Investigation of the Tearing Mechanism of Bonded Soft Elastomers with Finite Interfacial Friction

by

Tamran Hughen Lengyel

A thesis submitted in partial fulfillment of the requirements for the degree of

Doctor of Philosophy

Department of Mechanical Engineering
University of Alberta

Abstract

The role of interfacial slippage on the deformation and stress fields near an interfacial crack are investigated in detail. First, the limiting extents of interfacial bonded friction, defined as the 'frictionless' and 'no-slip' cases, were modeled as hyperelastic elastostatic boundary value problems in plane strain. Using ideas similar to a fracture mechanics cohesive zone model, the 'finite friction' case is established as a shear stress threshold on the bonded surface which if exceeded, allows interfacial slippage. The solutions of all three of these boundary value problems are found in the near field of the crack front using asymptotic analysis. Comparison of these solutions confirm experimental results that the inhibition of interfacial slip in the no-slip case caused material to contract inward producing a non-vertical surface angle that is shown to be a ratio of the in-plane stress components. The finite friction and frictionless cases were found to be related in that they both showed interfacial slippage after loading and the surface angle was perpendicular to the bonded interface. Further, the frictionless case is achieved when the finite friction threshold is set to zero, and in the presence of interfacial friction on the bonded edge there was a reduction in movement and the crack opening profile became more blunted or sharpened depending on the direction of slip.

Extensive numerical simulations were performed using commercial finite element analysis software. Simulations for all three friction cases were studied and the results showed strong agreement with the analytical near field findings. Using the numerical

data, the effects of far-field loading conditions on the remaining constants in the near-field solutions were quantified and discussed. Through the course of these simulations, it was identified that the direction of loading also plays a significant role on the deformation and stress fields near the crack front. The blunting effect occurred when the loading direction was more perpendicular and the interfacial slip moved to the right. However, when the loading direction was more tangential to the surface away from the crack the deformation field was sharpened and material in the slip-zone moved to the left. This direction of transition was also affected by the total deflection of the far-field loading. Moreover, the amount of blunting was found to be directly related to the magnitude of the stress threshold, and depending on the shear stress direction on the bonded edge (linked to the direction of slippage), produces significantly different normal stress magnitudes and failure modes.

From the results presented in this study, a method of quantifying interfacial friction through deflection geometry is introduced and design considerations for desired adhesive tearing mechanisms are provided.

Preface

Many of the results presented here were found through a collaborative nature and I can't justly take full credit for anything without acknowledging Dr. Rong Long and Dr. P. Schiavone (my supervisors and co-authors in other works) for their support and brilliant insights. Their engagement over the past years helped me refine the ideas presented here, and helped me ensure much of the analysis became something worth reading about.

The bulk of the findings presented in this dissertation was published in two journal papers. The first paper, titled "Effect of Interfacial Slippage on the Near-Tip Fields of an Interface Crack Between a Soft Elastomer and a Rigid Substrate" [1] was co-authored by myself, Dr. Rong Long and Dr. Peter Schiavone. This work covered the extents of friction only and are covered in portions of Chapters Chapters 2, 3, 4, 5, 6, 7, and 9.

The second paper is titled "Interface Crack Between a Compressible Elastomer and a Rigid Substrate with Finite Slippage" [2] (currently in review). Parts of this paper are found in Chapters 3, 5, 6, 8, and 9. This paper is a natural progression from the first paper as it covers interfacial slip inside the extents of friction.

This manuscript outlines more background detail and is intended to encompass full story covered by both papers mentioned above. Given that this work is mine alone (no co-authors), the work presented here may show a slightly different viewpoint.

This work on adhesion is dedicated to my best friend and companion, Beatrice Hollinshead. Thank you for sticking with me through it all.

Acknowledgments

To Kathleen Edwards: I thank you for all your support in the non-academic matters and the teaching advice over the years. Since you've been at the helm in the department, things are getting done. I learned a lot from the many examples of your organizational and personnel skills, and thank you most kindly for helping me find funds in various places to support me and other students.

To Dr. Billy Strean: Of all the training on pedagogy during my graduate work, I got the most teaching knowledge out of your workshop. Practicing what I learned there enabled me to win T.A. awards and attain great ratings as a sessional instructor. I'll never forget the three tenants of teaching: Follow the learning objectives, get (and keep) the students permission, and give them something they can't get from the Internet, YouTube or a textbook. It turns out, those rules work for most things so I'll keep them handy.

To (soon to be Dr.) Shawn Lavoie: Throughout my graduate work, you were one of the most intelligent colleagues I had the pleasure of working with. You always have answers that others can bank on. While working with you in other areas, you proved to be quite effective and a major contributor. Definitely an *A+* character and it's been a pleasure to work with you.

To (soon to be Dr.) Cuiying Jian: Thank you for being a friend and for all your contributions. You're smart as a whip and one of the hardest working people I've ever met. I also found your objectivity useful on multiple occasions.

To Dr. Ming-Zhao Jin: I loved our conversations about all kinds of topics. You are one of the kindest and most thoughtful people I've met and interacted in our program and it was a

pleasure to sit right behind you.

To Dr. Rong Long: While we didn't get as much time to collaborate as I'd have hoped, the short time spent working together had was an incredible learning experience for me. The polish that you put on things is fantastic and I'm incredibly proud to have been a co-author with you. With your guidance, I was able to understand extremely complicated things in simple ways. The question you often asked made it's way into my toolbox and the theme of it is worth repeating here: "How does this proposed action help solve our problem?" - or, as many of those close to me have heard so many times since: "What is the utility in that action?"

To Dr. Andrew Mioduchowski: After my Masters you advised that if I ever did a doctorate degree in anything theoretical that I'd have to do something non-linear. The work presented here is just that and I thank you for all the useful bits of advice over the last few years. I've always valued your opinion and hope this dissertation makes you proud.

To Dr. Peter Schiavone: As it turns out, you have rescued me on multiple occasions. Thank you for helping me salvage this degree when things didn't work out with other parties. I am thankful for your ability to navigate the bureaucracy because without that I'd be lost. I believe we are cut from the same cloth in many respects and hope this work meets with your approval. At this time, after all we've been through, I hold no other in our department in higher regard. Thank you for working with me and all your mentoring.

I would also like to thank the rest of the people in the Mechanical Engineering department as a whole; both from a funding perspective and allowing me opportunities to teach. Thank you for having enough faith in me to let me try. Also, as I understand it, some of my academic funding came at least indirectly from the Natural Sciences and Engineering Council of Canada.

Contents

List of Tables

List of Figures

List of Symbols

α	Loading angle
$\hat{\mathbf{E}}_A$	Unit basis vector in the referential configuration ($A = 1, 2, 3$)
$\hat{\mathbf{e}}_i$	Unit basis vector in the spatial configuration ($i = 1, 2, 3$)
$\mathbf{X}$	Referential coordinate vector
X_A	Referential coordinate magnitude ($A = 1, 2, 3$)
$\mathbf{x}$	Spatial coordinate vector
x_i	Spatial coordinate magnitude ($i = 1, 2, 3$)
$\mathbf{u}$	Deflection vector field
u_i	Deflection coordinate magnitude ($i = 1, 2, 3$)
$\mathcal{F}$	Deformation gradient ($d\mathbf{x} = \mathcal{F} d\mathbf{X}$)
$\otimes$	Tensor product: $(\mathbf{a} \otimes \mathbf{b})\mathbf{c} = (\mathbf{b} \cdot \mathbf{c})\mathbf{a}$
∇_{x}	Referential gradient operator ($\nabla_{\mathrm{x}}(*) \equiv \mathrm{Grad}(*)$)
V_0	Referential volume
V	Spatial volume
J	Jacobian ($\det \mathcal{F}$)
∇	Spatial gradient operator ($\nabla(*) \equiv \mathrm{grad}(*)$)
$\mathbf{I}$	Referential identity tensor ($= \delta_{AB} \hat{\mathbf{E}}_A \otimes \hat{\mathbf{E}}_B$)
δ_{ij}	Kronecker delta function
ε_{ijk}	Alternator delta
$\mathfrak{C}$	Referential displacement tensor

Continued on Next Page...

List of Symbols (Continued)

$\mathcal{E}$	Referential Strain tensor
$\mathcal{T}$	Referential traction vector (1st Piola) ($\equiv \mathcal{PN}$)
$\mathbf{t}$	Spatial traction vector (Cauchy) ($\equiv \boldsymbol{\sigma}\mathbf{n}$)
$\mathcal{N}$	Referential surface normal vector
$\mathbf{n}$	Spatial surface normal vector
$\mathcal{P}$	First Piola-Kirchhoff stress tensor
$\boldsymbol{\sigma}$	Cauchy stress tensor
A_0	Area in referential basis
A	Area in spatial basis
$\mathcal{S}$	Second Piola-Kirchhoff (referential) stress tensor
$\psi(I_1, I_2, I_3)$	Strain Energy Density Function
I_1, I_2, I_3	Invariants of the referential displacement tensor $\mathcal{C}$
$\tilde{\varepsilon}_{ij}$	Planar form of alternator delta ($\equiv \varepsilon_{ij3}$)
I	Plane-Strain trace invariant of the referential displacement tensor
$\mathcal{W}$	Strain energy density function in plane strain form
r	Planar radial component ($r \equiv \sqrt{X_1^2 + X_2^2}$)
θ	Planar polar component ($\tan\theta = X_2/X_1$)
$\tilde{\mathbb{C}}_A(\theta)$	Directional alternator function ($\tilde{\mathbb{C}}_1 \equiv \cos\theta$ and $\tilde{\mathbb{C}}_2 \equiv \cos\theta$)
τ	Shear stress threshold on bonded surface (finite friction case)
β	Material incompressibility parameter (related to ν)
ν	Poisson's ratio
μ	Small strain shear modulus
ξ	Non-dimensional shear stress threshold on bonded surface ($\xi \equiv \tau/\mu$)
$\mathcal{O}(*)$	Little 'O' notation

Continued on Next Page...

List of Symbols (Continued)

$\mathcal{O}(*)$	Big 'O' notation
$\bar{x}_1$	Crack tip interfacial displacement after loading (finite friction)
a, b	Deflection constants (finite friction)
$w(\theta)$	Angular variation for x_1 term (finite friction)
a_1, a_2	Deflection constants (no-slip)
ϕ	Wedge angle after loading (no-slip)
$\mathcal{J}$	The $\mathcal{J}$-Integral, also known as the energy release rate
$\bar{n}(\xi)$	Blunting parameter (finite friction)
$\chi(\theta)$	First order angular variation in J (finite friction)
L	Finite element dimensional length
Δ_X	Lateral far-field displacement loading
Δ_Y	Normal far-field displacement loading
Δ	Far-Field displacement loading ($\equiv \sqrt{\Delta_X^2 + \Delta_Y^2}$)
$\hat{a}_1, \hat{a}_2$	Opening shape point estimates for no-slip case
$\hat{b}$	Opening shape point estimate for finite friction case
$\tilde{\alpha}(\Delta)$	Transition loading angle (when $\sigma_{12} = 0$)
$\Delta_c(\Delta_Y)$	Critical lateral loading (Δ_X when $\sigma_{12} = 0$)
δ	Referential slip-zone length (finite friction)
δ_{guess}	Referential slip-zone length guess (finite friction)
$\tilde{\delta}$	Spatial Slip-Zone Length (Finite Friction)
$\bar{\phi}$	Adjusted wedge angle approximation after interfacial slippage

Part I

Background and Preliminaries

1 - Introduction

1.1 Project Motivation

The total industrial adhesive world market is projected to be worth over forty billion dollars (U.S.) by the year 2020 with water based adhesives being the most commonly used [4, 5]. Adhesive performance and the physical nature of adhesive detachment are primarily surface phenomena [6], however the effects of the adhesive material in combination with surface conditions of the adherand (what the adhesive is bonded to) are not well understood. While there has been a great deal of research on adhesives to date, much of our understanding of the surface process of detachment is empirical, requiring researchers to use expensive laboratory time or equipment and new discoveries are often serendipitous. Also, with insights mainly coming from numerical or experimental work, an understanding of the physics behind the true nature of adhesion performance is left undiscovered.

One of the significant findings in recent years was the experimental relation between surface interfacial slippage between a bonded elastomer and substrates [7, 8, 9, 10, 11]. Newby et al [7] performed peeling experiments of bonded soft elastomers (imagine un-peeling Scotch® tape) at shallow angles to find that the crack front moved in the opposite direction of pulling and a “finger tip” was formed due to material contraction [11]. A visualization of this is

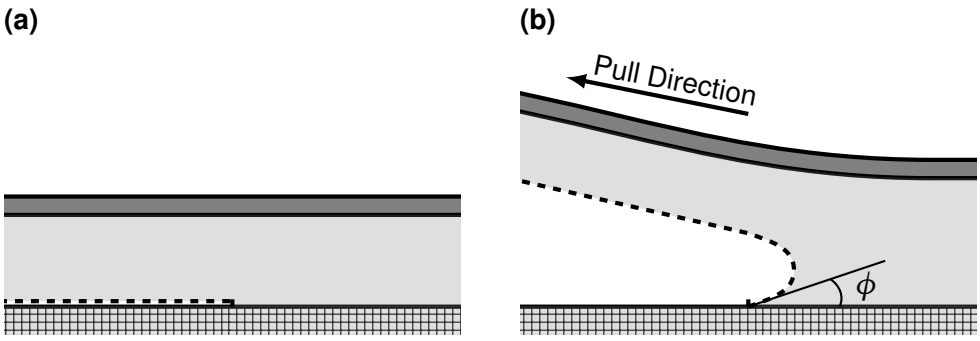

Figure 1.1: Visualization of Pre and Post Peel Test of a Soft Elastomer Bonded to a Substrate. (a) Unloaded Interface Crack (b) After Loading

shown in Figure 1.1 where the soft elastomer adhesive bulk material is depicted by the light gray shading, the darker gray shading represents the tape backing, the substrate is shown as a hatch pattern and the interfacial free edge (the unbonded portion) is depicted by a dashed line. In Figure 1.1a, the unloaded geometry is shown while Figure 1.1b is a visualization of post loading. When pulled to the left, Newby et al found that the free edge lifted and the indented finger tip moved material to the right. Even more interestingly, when the substrate had a pre-applied coating that allowed more interfacial slippage, the required peel strength for crack tearing was lower even though the calculated adhesion energy was higher [7].

Several works have been published on why and how interfacial slippage affects the wedge angle and the peeling force (and more generally, the loading force). The most common idea is that interfacial slippage causes energy dissipation at the interface (essentially, the work of some 'frictional' force over a displacement) leading to less energy available for debonding [8, 9, 12, 13, 14, 15, 16, 11]. This seems to be contradictory to Newby et al's findings, and few usable closed form solutions exist for bonded soft elastomers which would allow designers to utilize interfacial slippage to their advantage in a quantitative way. The purpose of the research presented in this dissertation is to provide further insights on the deformation and stress field near the crack front of a soft elastomer bonded to a rigid adherand with interfacial slippage. To this end, the primary goal is to quantify a tearing mechanism in the form of a

convenient, algebraic, deformation field near the front of a crack from which stresses can be derived, allowing others to make informed and quantitative decisions when designing bonded joints. With a closed form mechanism defined, it is hoped that design decisions for bonded interfaces can be made with less physical testing. Hence, reducing the overall cost of new discoveries and meet the increasing demands of the growing market for soft adhesives [4].

1.2 Background and Literature Review

When a crack resides between two materials with different properties that are bonded together, we refer to this as an interface crack [17, 18, 19]. For example, Figure 1.1a shows an example of a soft elastomer material (light gray) adhered to a rigid substrate (hatch pattern) in the unloaded configuration where the dashed line represents the interfacial crack edge. Upon loading, deflection of the bulk elastomer occurs (see Figure 1.1b) and the stresses near the crack front along the interface are found mathematically to have stress singularities as the distance from the crack tip $r \to 0$ [20, 21, 22]. To deal with these singularities and understand the nature of the debonding process of a soft adhesive from a more rigid adherand requires fracture mechanics methods [20, 21, 23, 24] where a localized separation zone near the crack tip is expected to form and these stress singularities are adjusted. Inside this small zone, often referred to as a 'cohesive zone' [20, 21], we can impose finite stress fields of various forms [25, 26] which can be interpreted as material hardening so that the crack will open smoothly [27, 28] and the cusps that were previously present are blunted [20, 27] by the local modification of the stress field near the crack tip. This method requires analysis on the entire perimeter of the bonded edge [29, 30], however very near the crack front is of most interest because this is where delamination is expected. In fact, many adhesion performance problems can be analyzed as interface cracks. Kinloch [31, 32] discussed various aspects of surface phenomena and reviewed different types of epoxy bonded joints that can be modeled as interfacial cracks. Baldan [6] also reviewed adhesion of bonded joints utilizing

analytical models and concluded that adhesion is purely a surface phenomenon and that the physical properties of an adhesive joint depend strongly on how the adhesive and adherand interact. Kendall [33] discussed a basic theory to evaluate the stresses (more specifically crack propagation) in lap shear joints. Some notable examples of bonded joints utilized in industry are shown in Figure 1.2.

First, recall the tape peeling experiments by Newby et al [7]. To model the tape peeling problem (Figure 1.2a) we define the peel angle or loading angle as α, which is typical measured from the negative $\hat{\mathbf{E}}_1$ axis. Here, the tape backing (cross hatch pattern) is typically much stiffer than the adhesive elastomer material (light gray) and the rigid adherand of the tape is denoted by the lined hatch pattern. The crack front then lies on a line parallel to the $\hat{\mathbf{E}}_3$ axis and denotes the edge of the bonded interface with the adherand. Similar to the tape peeling example, a butt joint is depicted in Figure 1.2b. Here, the loading angle (Pull Direction) and geometrical orientation is chosen such that the interfacial crack is the connected plane between either of the two (relatively) rigid blocks and the adhesive material. The interfacial crack problem for lap joints is depicted in Figure 1.2c. With carefully chosen geometry, the problem for most bonded joints can be modeled using the same approach by describing the bulk material of the bonded adhesive and surface conditions which are described by the geometry and properties of the adherand surface. It must be noted that while the peel angle depicted in Figure 1.2a is not identically the same concept as the pull direction depicted in Figures 1.2b and 1.2c, the variable α is used interchangeably in the proceeding chapters to more generally describe some far field loading angle.

Market research shows that more than half of industrial adhesives in use are made up of chemically bonded or water based adhesives [4, 5]. While these types of adhesive materials are often much less stiff than the adherends being bonded, they can also have stretch more than five times their original length before debonding or detachment occurs [34]. Given this, the bulk adhesive materials are often modeled as soft elastomers. Like industrial applications,

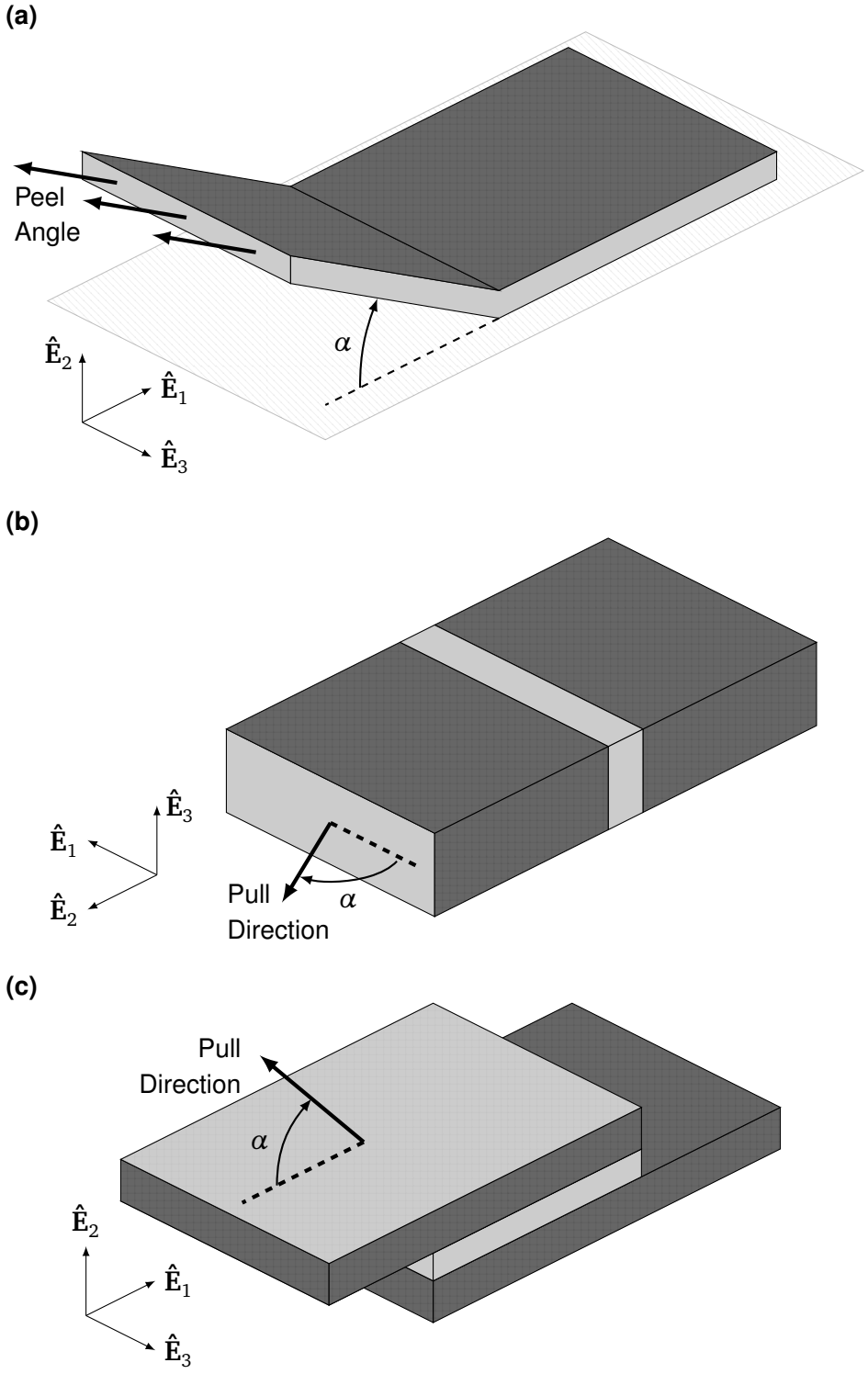

Figure 1.2: Visualizations of Loading Examples That Use Soft Elastomer Adhesives. (a) Tape Peeling from a Rigid Flat Surface (b) A Loaded Butt Joint (c) A Loaded Lap Joint.

similar processes and mechanisms exist in nature where wet and sticky secretions that allow slip with adhesion have been published. Gravish et al [35] determined that the external frictional loss is analogous to a viscous internal dissipation during detachment of PSAs. Endlein et al [36] studied tree frog adhesion where the detachment of hanging frogs hands and feet were analogous to a slippery bonded joint, most resembling the lap joint from Figure 1.2c. For example, tree frogs excrete a liquid adhesive [36] which enable them to stay attached to overhanging surfaces. Endlein showed that changing the loading angle α (due to the angle of the wall the tree frog was attached to) caused the tree frog to detach. This and other works show that the pulling angle α affects the detachment force required for bonded soft elastomers [33, 37] and that lubrication between the bonded surface will affect interfacial friction and is related to the detachment force [38, 7].

To achieve a closed form solution with materials that can undergo large strains, hyperelastic materials by definition have an equation for material strain energy density and may undergo large strain [39, 34, 40, 41]. Using algebraic methods, the hyperelastic strain energy density function is then used to derive the governing bulk material differential equation through a force or momentum balance [34, 39, 40]. While there is a great deal of literature on hyperelastic material models of soft elastomers [42, 43, 44, 42, 45, 46, 47], choosing an appropriate strain energy function for the present study requires an understanding of the various physical properties that can affect interfacial crack growth and performance. For example, some soft materials can undergo strain hardening, which can be simply defined for the purposes of this work as an increase in material stiffness after loading [48, 49, 50, 51, 52]. Also, while many elastomers can be well modeled as incompressible [34], the degree of compressibility can also affect the deformed geometry [34, 47] and should be considered. For quantitative values of these material properties, various collections can be utilized [53, 54].

In a study on rheological properties of hot-melt and PSAs, Gibert et al [55] determined that interfacial fracture is dependent on cure time and that fracture occurs in a ‘stick-slip’ way

related to the material viscoelasticity as well as the glassy transition, another interpretation of hardening in the bulk adhesive. Early work on the physics behind the dynamics of the stick-slip [56] phenomena was laid out by Schallamach [57] where it was concluded that frictional sliding of rubbery materials happens in waves of detachment along the bonded front due to the viscoelastic process of rubber friction [58]. While Shallamach's work was on compressive (not bonded) friction, this idea may explain some of the physical results from Newby et al [7] and is evidence that interfacial slippage may act in a 'stick-slip' manner.

Nase et al determined through experiments that higher viscoelasticity tended to produce a finite wedge angle $\phi \neq \pi/2$ after loading [59]. However, with higher polymer cross-linking, which should result in a stiffer adhesive material with less interfacial deflection, they found that these test samples showed a more vertical wedge angle ($\phi \simeq \pi/2$) [59]. They concluded that the energy required to separate the bonded elastomer from substrates is a function of pulling speed [60] and that more energy is required to propagate an interfacial crack of the adhesive if the samples are thicker, or if the material stiffness is lower - indicating that ductility may also play a role. Nase et al also found that more air pockets formed in the adhesive material [59] with weaker cross-linking. Ghatak et al [61] concluded that as the amount of cross-linking increases, the shear stress versus pulling velocity curve had a reduced scale; while Allegra and Raos [62] predicted a dramatic reduction of the sliding friction of higher versus lower cross-linked polymers. Using energy models [63], they determined that the frictional force is a function of sliding velocity and the effective friction coefficient is always a decreasing function of the material strain rate. Momozono et al [64] reviewed various models of adhesive friction and found that the frictional strength depends not only on surface parameters, but also concluded dependence on the material bulk viscoelasticity, elastic modulus, and the ratio of critical velocity and viscoelastic relaxation rate. Since viscoelasticity is a dissipative process which is a speed dependent parameter [37, 60], this evidence implies that the deformation and stress field near the crack front depends highly on the loading speed [33]. Other evidence

shows that high crack propagation velocities cause more dissipation [13] and nominal stresses increase as deformation rate increases [65].

In another work, Livne et.al [14] used modeling with linear and nonlinear elastic zones where energy dissipates differently. They found that dissipation was confined to a region smaller than $\sim 20\mu m$ and the blunting amount was found to correlate with the energy flux and this blunting distance increased more than linear as tearing speed increased. Through experiments, Liechti and Wu [66] found that slower pulling speeds caused more blunting and vertical wedge angle, where as faster pulling produced a finite wedge angle which resembled the 'fingertip' indent published by Newby et al [7]. These findings indicate that time dependence enters via the cohesive zone itself and that the failure mode process zone (the small amount of material near the crack front) is one of shear rather than tension which suppresses crack growth, so that the shear friction is dissipative (more on this below) [66]. Ondarcuhu [67] concluded that at higher separation rates, the failure is more interfacial and also notes the possibility of viscoelasticity effects happening on the bonded layer.

Sun et al [68] described interfacial fracture of PSAs and found that viscoelastic properties are related to pressure sensitive adhesion which is reflected in surface shear (as well as other properties). Wu and Huang [16] described crack expansion through shear as a distribution of moving dislocations on the bonded surface and inertial effects of the bulk material was found to be the most significant factor with nominal loading. When moving fast enough, the required tearing stress was larger than the yield stress [16], however, for lateral loading the applied stress required for tearing was lower than the actual yield stress.

Various works show that an increase in surface roughness will actually reduce adhesion strength on the bonded surface of an interfacial crack [69, 70, 71, 64]. Recall the conclusion of Newby et al [7, 8, 9] that various surface coatings on substrates were used before bonding to show that different degrees of interfacial slippage changes the deflection geometry due to energy dissipation through material movement along a surface friction (shear traction). Begly

et. al [72] noted that fracture toughness is made up of adhesion energy, but also work due to friction; and without slip, then shear will contribute to detachment, but with slippage it should not. Lu et al [11] also found through peel tests that the length scales of a slip zone (the amount of material near the crack front which moves due to loading) and contact angle ϕ are the most significant contributors to total fracture energy. These findings imply that the peel force is reduced with the occurrence of interfacial slippage. Collino et al [12] determined that peel force is a function of the wedge angle ϕ (see Figure 1.1b) which affected frictional slippage near the crack tip and implies that sliding influences deformation over scales larger than the asymptotic field [73] scale. Hui et al [15] explained that energy is dissipated from blunting in an interfacial crack, increasing the required energy for detachment. An implication here could be that the dissipation of blunting in an interfacial crack is similar to dissipation of a frictional surface force over some distance. So, due to dissipation the more interfacial slip allowed by the surface should predict a stronger pulling or peeling strength.

With the continuum approach, the surface part of any modeling can be defined by boundary conditions (BCs) which are derived from either a constraint or force balance on the interface [39, 40, 34]. Interfacial fracture can be affected by various surface properties which can change the types of BCs. Even though most cohesive models deal with separation in the normal direction [21, 20], we are most interested in how interfacial slippage changes adhesion strength deflection geometry and insight into a lateral cohesive zone could be taken from these many works for modeling BCs. In their recent review of cohesive zone models, Park and Paulino [74] compared and contrasted several methods of approximating the fracture process and note that mixed-mode (loading in both normal and lateral directions) cohesive fracture should be modeled with great care.

Once all of the material and surface properties are taken into account, a material model can then be chosen and a boundary value problem (BVP) can be formulated and solved. For small deflections with a linear elastic fracture mechanics (LEFM) [20] approach, interfacial crack

problems show oscillatory singularities in the form of complex exponents of r as $r \to 0$ [75, 76] which imply inter-penetration of the bulk material and the adherand that were determined to be 'unphysical' [17] due to the incorrect modeling of the problem as linearized strain. We can account for large strains in our continuum mechanics models by keeping our geometric non-linear strain terms in the bulk governing equations and BCs [34, 21]. A great deal of work has been done in non-linear elastostatics with some interesting results. To determine solution fields that are viable in a small range of interest, then asymptotic analysis [73, 27, 28] techniques can be used. This method lends itself nicely to many crack tip problems of interest and there are many examples [48, 77, 78, 79, 80, 50, 51, 52, 27, 28, 81, 82] of how to use asymptotic analysis to determine 'near field' solutions which are finite, local fields and are typically not viable far away from the point of interest unless many terms are found [73]. Unfortunately, finding unique, analytical solutions for non-linear problems using anything other than very simple material models and geometry can be difficult. Therefore, interface conditions and bulk materials must be chosen carefully in order to achieve usable results.

Knowles introduced the Generalized Neo-Hookean (GNH) model [83], which is for a soft, incompressible, rubbery elastomer with strain stiffening which has been used in several works to model soft elastomers [50, 51, 52, 49, 84]. Krishnan et al [84] used the GNH model to study interface cracks between the adhesive and a rigid flat substrate. Krishnan noted that while the oscillations from LEFM interface cracks mentioned above produced oscillatory inter-penetration, these singularities disappear using the non-linear terms with the incompressible GNH model. However, after an extensive search, no asymptotic solution could be found for a plane strain interface crack problem using an incompressible elastomer material adhered to a rigid substrate. This is possibly due to the fact that Krishnan's simulations showed an almost flat wedge angle ($\phi \simeq 0$), leading to oscillations in the normal stress field on the bonded interface near the crack front. It was speculated that these oscillations were numerical error given that the solutions yielded almost infinite contraction. Long et al [81]

noted that one reason asymptotic solutions do not exist for many of the problems studied is because several incompressible material models (while they are well tested) may produce asymptotic deformation fields that are not separable functions of r (the distance from the crack front) [50], where r is the asymptotic variable; in other words, a mathematical modeling issue. This is more evidence that the loaded wedge angle ϕ of an interface crack is strongly related to the stress fields [27, 28] and without blunting, a cusp (quantified by a very small wedge angle, $\phi \simeq 0$) is formed between the adhesive and surface leading to instability of the stress fields there.

Other insights of hyperelastic models and asymptotic solution techniques can come from work on general crack problems. Given the symmetry of solutions [80, 85, 27] above and below the full plane lateral axis, then the general problem is assumed to be analogous to an interface crack with the material bonded to a rigid substrate and no interfacial slip resistance. Given this, if results are found using a finite friction slip model, the works of Knowles and Sternberg [85, 48, 77], Geubelle et al [50, 51, 52] and Stephenson [80] for general cracks should be compared with zero friction. We can also employ finite element analysis [86, 87, 88, 89] to verify any analytical formulations or solutions found from any BVP to ensure the computed solution fields match or show similar trends for any solutions found.

1.3 Structure of Manuscript

Using what we now know, the goal is set to explore tearing mechanisms that take into account bonded interfacial slippage. The ideas presented in the chapters henceforth are in the pursuit of this goal and this dissertation is broken up into parts I through V.

Part I begins with the current chapter which outlines the motivation and background of the problem at hand. Then, in Chapter 2, the mathematical foundations are formulated in a general manner. Section 2.1 is a basic review of the continuum mechanics formulations for hyperelastic materials and the general plane strain interface crack problem for hyperelastic

materials is outlined in Section 2.2.

Using the preliminaries from Chapter 2, a plane strain interface crack problem for generalized hyperelastic materials is formulated in Section 3.1 and all but the bonded BC are discussed. Three BCs to model the bonded surface are derived in Section 3.2, being the 'frictionless' case (where interfacial slippage is unencumbered along the bonded edge), the 'no-slip' case (perfect bonding where no interfacial slippage may occur) and a simple finite friction case where interfacial slip is allowed but is encumbered by a finite, constant interfacial shear stress. The results from Sections 3.1 and 3.2 are summarized in Section 3.3. To use these formulations, in Section 3.4 a list of viable material strain energy formulations are discussed and a specific form of a compressible Blatz-Ko strain energy function is chosen. With the material model and the other formulations, the BVPs of interest are fully worked out and summarized in Section 3.5.

Part II begins with Chapter 4 where asymptotic analysis [73] is utilized to determine the near field displacement and stress fields for the three states of interfacial bonding friction. The solutions of the frictionless and no-slip cases are worked out in Sections 4.1 and 4.2 respectively and Section 4.3 outlines the solution of the finite friction case.

Evaluations of the near field solutions for all three cases is the subject of Chapter 5. First, the solutions for the no-slip and the frictionless cases (the extents of interfacial friction) are compared in Section 5.1, where closed form expressions are introduced for tearing mechanisms of both extents of friction. A comparison of the analytical solutions for the no-slip and finite friction cases is reviewed in Section 5.2 where it was confirmed that the frictionless problem is a special case of the finite friction problem.

Part III highlights the numerical methods and procedures used in order to validate the insights from the near field solutions, and Chapter 6 outlines the finite element model to be used for simulations of the problems summarized in Section 3.5. Section 6.1 outlines the software, material model, mesh geometry and loading conditions. How to utilize the finite

element solutions with the near field solutions from Chapter 4 and validation methods are subjects of Sections 6.2 and 6.3 respectively.

In Chapter 7, finite element analysis is performed using the no-slip and frictionless cases with various loading conditions. In Section 7.1, the finite element model is validated using normal loading and the effect of loading on the deformed geometry and stresses are discussed. Finally, a special stress state is discovered and quantified in Section 7.2 which is utilized to determine a starting point with the finite friction simulations in Chapter 8. Section 8.1 outlines the iteration method used to determine the slip zone lengths and outlines two examples to validate this technique proceeding to Section 8.2 for an extensive study of normal loading on interfacial slippage with finite interfacial friction. The effects of lateral loading with finite friction is discussed in Section 8.3 where the implications of the transitional loading angle are reviewed and two separate forms of interfacial friction are quantified.

A final discussion portion is the subject of Part IV, beginning with Chapter 9 which outlines a summary of the insights and potential issues of the interfacial slippage model proposed. Previous experimental results are compared to the findings in the earlier sections in Section 9.1 leading to more insights on how the deformation state may transition from the no-slip to the finite friction cases, discussed in Section 9.2, and some basic design considerations are provided in Section 9.3. Finally, a summary of thoughts and ideas are wrapped up in Chapter 10, where in Section 10.1 the notable findings are summarized, concluding with a brief discussion of avenues of future studies in Section 10.2.

For a list of all the references used in the creation of the results presented, see the bibliography in Part V.

2 - Problem Preliminaries

2.1 Hyperelastic Elastostatics

The Hyperelastic class of materials is defined through a strain energy density function and may undergo significant elongation [34]. Here, the mathematical framework for hyperelastic elastostatics is reviewed and standard continuum mechanics rules [39, 40, 34] are assumed. Einstein summation notation is assumed everywhere, meaning that summation of indices is required even if the summation symbols $\sum$ are not shown. All vector bases in this work are assumed linear and Cartesian [40]. Before loading, the material coordinates $\mathbf{X}$ are described in the referential basis $\hat{\mathbf{E}}_1, \hat{\mathbf{E}}_2$ and $\hat{\mathbf{E}}_3$. Once loaded, deformation occurs where the deformed coordinate $\mathbf{x}$ is described in the spatial basis $\hat{\mathbf{e}}_1, \hat{\mathbf{e}}_2$ and $\hat{\mathbf{e}}_3$. Displacement is defined as the difference between these two coordinates [39, 40] so that

$$\mathbf{u}(\mathbf{X}) \equiv \mathbf{x}(\mathbf{X}) - \mathbf{X}, \qquad \text{or} \qquad \mathbf{x}(\mathbf{X}) = \mathbf{u}(\mathbf{X}) + \mathbf{X}. \tag{2.1}$$

The mapping of deformation between the referential and spatial configurations can be expressed through the deformation gradient $\mathcal{F}$, which is a mixed basis tensor defined as [39, 40]:

$$\mathcal{F}(\mathbf{X},t) \equiv \nabla_{\mathrm{x}}\mathbf{x} = \mathrm{Grad}\,(\mathbf{x}) = \frac{\partial \mathbf{x}}{\partial \mathbf{X}} = \frac{\partial x_i}{\partial X_A}\hat{\mathbf{e}}_i \otimes \hat{\mathbf{E}}_A, \tag{2.2}$$

where the ratio between the volume in the spatial and referential configurations is the determinant of the deformation gradient, defined as J, and

$$J(\mathbf{X},t) \equiv \frac{dV}{dV_0} = \det \mathcal{F}. \tag{2.3}$$

Note that in the special case of incompressible materials, $V = V_0$ and it is required that $J = 1$. To avoid the possibility of infinite contraction, note that J must be positive and non-zero ($J > 0$) and so the deformation gradient $\mathcal{F}$ must be invertible so that

$$\mathcal{F}^{-1} = \nabla\mathbf{X} = \mathrm{grad}\,(\mathbf{X}) = \frac{\partial \mathbf{X}}{\partial \mathbf{x}} = \frac{\partial X_A}{\partial x_i}\hat{\mathbf{E}}_A \otimes \hat{\mathbf{e}}_i. \tag{2.4}$$

Also note that the inverse of $\mathcal{F}$ requires [39, 40, 34]

$$\mathcal{F}^{-1}\mathcal{F} = \mathbf{I}, \tag{2.5}$$

where $\mathbf{I}$ is the referential identity tensor and is defined as

$$\mathbf{I} \equiv \delta_{AB}\hat{\mathbf{E}}_A \otimes \hat{\mathbf{E}}_B, \tag{2.6}$$

and the Kronecker delta function [39, 40] is defined as

$$\delta_{ij} \equiv \begin{cases} 1, & i = j, \\ 0, & i \neq j. \end{cases} \tag{2.7}$$

From this and Eqn. (2.5), the inverse and transpose-inverse of the deformation gradient (which will be useful later) can be worked out to be [40, 39]

$$\mathcal{F}^{-1} = \left[\tfrac{1}{2}\varepsilon_{ijk}\varepsilon_{ABC}J^{-1}\mathcal{F}_{jB}\mathcal{F}_{kC}\right]\hat{\mathbf{E}}_A \otimes \hat{\mathbf{e}}_i, \tag{2.8a}$$

$$\text{so that} \quad \mathcal{F}^{-T} = \left[\tfrac{1}{2}\varepsilon_{ijk}\varepsilon_{ABC}J^{-1}\mathcal{F}_{jB}\mathcal{F}_{kC}\right]\hat{\mathbf{e}}_i \otimes \hat{\mathbf{E}}_A. \tag{2.8b}$$

The Levi-Civita alternator function is defined as the 'box product' [39] of any vector basis combination

$$\varepsilon_{ijk} \equiv \hat{\mathbf{e}}_i \cdot \left(\hat{\mathbf{e}}_j \times \hat{\mathbf{e}}_k\right) \qquad \text{and} \qquad \varepsilon_{ABC} \equiv \hat{\mathbf{E}}_A \cdot \left(\hat{\mathbf{E}}_B \times \hat{\mathbf{E}}_C\right), \tag{2.9}$$

so that

$$\varepsilon_{abc} \equiv \begin{cases} +1, & \text{if } a,b,c \text{ are even permutations of } 1,2,3, \\ -1, & \text{if } a,b,c \text{ are odd permutations of } 1,2,3, \\ 0, & \text{otherwise.} \end{cases} \tag{2.10}$$

Deformation is defined using the referential deformation tensor $\mathcal{C}$ [40, 39]

$$\mathcal{C} \equiv \mathcal{F}^T\mathcal{F} = \mathcal{F}_{iA}\mathcal{F}_{iB}\hat{\mathbf{E}}_A \otimes \hat{\mathbf{E}}_B = \frac{\partial x_i}{\partial X_A}\frac{\partial x_i}{\partial X_B}\hat{\mathbf{E}}_A \otimes \hat{\mathbf{E}}_B. \tag{2.11}$$

Note that $\mathcal{C}$ is a symmetric tensor, so $\mathcal{C} = \mathcal{C}^T$. From Eqns. (2.1) and (2.11), the referential deformation tensor also has the form:

$$\begin{aligned} \mathcal{C} &= \left(\nabla_{\mathrm{x}}\mathbf{u} + \mathbf{I}\right)^T\left(\nabla_{\mathrm{x}}\mathbf{u} + \mathbf{I}\right) = \left(\nabla_{\mathrm{x}}\mathbf{u}^T + \mathbf{I}\right)\left(\nabla_{\mathrm{x}}\mathbf{u} + \mathbf{I}\right) \\ &= \mathbf{I} + \nabla_{\mathrm{x}}\mathbf{u} + \left(\nabla_{\mathrm{x}}\mathbf{u}\right)^T + \left(\nabla_{\mathrm{x}}\mathbf{u}\right)^T\left(\nabla_{\mathrm{x}}\mathbf{u}\right) = \mathbf{I} + 2\mathcal{E} + \left(\nabla_{\mathrm{x}}\mathbf{u}\right)^T\left(\nabla_{\mathrm{x}}\mathbf{u}\right), \end{aligned}$$

where $\mathcal{E}$ is defined as the linear referential strain tensor:

$$\mathcal{E} \equiv \tfrac{1}{2}\left(\nabla_{\mathrm{x}}\mathbf{u} + \nabla_{\mathrm{x}}\mathbf{u}^T\right). \tag{2.12}$$

For small deformations, the non-linear term in $\mathfrak{C}$, being $(\nabla_x \mathbf{u})^T (\nabla_x \mathbf{u})$, can be discarded [40]. However, since hyperelastic materials can have larger deformations, the geometric nonlinearity must be kept in our modeling thus deviating from linear mechanics. To deal with this non-linearity, a mixed basis approach can be used. To define the resultant differential force element $d\mathbf{F}$ on a body in both the referential and spatial configurations, the force balance must satisfy

$$d\mathcal{F} = \mathbf{t}dA = \mathcal{T}dA_0, \tag{2.13}$$

where A and A_0 are areas in the spatial and referential configurations respectively, $\mathbf{t}$ and $\mathbf{T}$ are the Cauchy and first Piola-Kirchoff stress traction vectors, so that

$$\mathbf{t} \equiv \boldsymbol{\sigma}\mathbf{n} = \sigma_{ij} n_j \hat{\mathbf{e}}_i, \tag{2.14}$$

$$\text{and} \quad \mathcal{T} \equiv \mathcal{P}\mathcal{N} = \mathcal{P}_{iA} N_A \hat{\mathbf{e}}_i. \tag{2.15}$$

$\mathbf{n}$ and $\mathcal{N}$ are defined as the outward unit normal vectors of the spatial and referential surfaces respectively. The Cauchy and first Poila-Kirchhoff tensors are defined as $\boldsymbol{\sigma}$ and $\mathcal{P}$ respectively, and using Eqn. (2.13) these stress components are related by:

$$\boldsymbol{\sigma}\mathbf{n}dA = \mathcal{P}\mathcal{N}dA_0. \tag{2.16}$$

The change in area between the referential and spatial configurations can be found through Nanson's Formula [39, 40, 34]:

$$\mathbf{n}dA = J\mathcal{F}^{-T}\mathcal{N}dA_0. \tag{2.17}$$

Using this, the relation between the first Piola-Kirchoff stress tensor and the Cauchy stress tensor is found to be

$$\mathcal{P} = J\boldsymbol{\sigma}\mathcal{F}^{-T} = \mathcal{P}_{iA}\hat{\mathbf{e}}_i \otimes \hat{\mathbf{E}}_A. \tag{2.18}$$

The second Piola-Kirchhoff stress tensor $\mathcal{S}$ is symmetric and represents the stress tensor field in the referential basis where:

$$\mathcal{S} = \mathcal{F}^{-1}\mathcal{P} = J\mathcal{F}^{-1}\boldsymbol{\sigma}\mathcal{F}^{-T} = \mathcal{S}_{AB}\hat{\mathbf{E}}_A \otimes \hat{\mathbf{E}}_B. \tag{2.19}$$

All isotropic hyperelastic materials can be defined using a strain energy density function

$$\psi = \psi(I_1, I_2, I_3),$$

where I_i $(i = 1, 2, 3)$ are the invariants of the referential deformation tensor $\mathcal{C}$ [39, 40] and

$$I_1 \equiv \mathrm{tr}\{\mathcal{C}\} = \mathbf{I} : \mathcal{C}, \tag{2.20a}$$

$$I_2 \equiv \tfrac{1}{2}\left([\mathrm{tr}\{\mathcal{C}\}]^2 - \mathrm{tr}\left\{\mathcal{C}^2\right\}\right) = \tfrac{1}{2}\left([\mathbf{I} : \mathcal{C}]^2 - \mathbf{I} : \mathcal{C}^2\right), \tag{2.20b}$$

$$\text{and} \quad I_3 \equiv \det\mathcal{C} = [\det\mathcal{F}]^2. \tag{2.20c}$$

The second Piola-Kirchhoff stress tensor is related to the strain energy density function by [39]:

$$\mathcal{S} = 2\frac{\partial\psi}{\partial\mathcal{C}}, \tag{2.21}$$

which can be evaluated by using the standard definition of the chain rule [90],

$$\frac{\partial\psi}{\partial\mathcal{C}} = \frac{\partial\psi}{\partial I_1}\frac{\partial I_1}{\partial\mathcal{C}} + \frac{\partial\psi}{\partial I_2}\frac{\partial I_2}{\partial\mathcal{C}} + \frac{\partial\psi}{\partial I_3}\frac{\partial I_3}{\partial\mathcal{C}},$$

and each portion can be evaluated separately. The trace derivative becomes:

$$\frac{\partial I_1}{\partial \mathfrak{C}} = \frac{\partial}{\partial \mathfrak{C}}(\mathbf{I}\colon \mathfrak{C}) = \frac{\partial I_1}{\partial\, \mathfrak{C}_{AB}}\hat{\mathbf{E}}_A \otimes \hat{\mathbf{E}}_B = \frac{\partial\, \mathfrak{C}_{DD}}{\partial\, \mathfrak{C}_{AB}}\hat{\mathbf{E}}_A \otimes \hat{\mathbf{E}}_B = \delta_{AD}\delta_{BD}\hat{\mathbf{E}}_A \otimes \hat{\mathbf{E}}_B.$$

Therefore:

$$\frac{\partial I_1}{\partial \mathfrak{C}} = \mathbf{I}. \tag{2.22a}$$

Using similar logic:

$$\begin{aligned}\frac{\partial I_2}{\partial \mathfrak{C}} &= \frac{\partial}{\partial \mathfrak{C}}\left[\tfrac{1}{2}\left([\mathbf{I}\colon \mathfrak{C}]^2 - \mathbf{I}\colon \mathfrak{C}^2\right)\right] = \frac{\partial}{\partial\, \mathfrak{C}_{AB}}\left[\tfrac{1}{2}(\mathfrak{C}_{DD})^2 - \tfrac{1}{2}(\mathfrak{C}_{EF})^2\right]\hat{\mathbf{E}}_A \otimes \hat{\mathbf{E}}_B \\ &= [\delta_{AD}\delta_{BD}\,\mathfrak{C}_{DD} - \delta_{AE}\delta_{BF}\,\mathfrak{C}_{EF}]\,\hat{\mathbf{E}}_A \otimes \hat{\mathbf{E}}_B = \operatorname{tr}\{\mathfrak{C}\}\,\mathbf{I} - \mathfrak{C}.\end{aligned}$$

Therefore:

$$\frac{\partial I_2}{\partial \mathfrak{C}} = I_1\mathbf{I} - \mathfrak{C}. \tag{2.22b}$$

The derivative of the third invariant is shown by Chadwick [39] to be:

$$\frac{\partial I_3}{\partial \mathfrak{C}} = [\det \mathfrak{C}]\,\mathfrak{C}^{-1} = I_3\mathfrak{C}^{-1}. \tag{2.22c}$$

Putting this all together yields:

$$\mathfrak{S} = 2\left(\frac{\partial \psi}{\partial I_1} + I_1\frac{\partial \psi}{\partial I_2}\right)\mathbf{I} - 2\frac{\partial \psi}{\partial I_2}\mathfrak{C} + 2I_3\frac{\partial \psi}{\partial I_3}\mathfrak{C}^{-1}. \tag{2.23}$$

Also, using (2.2) and (2.19), the first Piola-Kirchhoff can be expressed as a function of the deformation gradient $\mathfrak{F}$, the invariants of $\mathfrak{C}$, and the strain energy density function:

$$\mathfrak{P} = 2\left(\frac{\partial \psi}{\partial I_1} + I_1\frac{\partial \psi}{\partial I_2}\right)\mathfrak{F} - 2\frac{\partial \psi}{\partial I_2}\mathfrak{F}\mathfrak{F}^T\mathfrak{F} + 2I_3\frac{\partial \psi}{\partial I_3}\mathfrak{F}^{-T} \tag{2.24}$$

The expression in Eqn. (2.24) can now be used to furnish the bulk material governing equations through a static force balance in the referential basis with no external body forces [39, 40, 34, 41]

$$\text{Div}\,(\mathcal{P}) = \nabla_{\chi} \cdot \mathcal{P} = 0, \qquad \text{or} \qquad \frac{\partial\, \mathcal{P}_{iA}}{\partial X_A} = 0. \tag{2.25}$$

The boundary conditions are also required, which are either a constraint or force balance (see Eqn. (2.15)) on each surface. The specifics of boundary conditions are discussed in more detail in Sections 3.1 and 3.2.

2.2 General Plane-Strain Hyperelasticity

Figures 1.2a through 1.2c show visualizations of bonded soft elastomers in loading where for each figure the soft elastomer adhesive is shown inlight gray. In the loaded case, the bonding material is assumed to be hyperelastic and given that the bonded surfaces (see the hatch and line patterned components) are typically much stiffer than the bonded material [34], they shall for all intents and purposes be considered rigid bodies for any problem modeling in this manuscript. While Hooke's Law suggests that the elastomer in tension is expected to contract [41, 34], if the width in $\hat{\mathbf{e}}_3$ direction is larger than the microscopic scale and the bulk of the material of interest resides well inside this thickness, then the strain in the $\hat{\mathbf{e}}_3$ direction is assumed negligible, and the displacement $u_3 \simeq 0$. This condition is known as plane strain [48, 34], and it is assumed that $x_3 = X_3$. Using Eqn. (2.2), the deformation gradient $\mathcal{F}$ has the properties:

$$[\mathcal{F}] = \begin{bmatrix} \mathcal{F}_{11} & \mathcal{F}_{12} & 0 \\ \mathcal{F}_{21} & \mathcal{F}_{22} & 0 \\ 0 & 0 & 1 \end{bmatrix}, \quad \therefore \quad \left[\mathcal{F}^{-1}\right] = \frac{1}{J} \begin{bmatrix} \mathcal{F}_{22} & -\mathcal{F}_{12} & 0 \\ -\mathcal{F}_{21} & \mathcal{F}_{11} & 0 \\ 0 & 0 & 1 \end{bmatrix},$$

so that the planar components of $\mathfrak{F}^{-1}$ and $\mathfrak{F}^{-T}$ $(i,A=1,2)$ become

$$\left[\mathfrak{F}^{-1}\right]_{Ai} = \tilde{\varepsilon}_{ij}\tilde{\varepsilon}_{AB}J^{-1}\left(\mathcal{F}_{jB}\delta_{iA}+\mathcal{F}_{iA}\delta_{iB}\right), \tag{2.26a}$$

and $$\left[\mathfrak{F}^{-T}\right]_{iA} = \tilde{\varepsilon}_{ij}\tilde{\varepsilon}_{AB}J^{-1}\mathcal{F}_{jB}, \tag{2.26b}$$

where $\tilde{\varepsilon}_{ij}$ represents the planar form of the Levi-Civita alternator ε_{ijk} from Eqn. (2.10) with $k=3$ so that

$$\tilde{\varepsilon}_{ij} \equiv \varepsilon_{ij3} = \begin{cases} 1, & \text{if } i=1, \text{ and } j=2, \\ -1, & \text{if } i=2, \text{ and } j=1, \\ 0, & \text{if } i=j. \end{cases} \tag{2.27}$$

From this and Eqn. (2.11), the referential deformation tensor $\mathfrak{C}$ has special plane strain form:

$$\mathfrak{C} = \begin{bmatrix} \mathcal{C}_{11} & \mathcal{C}_{12} & 0 \\ \mathcal{C}_{21} & \mathcal{C}_{22} & 0 \\ 0 & 0 & 1 \end{bmatrix}.$$

It is now convenient to introduce I as the trace of the sub-tensor of $\mathfrak{C}$, then

$$I \equiv \text{tr}\begin{bmatrix} \mathcal{C}_{11} & \mathcal{C}_{12} \\ \mathcal{C}_{21} & \mathcal{C}_{22} \end{bmatrix} = \mathcal{C}_{11}+\mathcal{C}_{22}=\mathcal{F}_{11}^2+\mathcal{F}_{12}^2+\mathcal{F}_{21}^2+\mathcal{F}_{22}^2, \tag{2.28}$$

and the three principal invariants of the tensor $\mathfrak{C}$ reduce to two plane strain invariants [48]:

$$I_1 = I+1, \quad I_2 = J^2+I, \quad \text{and} \quad I_3 = J^2, \tag{2.29}$$

so that the strain energy density function in plane strain can be represented as a function of the two plane strain invariants

$$\psi(I_1, I_2, I_3) = \mathcal{W}(I, J). \tag{2.30}$$

These plane strain invariants also have the form:

$$I(X_1, X_2) = \left[\frac{\partial x_1}{\partial X_1}\right]^2 + \left[\frac{\partial x_1}{\partial X_2}\right]^2 + \left[\frac{\partial x_2}{\partial X_1}\right]^2 + \left[\frac{\partial x_2}{\partial X_2}\right]^2 \tag{2.31a}$$

$$\text{and} \quad J(X_1, X_2) = \frac{\partial x_1}{\partial X_1}\frac{\partial x_2}{\partial X_2} - \frac{\partial x_1}{\partial X_2}\frac{\partial x_2}{\partial X_1}. \tag{2.31b}$$

Recalling that $J > 0$ and re-arranging, we find

$$\begin{aligned}
I &= \left[\frac{\partial x_1}{\partial X_1}\right]^2 + \left[\frac{\partial x_1}{\partial X_2}\right]^2 + \left[\frac{\partial x_2}{\partial X_1}\right]^2 + \left[\frac{\partial x_2}{\partial X_2}\right]^2 \\
&= \left[\frac{\partial x_1}{\partial X_1}\right]^2 - 2\frac{\partial x_1}{\partial X_1}\frac{\partial x_2}{\partial X_2} + \left[\frac{\partial x_2}{\partial X_2}\right]^2 + \left[\frac{\partial x_1}{\partial X_2}\right]^2 + 2\frac{\partial x_1}{\partial X_1}\frac{\partial x_2}{\partial X_2} + \left[\frac{\partial x_2}{\partial X_1}\right]^2 \\
&= \left[\frac{\partial x_1}{\partial X_1} - \frac{\partial x_2}{\partial X_2}\right]^2 + \left[\frac{\partial x_1}{\partial X_2}\right]^2 + 2\frac{\partial x_1}{\partial X_2}\frac{\partial x_2}{\partial X_1} + \left[\frac{\partial x_2}{\partial X_1}\right]^2 + 2\left[\frac{\partial x_1}{\partial X_1}\frac{\partial x_2}{\partial X_2} - \frac{\partial x_1}{\partial X_2}\frac{\partial x_2}{\partial X_1}\right] \\
&= \left[\frac{\partial x_1}{\partial X_1} - \frac{\partial x_2}{\partial X_2}\right]^2 + \left[\frac{\partial x_1}{\partial X_2} + \frac{\partial x_2}{\partial X_1}\right]^2 + 2J.
\end{aligned}$$

Then for any plane strain problem the constraints on the invariants I and J are

$$I \geq 2J, \qquad \text{where} \qquad J > 0. \tag{2.32}$$

Using Eqns. (2.24) and (2.29), the first Piola-Kirchhoff stress tensor for plane strain becomes

$$\mathcal{P} = 2\mathcal{F}\frac{\partial \mathcal{W}}{\partial \mathcal{C}} = 2\mathcal{F}\left[\frac{\partial \mathcal{W}}{\partial I}\frac{\partial I}{\partial \mathcal{C}} + \frac{\partial \mathcal{W}}{\partial J}\frac{\partial J}{\partial \mathcal{C}}\right],$$

which yields:

$$\mathcal{P} = \left(2\frac{\partial \mathcal{W}}{\partial I}\right)\mathcal{F} + \left(J\frac{\partial \mathcal{W}}{\partial J}\right)\mathcal{F}^{-T}. \tag{2.33}$$

Using Eqns. (2.2) and (2.26b), the planar components of the first Piola-Kirchhoff stress tensor are ($i, A = 1, 2$):

$$\mathcal{P}_{iA} = \left(2\frac{\partial \mathcal{W}}{\partial I}\right)\mathcal{F}_{iA} + \tilde{\varepsilon}_{ij}\tilde{\varepsilon}_{AB}\left(\frac{\partial \mathcal{W}}{\partial J}\right)\mathcal{F}_{jB}. \tag{2.34}$$

Using Eqn. (2.18), then

$$\boldsymbol{\sigma} = J^{-1}\boldsymbol{\mathcal{P}}\boldsymbol{\mathcal{F}}^T = J^{-1}\left(\mathcal{P}_{iA}\hat{\mathbf{e}}_i \otimes \hat{\mathbf{E}}_A\right)\left(\mathcal{F}_{jB}\hat{\mathbf{E}}_B \otimes \hat{\mathbf{e}}_j\right) = J^{-1}\,\mathcal{P}_{iA}\mathcal{F}_{jA}\hat{\mathbf{e}}_i \otimes \hat{\mathbf{e}}_j. \tag{2.35}$$

Finally, utilizing (2.34) then the in-plane components of the Cauchy stress tensor are ($i, j = 1, 2$):

$$\sigma_{ij} = J^{-1}\left[\left(2\frac{\partial \mathcal{W}}{\partial I}\right)\mathcal{F}_{iA}\mathcal{F}_{jA} + \tilde{\varepsilon}_{ik}\tilde{\varepsilon}_{AB}\left(\frac{\partial \mathcal{W}}{\partial J}\right)\mathcal{F}_{jA}\mathcal{F}_{kB}\right]. \tag{2.36}$$

If it is required to know the out of plane stresses, note that $\mathcal{F}_{i3} = \mathcal{F}_{3A} = 0$ in plane strain unless $i = 3$ and $A = 3$ in plane strain. Further, $\mathcal{P}_{33}$ can be computed using Eqn. (2.33). Recalling that $[\boldsymbol{\mathcal{F}}]_{33} = 1$ and $[\boldsymbol{\mathcal{F}}^{-T}]_{33} = J^{-1}$, then

$$\mathcal{P}_{33} = 2\frac{\partial \mathcal{W}}{\partial I} + \frac{\partial \mathcal{W}}{\partial J}. \tag{2.37}$$

The out of plane Cauchy stress σ_{33} can be found by using Eqns. (2.33) with (2.35) directly, so that

$$\sigma_{33} = J^{-1}\left[2\frac{\partial \mathcal{W}}{\partial I} + \frac{\partial \mathcal{W}}{\partial J}\right]. \tag{2.38}$$

3 - Problem Formulations

3.1 A General Interface Crack Problem

The visualizations in Figures 1.2a, 1.2b and 1.2c can each be formulated to represent plane strain interface crack problems. Also, recall from Section 2.2 that if the bond dimensions along the $\hat{\mathbf{E}}_3$ axis is much smaller than the length in the $\hat{\mathbf{E}}_1$ axis then displacement in the $\hat{\mathbf{E}}_3$ axis can be assumed negligible. Since failure after loading is expected to happen near the crack tip (defined as the place where the bonded and free edges meet), the problem geometry can be approximated as a semi-infinite plane shown in Figure 3.1. The undeformed material, shown in light gray, resides in the entire upper half plane ($-\infty < X_1 < \infty$ and $X_2 \geq 0$) and the lower half ($-\infty < X_1 < \infty$ and $X_2 \leq 0$) is assumed to be rigid and impenetrable. The origin, where $X_1 = X_2 = 0$ and labeled as 'O', is the interfacial crack tip location and the positive $\hat{\mathbf{E}}_1$ axis ($X_1 > 0$) is the defined as the bonded edge. The negative $\hat{\mathbf{E}}_1$ axis ($X_1 < 0$), denoted by a dashed line, is the crack edge and is assumed to be traction free.

While keeping Cartesian coordinates in the plane, a useful polar transformation can be utilized which lends to the ability to define the problem in Cartesian, but allow for near-field solutions with separable functions of the radial coordinates, namely the radial distance from the crack tip. The Cartesian coordinates each have the polar form

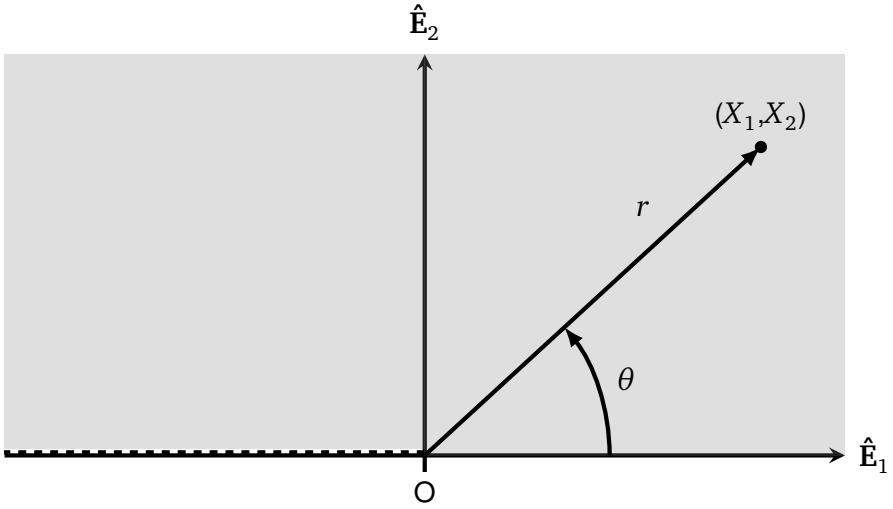

Figure 3.1: The Undeformed Configuration of a Plane Strain Interface Crack Between an Infinite Soft Elastomer and a Rigid Substrate

$$X_A(r,\theta) \equiv r\tilde{\mathbb{C}}_A(\theta), \tag{3.1}$$

where the directional alternator function is defined as

$$\tilde{\mathbb{C}}_A(\theta) \equiv \begin{cases} \cos\theta, & A=1, \\ \sin\theta, & A=2. \end{cases} \tag{3.2}$$

Note that the direction alternator has the derivatives

$$\tilde{\mathbb{C}}'_A(\theta) = -\tilde{\varepsilon}_{AB}\tilde{\mathbb{C}}_B(\theta). \tag{3.3}$$

Using this polar transformation, the elastomer in the upper half plane has the range $r \geq 0$ and $0 \leq \theta \leq \pi$, while the interface crack tip resides at $r = 0$. In polar coordinates, the plane strain components of the referential gradient operator become ($A = 1, 2$)

$$[\nabla_{\mathrm{x}}]_A \equiv \frac{\partial}{\partial X_A} = \frac{\partial r}{\partial X_A}\frac{\partial}{\partial r} + \frac{\partial \theta}{\partial X_A}\frac{\partial}{\partial \theta}.$$

Using this and taking the divergence of the referential coordinate we see

$$\nabla_{\mathrm{x}} \cdot \mathbf{X} = \frac{\partial X_B}{\partial X_A} = \delta_{AB} = \frac{\partial}{\partial X_A}\left(r\tilde{\mathbb{C}}_B\right) = \frac{\partial r}{\partial X_A}\tilde{\mathbb{C}}_B + r\frac{\partial \tilde{\mathbb{C}}_B}{\partial X_A},$$

$$\text{and} \quad \frac{\partial \tilde{\mathbb{C}}_B}{\partial X_A} = \frac{d\tilde{\mathbb{C}}_B}{d\theta}\frac{\partial \theta}{\partial X_A} = \tilde{\varepsilon}_{DB}\tilde{\mathbb{C}}_D\frac{\partial \theta}{\partial X_A}.$$

Combining leaves the following equation set ($A = 1, 2$)

$$\delta_{AB} = \tilde{\mathbb{C}}_B\frac{\partial r}{\partial X_A} + \tilde{\varepsilon}_{DB}\tilde{\mathbb{C}}_D r\frac{\partial \theta}{\partial X_A}.$$

Solving this set of equations yields the plane strain components of the referential gradient operator ∇_{x} in polar coordinates ($A = 1, 2$)

$$[\nabla_{\mathrm{x}}]_A = \frac{\partial}{\partial X_A} = \tilde{\mathbb{C}}_A(\theta)\frac{\partial}{\partial r} - \tilde{\varepsilon}_{AB}\tilde{\mathbb{C}}_B(\theta)\frac{1}{r}\frac{\partial}{\partial \theta}. \tag{3.4}$$

From this, the deformation gradient components become ($i, A = 1, 2$)

$$\mathcal{F}_{iA}(r,\theta) = \tilde{\mathbb{C}}_A(\theta)\frac{\partial x_i}{\partial r} - \tilde{\varepsilon}_{AB}\tilde{\mathbb{C}}_B(\theta)\frac{1}{r}\frac{\partial x_i}{\partial \theta}, \tag{3.5}$$

which extended yields the polar form of the planar invariants I and J. Therefore

$$\begin{aligned}
I &= \mathcal{F}_{11}^2 + \mathcal{F}_{12}^2 + \mathcal{F}_{21}^2 + \mathcal{F}_{22}^2 \\
&= \left[\tilde{\mathbb{C}}_1\frac{\partial x_1}{\partial r} - \tilde{\mathbb{C}}_2\frac{1}{\theta}\frac{\partial x_1}{\partial \theta}\right]^2 + \left[\tilde{\mathbb{C}}_2\frac{\partial x_1}{\partial r} + \tilde{\mathbb{C}}_1\frac{1}{\theta}\frac{\partial x_1}{\partial \theta}\right]^2 \\
&\qquad + \left[\tilde{\mathbb{C}}_1\frac{\partial x_2}{\partial r} - \tilde{\mathbb{C}}_2\frac{1}{\theta}\frac{\partial x_2}{\partial \theta}\right]^2 + \left[\tilde{\mathbb{C}}_2\frac{\partial x_2}{\partial r} + \tilde{\mathbb{C}}_1\frac{1}{\theta}\frac{\partial x_2}{\partial \theta}\right]^2, \quad \text{and} \\
J &= \mathcal{F}_{11}\mathcal{F}_{22} - \mathcal{F}_{12}\mathcal{F}_{21} \\
&= \left[\tilde{\mathbb{C}}_1\frac{\partial x_1}{\partial r} - \tilde{\mathbb{C}}_2\frac{1}{r}\frac{\partial x_1}{\partial \theta}\right]\left[\tilde{\mathbb{C}}_2\frac{\partial x_2}{\partial r} + \tilde{\mathbb{C}}_1\frac{1}{r}\frac{\partial x_2}{\partial \theta}\right] \\
&\qquad - \left[\tilde{\mathbb{C}}_2\frac{\partial x_1}{\partial r} + \tilde{\mathbb{C}}_1\frac{1}{r}\frac{\partial x_1}{\partial \theta}\right]\left[\tilde{\mathbb{C}}_1\frac{\partial x_2}{\partial r} - \tilde{\mathbb{C}}_2\frac{1}{r}\frac{\partial x_2}{\partial \theta}\right],
\end{aligned}$$

so that

$$I(r,\theta) = \left[\frac{\partial x_1}{\partial r}\right]^2 + \left[\frac{\partial x_2}{\partial r}\right]^2 + \left[\frac{1}{r}\frac{\partial x_1}{\partial \theta}\right]^2 + \left[\frac{1}{r}\frac{\partial x_2}{\partial \theta}\right]^2, \tag{3.6a}$$

$$\text{and} \quad J(r,\theta) = \frac{1}{r}\left[\frac{\partial x_1}{\partial r}\frac{\partial x_2}{\partial \theta} - \frac{\partial x_1}{\partial \theta}\frac{\partial x_2}{\partial r}\right]. \tag{3.6b}$$

To get the general plane strain polar form of the governing equations from (2.25), use the polar form of the gradient operator again to get

$$\left[\frac{\partial \mathcal{P}_{11}}{\partial r} + \frac{1}{r}\frac{\partial \mathcal{P}_{12}}{\partial \theta}\right]\cos\theta + \left[\frac{\partial \mathcal{P}_{12}}{\partial r} - \frac{1}{r}\frac{\partial \mathcal{P}_{11}}{\partial \theta}\right]\sin\theta = 0, \tag{3.7a}$$

$$\text{and} \quad \left[\frac{\partial \mathcal{P}_{21}}{\partial r} + \frac{1}{r}\frac{\partial \mathcal{P}_{22}}{\partial \theta}\right]\cos\theta + \left[\frac{\partial \mathcal{P}_{22}}{\partial r} - \frac{1}{r}\frac{\partial \mathcal{P}_{21}}{\partial \theta}\right]\sin\theta = 0. \tag{3.7b}$$

The plane strain gradient components in polar coordinates of the first Piola-Kirchhoff tensor simply require the derivatives of the deformation gradient. Recall Eqn. (3.5), so that ($i, A = 1, 2$)

$$\frac{\partial \mathcal{F}_{iA}}{\partial r} = \tilde{\mathbb{C}}_A \frac{\partial^2 x_i}{\partial r^2} - \tilde{\varepsilon}_{AB}\tilde{\mathbb{C}}_B\left[\frac{1}{r}\frac{\partial^2 x_i}{\partial r \partial \theta} - \frac{1}{r^2}\frac{\partial x_i}{\partial \theta}\right], \tag{3.8a}$$

$$\frac{1}{r}\frac{\partial \mathcal{F}_{iA}}{\partial \theta} = \tilde{\mathbb{C}}_A\left[\frac{1}{r}\frac{\partial^2 x_i}{\partial r \partial \theta} - \frac{1}{r^2}\frac{\partial x_i}{\partial \theta}\right] - \tilde{\varepsilon}_{AB}\tilde{\mathbb{C}}_B\left[\frac{1}{r}\frac{\partial x_i}{\partial r} + \frac{1}{r^2}\frac{\partial^2 x_i}{\partial \theta^2}\right]. \tag{3.8b}$$

The governing equations can not be solved without the boundary conditions. First, recall the edge at $\theta = \pi$ (so that $\mathfrak{N} = -\hat{\mathbf{E}}_2$) is traction free, and an equilibrium force balance requires

$$\mathbf{0} = \mathfrak{P}\mathfrak{N} = \left(\mathcal{P}_{iA}\hat{\mathbf{e}}_i \otimes \hat{\mathbf{E}}_A\right)\left(-\hat{\mathbf{E}}_2\right) = -\mathcal{P}_{i2}\hat{\mathbf{e}}_i,$$

so that $\mathcal{P}_{12}(r,\pi) = \mathcal{P}_{22}(r,\pi) = 0$. Using Eqns. (2.34), (3.5) then ($i = 1, 2$)

$$0 = \left(2\frac{\partial \mathcal{W}}{\partial I}\right)\mathcal{F}_{i2}(r,\pi) - \tilde{\varepsilon}_{ij}\left(\frac{\partial \mathcal{W}}{\partial J}\right)\mathcal{F}_{j1}(r,\pi).$$

Finally, the two boundary conditions at the traction free edge become ($i = 1, 2$)

$$\left[\left(2\frac{\partial \mathcal{W}}{\partial I}\right)\left(\frac{1}{r}\frac{\partial x_i}{\partial \theta}\right) - \tilde{\varepsilon}_{ij}\left(\frac{\partial \mathcal{W}}{\partial J}\right)\left(\frac{\partial x_j}{\partial r}\right)\right]_{\theta=\pi} = 0,$$

which yields

$$\left[\left(2\frac{\partial \mathcal{W}}{\partial I}\right)\left(\frac{1}{r}\frac{\partial x_1}{\partial \theta}\right) - \left(\frac{\partial \mathcal{W}}{\partial J}\right)\left(\frac{\partial x_2}{\partial r}\right)\right]_{\theta=\pi} = 0, \tag{3.9a}$$

$$\text{and} \quad \left[\left(2\frac{\partial \mathcal{W}}{\partial I}\right)\left(\frac{1}{r}\frac{\partial x_2}{\partial \theta}\right) + \left(\frac{\partial \mathcal{W}}{\partial J}\right)\left(\frac{\partial x_1}{\partial r}\right)\right]_{\theta=\pi} = 0. \tag{3.9b}$$

The boundary condition on the bonded edge requires deeper consideration. A detailed discussion is given in Section 3.2.

3.2 Bonded Boundary Conditions

The bonded surface is shown on the positive $\hat{\mathbf{E}}_1$ axis in Figure 3.1, and corresponds to the planar polar coordinates $\theta = 0$ and $r \geq 0$. For the geometry shown in Figure 3.1, the in-plane surface traction vectors $\mathbf{t}$ and $\mathcal{T}$ on the bonded surface have the form ($i = 1, 2$)

$$\mathbf{t}(r, 0) = \left(\sigma_{ij}\hat{\mathbf{e}}_i \otimes \hat{\mathbf{e}}_j\right)(-\hat{\mathbf{e}}_2) = -\sigma_{i2}\hat{\mathbf{e}}_i, \qquad \therefore \quad t_i = -\sigma_{i2},$$

$$\text{and} \quad \mathcal{T}(r, 0) = \left(\mathcal{P}_{ij}\hat{\mathbf{e}}_i \otimes \hat{\mathbf{E}}_A\right)\left(-\hat{\mathbf{E}}_2\right) = -\mathcal{P}_{i2}\hat{\mathbf{e}}_i, \qquad \therefore \quad \mathcal{T}_i = -\mathcal{P}_{i2},$$

where $i = 1$ and $i = 2$ represent lateral and normal tractions respectively. Using Eqn. (2.36), the form of t_1 and t_2 can be imposed using any of the available traction-separation relationships [20, 21, 74] where the opening displacement in the lateral and normal cases in the near field are equivalent to the displacements u_1 and u_2. In most cases, the traction-separation is only expressed in the normal direction u_2 and $u_1 = 0$. However, since the main theme of this work is to determine the effect of interfacial slippage we shall assume the reverse, and for all cases considered let $u_2 = 0$ on the bonded edge ($\theta = 0$) so

that

$$x_2(r,0) = 0. \tag{3.10}$$

With this condition, note that it is also required that

$$\left[\frac{\partial x_2}{\partial r}\right]_{\theta=0} = 0, \quad \text{and} \quad \mathcal{F}_{21}(r,0) = \cos(0)\cancelto{0}{\left[\frac{\partial x_2}{\partial r}\right]_{\theta=0}} - \cancelto{0}{\sin(0)}\left[\frac{1}{r}\frac{\partial x_2}{\partial \theta}\right]_{\theta=0} = 0.$$

To model interfacial slip, the first major case to consider is the highest extent of interfacial friction so that zero in-plane displacements on the bonded surface are allowed. With infinite maximum friction, we define the 'no-slip' case where $u_1(r,0) = u_2(r,0) = 0$. Utilizing Eqns. (3.1) and (3.2) this boundary condition simplifies to

$$x_1(r,0) = r. \tag{3.11}$$

With the no-slip case, the traction components t_1 and t_2 are unknown and will be resultant stresses from the displacement constraint $u_1(r,0) = u_2(r,0) = 0$.

If interfacial slip is allowed but not encumbered, we have the opposing extent of interfacial friction to the no-slip case and call this the 'frictionless' case. Here, the interfacial traction condition in the $\hat{\mathbf{E}}_1$ direction is defined as $\mathcal{P}\mathbf{N}\cdot\hat{\mathbf{E}}_1 = 0$, so that $\mathcal{P}_{12}(r,0) = 0$ and using Eqn. (3.5):

$$0 = \left(2\frac{\partial \mathcal{W}}{\partial I}\right)\mathcal{F}_{12}(r,0) - \left(\frac{\partial \mathcal{W}}{\partial J}\right)\cancelto{0}{\mathcal{F}_{21}(r,0)} = \left(2\frac{\partial \mathcal{W}}{\partial I}\right)\left(\frac{1}{r}\frac{\partial x_1}{\partial \theta}\right).$$

Therefore, without a loss of generality the frictionless case boundary condition becomes

$$\left[\frac{\partial x_1}{\partial \theta}\right]_{\theta=0} = 0. \tag{3.12}$$

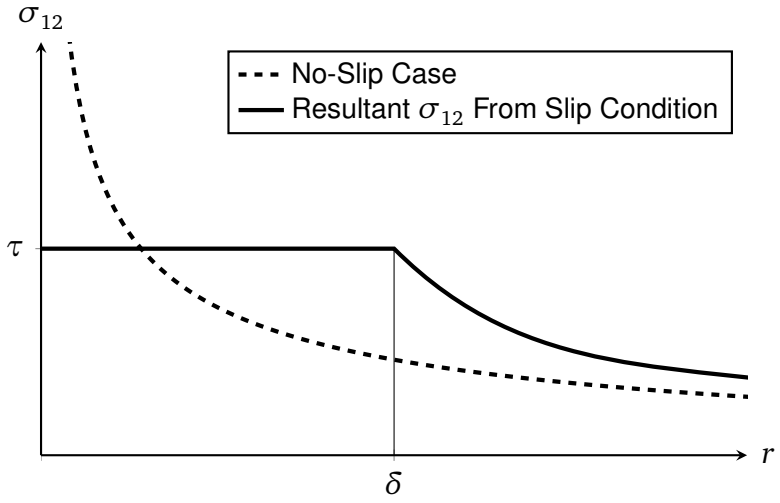

Figure 3.2: Visualization of a constant finite friction threshold boundary condition and slip zone region

In the finite friction case, slippage is allowed to occur as in the frictionless case, however the condition must have some non-zero, finite stress along the bonded edge. Park and Paulino [74] discussed several traction-separation relationships for cohesive zone models that are commonly utilized to describe fracture, notably being some polynomial, exponential or linear expression between the induced traction and opening displacement. Taking the simplest form of traction-separation relationships, we can assume this interface traction is a constant value τ with opening displacement inside of some 'slip zone.' This basic form of a 'slip-zone' model (an interfacial slip cohesive zone) has multiple interpretations. The first being the similarity to the Dugdale-Barenblatt model [91, 21, 92, 93] using a constant stress, but in the lateral direction as opposed to the normal direction. Another interpretation of this idea is that interfacial slippage is allowed only if the shear stress magnitude on the bonded edge is exceeded, or when

$$|\sigma_{12}(r,0)| \leq |\tau|. \tag{3.13}$$

A visualization of this idea is shown in Figure 3.2, where inside of some arbitrary finite

slip-zone length δ, the no-slip case result is re-adjusted (lowered) to the maximum threshold value τ. The sign of τ here is not restricted and can be positive or negative, but is assumed to be a real constant. Using a force balance in the deformed configuration inside the slip zone region, then $\sigma_{12}(r,0)=\tau$ and using Eqns. (3.5), (3.6b) and (2.36)

$$\begin{aligned}\tau &= J^{-1}\left[\left(2\frac{\partial \mathcal{W}}{\partial I}\right)\left(\mathcal{F}_{11}\cancelto{0}{\mathcal{F}_{21}}+\mathcal{F}_{12}\mathcal{F}_{22}\right)+\left(\frac{\partial \mathcal{W}}{\partial J}\right)(\cancel{\mathcal{F}_{21}\mathcal{F}_{22}}-\cancel{\mathcal{F}_{22}\mathcal{F}_{21}})\right]_{\theta=0}\\ &= J^{-1}\left(2\frac{\partial \mathcal{W}}{\partial I}\right)\left(\frac{1}{r^2}\frac{\partial x_1}{\partial \theta}\frac{\partial x_2}{\partial \theta}\right), \qquad \text{and}\\ J(r,0) &= \frac{1}{r}\frac{\partial x_1}{\partial r}\frac{\partial x_2}{\partial \theta}-\frac{1}{r}\frac{\partial x_1}{\partial \theta}\cancelto{0}{\frac{\partial x_2}{\partial r}}\ .\end{aligned}$$

Since $J>0$, then

$$\left[\frac{1}{r}\frac{\partial x_2}{\partial \theta}\right]_{\theta=0}\neq 0, \quad \text{and} \quad \left[\frac{\partial x_1}{\partial r}\right]_{\theta=0}\neq 0,$$

and re-arranging yields the general finite friction boundary condition,

$$\left[\left(2\frac{\partial \mathcal{W}}{\partial I}\right)\left(\frac{1}{r}\frac{\partial x_1}{\partial \theta}\right)-\tau\frac{\partial x_1}{\partial r}\right]_{\theta=0}=0. \tag{3.14}$$

3.3 Summary of Plane-Strain Interface Crack Problems

The general plane strain bonded interface crack eigenvalue problem requires Eqns. (3.7), (3.9), and the required bonded edge conditions for each of the three bonding cases, which were: no-slip, frictionless and finite friction. The generalized problems are summarized in Table 3.1. It should be noted that the finite friction problem (the third column) collapses to the frictionless problem (the second column) when the bonded friction threshold $\tau \to 0$ as expected.

It must also be noted here that the far-field boundary conditions (as $r \to \infty$) are not

shown in the problem summary in Table 3.1. Without the far-field conditions, we are left with an eigenvalue problem which will be shown in Chapter 4 to be approximated analytically near a point of interest. The far-field conditions are discussed in more detail in Chapter 6.

Table 3.1: Summary of the three plane strain interface crack eigenvalue problems.

No-Slip Case	**Frictionless Case**	**Finite Friction Case**
General Governing Eqns. (3.7a) **&** (3.7b)**: in** $r \geq 0$**, and** $0 \leq \theta \leq \pi$**.** $\left[\frac{\partial \mathcal{P}_{11}}{\partial r} + \frac{1}{r}\frac{\partial \mathcal{P}_{12}}{\partial \theta}\right]\cos\theta + \left[\frac{\partial \mathcal{P}_{12}}{\partial r} - \frac{1}{r}\frac{\partial \mathcal{P}_{11}}{\partial \theta}\right]\sin\theta = 0$ $\left[\frac{\partial \mathcal{P}_{21}}{\partial r} + \frac{1}{r}\frac{\partial \mathcal{P}_{22}}{\partial \theta}\right]\cos\theta + \left[\frac{\partial \mathcal{P}_{22}}{\partial r} - \frac{1}{r}\frac{\partial \mathcal{P}_{21}}{\partial \theta}\right]\sin\theta = 0$		
Traction Free Boundary Condition Eqns. (3.9a) **&** (3.9b)**: on** $\theta = \pi$**.** $\left(2\frac{\partial \mathcal{W}}{\partial I}\right)\left(\frac{1}{r}\frac{\partial x_1}{\partial \theta}\right) - \left(\frac{\partial \mathcal{W}}{\partial J}\right)\left(\frac{\partial x_2}{\partial r}\right) = 0$ $\left(2\frac{\partial \mathcal{W}}{\partial I}\right)\left(\frac{1}{r}\frac{\partial x_2}{\partial \theta}\right) + \left(\frac{\partial \mathcal{W}}{\partial J}\right)\left(\frac{\partial x_1}{\partial r}\right) = 0$		
Bonded Boundary Condition: on $\theta = 0$**.**		
Eqns. (3.11) & (3.10)	**Eqns.** (3.12) & (3.10)	**Eqns.** (3.14) & (3.10)
$x_1 = r$	$\frac{\partial x_1}{\partial \theta} = 0$	$\left(2\frac{\partial \mathcal{W}}{\partial I}\right)\left(\frac{1}{r}\frac{\partial x_1}{\partial \theta}\right) - \tau\frac{\partial x_1}{\partial r} = 0$
$x_2 = 0$	$x_2 = 0$	$x_2 = 0$

3.4 A Class of Hyperelastic Rubber

Water based and chemically bonded adhesives are well modeled as soft elastomers [94]. Knowles introduced the generalized Neo-Hookean (GNH) material model [83] for an incompressible ($J = 1$) soft elastomer. This model, which has been used to model soft elastomers with various crack problems [49, 50, 51, 52], utilizes a 'stiffening' parameter η and has a strain energy density function in the form

$$\psi = \frac{\mu}{2b}\left[\left(1+\frac{b}{\eta}(I_1-3)\right)^{\eta}-1\right]. \tag{3.15}$$

Here, b is a material parameter, μ represents the linear small strain shear modulus. The material parameters μ, b and η must be positive and non-zero. When $\eta = 1$, Eqn. (3.15) reduces to the Neo-Hookean material strain energy density function [34, 41]

$$\psi(I_1, I_2, I_3) = \frac{\mu}{2}(I_1-3). \tag{3.16}$$

The states of stiffening represented by the GNH model in Eqn. (3.15) depend on the value of η; for example $\eta > 1$ represents a positive 'shear stiffening' and $0 < \eta < 1$ is a state of 'shear softening' [83].

For biological tissue, the Ogden model [95, 34] is also an incompressible elastomer that has the strain energy density function

$$\psi = \sum_{i=1}^{N}\frac{\mu_i}{\alpha_i}\left[\sum_{j=1}^{3}\lambda_j^{\alpha_i}-3\right], \tag{3.17}$$

where $\mu_i\alpha_i > 0$, λ_1, λ_2, and λ_3 are the principal stretches, and N is a positive integer representing the number of material correlations used. These principal stretches are related to the three principal invariants by [95, 39, 40, 41, 34]

$$I_1 \equiv \lambda_1^2+\lambda_2^2+\lambda_3^2, \tag{3.18a}$$

$$I_2 \equiv \lambda_1^2\lambda_2^2+\lambda_2^2\lambda_3^2+\lambda_3^2\lambda_1^2, \tag{3.18b}$$

$$\text{and} \quad I_3 \equiv \lambda_1^2\lambda_2^2\lambda_3^2. \tag{3.18c}$$

When $N = 1$, Eqn. (3.17) also results in the Neo-Hookean material strain energy function from Eqn. (3.16).

The 'Power Law Material' introduced by Stephenson [80], is presented using the plane

strain asymptotic relationship of the first plane strain invariant I defined in Eqn. (2.28), with a stiffening parameter η (power):

$$\psi = AI^{\eta} + BI^{\eta-1} + \mathcal{O}\left(I^{\eta-1}\right), \qquad \text{as} \quad I \to \infty. \tag{3.19}$$

This incompressible material model is a more theoretical take on the GNH model, and again with the stiffening parameter $\eta = 1$, $A = \mu/2$ and taking $B = -\mu$ we arrive at the Neo-Hookean model [80].

Given the connections and simplicity, the Neo-Hookean material model from Eqn. (3.16) showed potential. Unfortunately, solutions (using the techniques outlined in Chapters 4 and 5) attempted with this model did not yield useful results. The details are omitted here, however due to the incompressibility requirement ($J = 1$ in Eqn. (2.31b)), it was not possible to furnish a solution that satisfies both the bulk material governing Eqn. (2.25) and the boundary conditions on the free bonded from Eqn. (3.11). A partial explanation for the inability to yield a near-field deformation field in separable functions of the polar coordinates r and θ [81] is that it is expected that the wedge angle ϕ (recall Figure 1.1b) for the GNH, an incompressible material, was nearly flat (i.e. $\theta \simeq 0$) which could mean infinite compression inside and near the crack front.

Blatz and Ko introduced a class of compressible foam rubber [47, 96] with the strain energy density function

$$\psi = \frac{\mu}{2}\left[f I_1 + (1-f)\,\frac{I_2}{I_3} - 3\right] + \frac{\mu}{2\beta}\left(I_3^{-\beta} - 1\right). \tag{3.20}$$

The parameter f represents the void content (for example, air bubbles) in the rubber material. The parameter β is a measure of material compressibility and is related to the Poisson's ratio ν by the expression

$$\beta \equiv \frac{\nu}{1-2\nu}. \tag{3.21}$$

Eqn. (3.20) can be simplified if we assume that there is negligible dilation in the material after loading from voids (i.e. we assume there are no air bubbles in our adhesive material), then let $f = 1$ [47] to get

$$\psi = \frac{\mu}{2}(I_1 - 3) + \frac{\mu}{2\beta}\left(I_3^{-\beta} - 1\right). \tag{3.22}$$

Using the relations from Eqn. (2.29), the Blatz-Ko strain energy density function has the plane strain form

$$\mathcal{W}(I,J) = \frac{\mu}{2}\left(I - 2 + \frac{1}{\beta}\left[J^{-2\beta} - 1\right]\right). \tag{3.23}$$

While the expression in Eqn. (3.23) is for plane strain, for the special case when $\beta = 1$ we find the same relation to the the plane stress formulation of the GNH material model from Eqn. (3.15) with the stiffening parameter $\eta = 1$ [83, 50]. Also, if we assume that for 'nearly incompressible' materials that $J \simeq 1$ (hence $I_3 \simeq 1$) and $\nu \to 1/2$, then $\beta \to \infty$ and the second terms in Eqns. (3.22) and (3.23) vanish so that we converge to the Neo-Hookean case from Eqn. (3.16). While insight from Stephensons 'power-law' [80] could be utilized to model a strain stiffening parameter, none was found in literature and the Blatz-Ko model from Eqn. (3.20) does not inherently incorporate strain stiffening. However, the compressibility material parameter β may account for effects worth studying. Given the relation of this model to the Neo-Hookean, which is commonly used as a simple model for most other elastomers mentioned here, it is of interest to continue with this material model and we shall proceed with the plane strain, compressible Blatz-Ko strain energy function given by Eqn. (3.23).

3.5 Bonded Interface Problems with Blatz-Ko Material

The derivatives with respect to the planar invariants I and J of the Blatz-Ko strain energy function $\mathcal{W}$ from Eqn. (3.23) are

$$\frac{\partial \mathcal{W}}{\partial I} = \frac{\mu}{2}, \qquad \text{and} \qquad \frac{\partial \mathcal{W}}{\partial J} = -\frac{\mu}{J^{2\beta+1}},$$

so that the in-plane components of the first Piola-Kirchhoff and Cauchy stress tensors from Eqns. (2.34), and (2.36) respectively become ($i, A = 1, 2$)

$$\mathcal{P}_{iA} = \mu \left[\mathcal{F}_{iA} - \tilde{\varepsilon}_{ij} \tilde{\varepsilon}_{AB} J^{-(2\beta+1)} \mathcal{F}_{jB} \right], \tag{3.24}$$

$$\sigma_{ij} = \mu J^{-1} \left[\mathcal{F}_{iA} \mathcal{F}_{jA} - \tilde{\varepsilon}_{ik} \tilde{\varepsilon}_{AB} J^{-(2\beta+1)} \mathcal{F}_{jA} \mathcal{F}_{kB} \right]. \tag{3.25}$$

The components of the deformation gradient $\mathcal{F}$ are computed using Eqn. (3.5), from which the in-plane components of the Cauchy stress tensor can be determined, where

$$\sigma_{11} = \mu J^{-1} \left[\mathcal{F}_{11}^2 + \mathcal{F}_{12}^2 - J^{-2\beta} \right], \tag{3.26a}$$

$$\sigma_{12} = \sigma_{21} = \mu J^{-1} \left[\mathcal{F}_{11} \mathcal{F}_{21} + \mathcal{F}_{12} \mathcal{F}_{22} \right], \tag{3.26b}$$

$$\text{and} \quad \sigma_{22} = \mu J^{-1} \left[\mathcal{F}_{21}^2 + \mathcal{F}_{22}^2 - J^{-2\beta} \right]. \tag{3.26c}$$

Also, using Eqn. (3.8) the gradient terms of the first Piola-Kirchhoff tensor are:

$$\frac{\partial \mathcal{P}_{iA}}{\partial r} = \mu \left[\frac{\partial \mathcal{F}_{iA}}{\partial r} - \tilde{\varepsilon}_{ij} \tilde{\varepsilon}_{AB} \left(J^{-(2\beta+1)} \frac{\partial \mathcal{F}_{jB}}{\partial r} - (2\beta+1) J^{-2(\beta+1)} \frac{\partial J}{\partial r} \mathcal{F}_{jB} \right) \right],$$

$$\frac{1}{r} \frac{\partial \mathcal{P}_{iA}}{\partial \theta} = \frac{\mu}{r} \left[\frac{\partial \mathcal{F}_{iA}}{\partial \theta} - \tilde{\varepsilon}_{ij} \tilde{\varepsilon}_{AB} \left(J^{-(2\beta+1)} \frac{\partial \mathcal{F}_{jB}}{\partial \theta} - (2\beta+1) J^{-2(\beta+1)} \frac{\partial J}{\partial \theta} \mathcal{F}_{jB} \right) \right],$$

and the governing material Eqn. (3.7) becomes

$$
\begin{aligned}
0 &= \tilde{\mathbb{C}}_A \left[\frac{\partial \mathcal{F}_{iA}}{\partial r} - \tilde{\varepsilon}_{ij}\tilde{\varepsilon}_{AB} \left(J^{-(2\beta+1)} \frac{\partial \mathcal{F}_{jB}}{\partial r} - (2\beta+1) J^{-2(\beta+1)} \frac{\partial J}{\partial r} \mathcal{F}_{jB} \right) \right] \\
&\quad - \tilde{\varepsilon}_{AB} \frac{\tilde{\mathbb{C}}_B}{r} \left[\frac{\partial \mathcal{F}_{iA}}{\partial \theta} - \tilde{\varepsilon}_{ij}\tilde{\varepsilon}_{AB} \left(J^{-(2\beta+1)} \frac{\partial \mathcal{F}_{jB}}{\partial \theta} - (2\beta+1) J^{-2(\beta+1)} \frac{\partial J}{\partial \theta} \mathcal{F}_{jB} \right) \right] \\
&= \tilde{\mathbb{C}}_A^2 \frac{\partial^2 x_i}{\partial r^2} - \tilde{\varepsilon}_{AB}\tilde{\mathbb{C}}_B\tilde{\mathbb{C}}_A \left[\frac{1}{r} \frac{\partial^2 x_i}{\partial r \partial \theta} - \frac{1}{r^2} \frac{\partial x_i}{\partial \theta} \right] - \tilde{\varepsilon}_{ij}\tilde{\varepsilon}_{AB} J^{-(2\beta+1)} \tilde{\mathbb{C}}_A\tilde{\mathbb{C}}_B \frac{\partial^2 x_j}{\partial r^2} \\
&\quad + \tilde{\varepsilon}_{ij}\tilde{\varepsilon}_{AB}\tilde{\varepsilon}_{BD} J^{-(2\beta+1)} \tilde{\mathbb{C}}_A\tilde{\mathbb{C}}_D \left[\frac{1}{r} \frac{\partial^2 x_j}{\partial r \partial \theta} - \frac{1}{r^2} \frac{\partial x_j}{\partial \theta} \right] \\
&\quad + (2\beta+1)\tilde{\varepsilon}_{ij}\tilde{\varepsilon}_{AB}\tilde{\mathbb{C}}_A J^{-2(\beta+1)} \frac{\partial J}{\partial r} \left[\tilde{\mathbb{C}}_B \frac{\partial x_j}{\partial r} - \tilde{\varepsilon}_{BD}\tilde{\mathbb{C}}_D \frac{1}{r} \frac{\partial x_j}{\partial \theta} \right] \\
&\quad - \tilde{\varepsilon}_{AB}\tilde{\mathbb{C}}_A\tilde{\mathbb{C}}_B \left[\frac{1}{r} \frac{\partial^2 x_i}{\partial r \partial \theta} - \frac{1}{r^2} \frac{\partial x_i}{\partial \theta} \right] + \tilde{\mathbb{C}}_B^2 \left[\frac{1}{r} \frac{\partial x_i}{\partial r} + \frac{1}{r^2} \frac{\partial^2 x_i}{\partial \theta^2} \right] \\
&\quad + \tilde{\varepsilon}_{ij}\tilde{\mathbb{C}}_B J^{-(2\beta+1)} \left(\tilde{\mathbb{C}}_B \left[\frac{1}{r} \frac{\partial^2 x_j}{\partial r \partial \theta} - \frac{1}{r^2} \frac{\partial x_j}{\partial \theta} \right] - \tilde{\varepsilon}_{BD}\tilde{\mathbb{C}}_D \left[\frac{1}{r} \frac{\partial x_j}{\partial r} + \frac{1}{r^2} \frac{\partial^2 x_j}{\partial \theta^2} \right] \right) \\
&\quad - \tilde{\varepsilon}_{ij}\tilde{\mathbb{C}}_B (2\beta+1) J^{-2(\beta+1)} \frac{1}{r} \frac{\partial J}{\partial \theta} \left[\tilde{\mathbb{C}}_B \frac{\partial x_j}{\partial r} - \tilde{\varepsilon}_{BD}\tilde{\mathbb{C}}_D \frac{1}{r} \frac{\partial x_j}{\partial \theta} \right].
\end{aligned}
$$

Using the definition from Eqn. (3.2), then

$$
\tilde{\varepsilon}_{AB}\tilde{\varepsilon}_{BD}\tilde{\mathbb{C}}_A\tilde{\mathbb{C}}_D = \tilde{\varepsilon}_{AB}\tilde{\varepsilon}_{BA}\tilde{\mathbb{C}}_A^2 = -\tilde{\mathbb{C}}_A^2, \qquad \tilde{\mathbb{C}}_A^2 = \tilde{\mathbb{C}}_B^2 = \tilde{\mathbb{C}}_1^2 + \tilde{\mathbb{C}}_2^2 = 1,
$$

$$
\text{and} \quad \tilde{\varepsilon}_{AB}\tilde{\mathbb{C}}_A\tilde{\mathbb{C}}_B = \tilde{\varepsilon}_{12}\tilde{\mathbb{C}}_1\tilde{\mathbb{C}}_2 + \tilde{\varepsilon}_{21}\tilde{\mathbb{C}}_2\tilde{\mathbb{C}}_1 = 0,
$$

so that

$$
\begin{aligned}
0 &= \frac{\partial^2 x_i}{\partial r^2} - \cancel{\tilde{\varepsilon}_{ij} J^{-(2\beta+1)} \left[\frac{1}{r} \frac{\partial^2 x_j}{\partial r \partial \theta} - \frac{1}{r^2} \frac{\partial x_j}{\partial r} \right]} + (2\beta+1) J^{-2(\beta+1)} \tilde{\varepsilon}_{ij} \frac{\partial J}{\partial r} \left(\frac{1}{r} \frac{\partial x_j}{\partial \theta} \right) \\
&\quad + \frac{1}{r} \frac{\partial x_i}{\partial r} + \frac{1}{r^2} \frac{\partial^2 x_i}{\partial \theta^2} + \cancel{\tilde{\varepsilon}_{ij} J^{-(2\beta+1)} \left[\frac{1}{r} \frac{\partial^2 x_j}{\partial r \partial \theta} - \frac{1}{r^2} \frac{\partial x_j}{\partial r} \right]} \\
&\quad - \tilde{\varepsilon}_{ij} (2\beta+1) J^{-2(\beta+1)} \left(\frac{1}{r} \frac{\partial J}{\partial \theta} \right) \frac{\partial x_j}{\partial r},
\end{aligned}
$$

and finally, the two governing equations ($i = 1, 2$) simplify to

$$\nabla_x^2 x_1 + (2\beta+1) J^{-2(\beta+1)} |\nabla_x J \times \nabla_x x_2| = 0, \tag{3.27a}$$

$$\text{and} \quad \nabla_x^2 x_2 - (2\beta+1) J^{-2(\beta+1)} |\nabla_x J \times \nabla_x x_1| = 0, \tag{3.27b}$$

where the operators are defined as

$$\nabla_x^2 x_i \equiv \nabla_x \cdot (\nabla_x x_i) = \frac{\partial^2 x_i}{\partial r^2} + \frac{1}{r}\frac{\partial x_i}{\partial r} + \frac{1}{r^2}\frac{\partial^2 x_i}{\partial \theta^2}, \tag{3.28a}$$

$$\text{and} \quad \left|\nabla_x J \times \nabla_x x_j\right| \equiv \frac{1}{r}\left[\frac{\partial J}{\partial r}\frac{\partial x_j}{\partial \theta} - \frac{\partial J}{\partial \theta}\frac{\partial x_j}{\partial r}\right]. \tag{3.28b}$$

Using the Blatz-Ko strain energy density function from Eqn. (3.23), the boundary conditions on the free edge from Eqn. (3.9) are

$$\left[\frac{1}{r}\frac{\partial x_1}{\partial \theta} + J^{-(2\beta+1)}\frac{\partial x_2}{\partial r}\right]_{\theta=\pi} = 0, \tag{3.29a}$$

$$\text{and} \quad \left[\frac{1}{r}\frac{\partial x_2}{\partial \theta} - J^{-(2\beta+1)}\frac{\partial x_1}{\partial r}\right]_{\theta=\pi} = 0. \tag{3.29b}$$

The boundary condition on the bonded edge ($\theta = 0$) is then found by applying the material model to the equations in Table 3.1. From this, Eqn. (3.14) has the specific form

$$\left[\frac{1}{r}\frac{\partial x_1}{\partial \theta} - \xi\frac{\partial x_1}{\partial r}\right]_{\theta=0} = 0, \tag{3.30}$$

where the non-dimensional stress threshold ξ is defined as

$$\xi \equiv \frac{\tau}{\mu}. \tag{3.31}$$

The interface crack problems using the Blatz-Ko material model are given by Eqns. (3.27), (3.29), and the bonded edge conditions are summarized in Table 3.2. Again, as expected the finite friction problem (the third column) collapses to the Frictionless problem when the bonded friction threshold $\tau \to 0$ (or $\xi \to 0$).

Table 3.2: Summary of the plane strain interface crack problems with the Blatz-Ko material.

No-Slip Case	**Frictionless Case**	**Finite Friction Case**
General Governing Eqns. (3.27a) **&** (3.27b)**: in** $r \geq 0$**, and** $0 \leq \theta \leq \pi$**.** $\nabla_x^2 x_1 + (2\beta+1)J^{-2(\beta+1)}\,\lvert\nabla_x J \times \nabla_x x_2\rvert = 0$ $\nabla_x^2 x_2 - (2\beta+1)J^{-2(\beta+1)}\,\lvert\nabla_x J \times \nabla_x x_1\rvert = 0$		
Traction Free Boundary Condition Eqns. (3.29a) **&** (3.29b)**: on** $\theta = \pi$**.** $\frac{1}{r}\frac{\partial x_1}{\partial \theta} + J^{-(2\beta+1)}\frac{\partial x_2}{\partial r} = 0$ $\frac{1}{r}\frac{\partial x_2}{\partial \theta} - J^{-(2\beta+1)}\frac{\partial x_1}{\partial r} = 0$		
Bonded Boundary Condition: on $\theta = 0$**.**		
Eqns. (3.11) & (3.10)	**Eqns.** (3.12) & (3.10)	**Eqns.** (3.30) & (3.10)
$x_1 = r$ $x_2 = 0$	$\frac{\partial x_1}{\partial \theta} = 0$ $x_2 = 0$	$\frac{1}{r}\frac{\partial x_1}{\partial \theta} - \xi\frac{\partial x_1}{\partial r} = 0$ $x_2 = 0$

Part II

Analytical Solutions

4 - Asymptotic Analysis

The three BVPs summarized in Table 3.2 do not show all the boundary conditions required to solve them globally. However, since we are looking only for solutions close to the crack tip it is possible to determine a solution near $r \to 0$, bypassing the need for far field conditions. Each BVP then becomes an eigenvalue problem where the geometry of the general equations for the deformed coordinates are found, however undetermined constants remain. Asymptotic analysis [73] is used to determine a local near-field solution for each BVP in the following sections.

4.1 The Frictionless Bonding Case

Recall the frictionless case is governed by Eqns. (3.27), (3.29), (3.10) and (3.12), being

$$
\begin{aligned}
&\nabla_{\mathrm{x}}^2 x_1 + (2\beta+1) J^{-2(\beta+1)} |\nabla_{\mathrm{x}} J \times \nabla_{\mathrm{x}} x_2| = 0, && \text{in} \quad 0 \le \theta \le \pi, \\
&\nabla_{\mathrm{x}}^2 x_2 - (2\beta+1) J^{-2(\beta+1)} |\nabla_{\mathrm{x}} J \times \nabla_{\mathrm{x}} x_1| = 0, && \text{in} \quad 0 \le \theta \le \pi, \\
&\frac{1}{r}\frac{\partial x_1}{\partial \theta} + J^{-(2\beta+1)} \frac{\partial x_2}{\partial r} = 0, \qquad \frac{1}{r}\frac{\partial x_2}{\partial \theta} - J^{-(2\beta+1)} \frac{\partial x_1}{\partial r} = 0, && \text{on} \quad \theta = \pi, \\
&\frac{\partial x_1}{\partial \theta} = 0, \qquad x_2 = 0, && \text{on} \quad \theta = 0.
\end{aligned}
$$

The solution to the problem of interest is only required near the crack tip, and to determine the nature of deflection, first look for near field deflection in the form ($i = 1, 2$)

$$x_i(r,\theta) = \bar{x}_i + r^m v_i(\theta) + \mathfrak{o}(r^m), \qquad \text{as} \quad r \to 0, \tag{4.1}$$

where v_1 and v_2 are arbitrary functions of θ. The term $\mathfrak{o}(r^m)$ represents 'Little-O' notation [73], meaning that $\mathfrak{o}(r^m)$ converges to a value which is less dominant than r^m as $r \to 0$. Conversely, Little-O is different than 'Big-O' notation $\mathcal{O}(r^m)$, which indicates an expression which is equally dominant to r^m as $r \to 0$. To ensure the deflection field is finite [27, 79] and non-oscillating [79, 76, 75, 97, 22, 17, 98], then it is required that the constant m be positive and real. To ensure finite contractions (recall that $J > 0$), then it is also required that the constant $m < 1$ [27] so that the range of the exponent m is

$$0 < m < 1. \tag{4.2}$$

Taking the derivative of Eqn. (4.1) yields

$$\frac{\partial x_i}{\partial r} = m r^{m-1} v_i(\theta) + \mathfrak{o}\left(r^{m-1}\right), \qquad \frac{1}{r}\frac{\partial x_i}{\partial \theta} = r^{m-1} v_i'(\theta) + \mathfrak{o}\left(r^{m-1}\right),$$
$$\text{and} \quad \nabla_{\mathrm{x}}^2 x_i = \left[v_i''(\theta) + m^2 v_i(\theta)\right] r^{m-2} + \mathfrak{o}\left(r^{m-2}\right).$$

From this, the plane strain invariants from Eqns. (3.6a) and (3.6b) become

$$I(r,\theta) = \left[m^2\left(v_1^2 + v_2^2\right) + \left(v_1'\right)^2 + \left(v_2'\right)^2\right] r^{2(m-1)} + \mathfrak{o}\left(r^{2(m-1)}\right),$$
$$\text{and} \quad J(r,\theta) = m\left[v_1 v_2' - v_1' v_2\right] r^{2(m-1)} + \mathfrak{o}\left(r^{2(m-1)}\right).$$

Since $\nabla_{\mathrm{x}} x_i = \mathcal{O}\left(r^{m-1}\right)$ and $J = \mathcal{O}\left(r^{2(m-1)}\right)$, then the boundary conditions from Eqns. (3.29), (3.10) and (3.12) require

$$\bar{x}_2 = 0, \quad v_1'(0) = 0, \quad v_2(0) = 0, \quad v_1'(\pi) = 0, \quad \text{and} \quad v_2'(\pi) = 0. \tag{4.3}$$

The $\nabla_x^2 x_i$ terms in the governing Eqns. (3.27) are most dominant as $r \to 0$, hence for $i = 1, 2$

$$v_i(\theta) = A_i \sin(m\theta) + B_i \cos(m\theta), \tag{4.4}$$

where A_i and B_i are arbitrary constants. From Eqn. (4.3), then $A_1 = B_2 = 0$,

$$B_1 \sin(m\pi) = 0, \quad \text{and} \quad A_2 \cos(m\pi) = 0.$$

Since $0 < m < 1$, it is determined that $B_1 = 0$, hence $v_1(\theta) = 0$, $m = 1/2$ and without a loss in generality

$$v_2(\theta) = a \sin(\theta/2), \tag{4.5}$$

where a is an arbitrary constant. Then the near-field displacement components are

$$x_1(r, \theta) = \bar{x}_1 + \mathcal{O}\left(r^{1/2}\right),$$
$$\text{and} \quad x_2(r, \theta) = a r^{1/2} \sin(\theta/2) + \mathcal{O}\left(r^{1/2}\right).$$

Since the shear traction is zero on the bonded edge, then slippage is expected and the arbitrary constant $\bar{x}_1$ represents the lateral deflection of the crack tip after loading. Here, there is not yet enough information to be useful given that this leads to a degenerate expression for J because $J(r, \theta) = \mathcal{O}\left(r^{2(m-1)}\right)$. Given this, further terms are required, and so an expanded form of the deformed coordinates are assumed to be

$$x_1(r, \theta) = \bar{x}_1 + r^n w_1(\theta) + \mathcal{O}(r^n), \tag{4.6a}$$
$$\text{and} \quad x_2(r, \theta) = a r^{1/2} \sin(\theta/2) + r^n w_2(\theta) + \mathcal{O}(r^n), \tag{4.6b}$$

where w_1 and w_2 are arbitrary functions of θ and the constant $n > 1/2$. The derivatives become

$$\frac{\partial x_1}{\partial r} = nr^{n-1}w_1(\theta) + \mathcal{O}\left(r^{n-1}\right), \tag{4.7a}$$

$$\frac{1}{r}\frac{\partial x_1}{\partial \theta} = r^{n-1}w_1'(\theta) + \mathcal{O}\left(r^{n-1}\right), \tag{4.7b}$$

$$\frac{\partial x_2}{\partial r} = \tfrac{1}{2}ar^{-1/2}\sin(\theta/2) + nr^{n-1}w_2(\theta) + \mathcal{O}\left(r^{n-1}\right), \tag{4.7c}$$

$$\frac{1}{r}\frac{\partial x_2}{\partial \theta} = \tfrac{1}{2}ar^{-1/2}\cos(\theta/2) + r^{n-1}w_2'(\theta) + \mathcal{O}\left(r^{n-1}\right), \tag{4.7d}$$

and $$\nabla_x^2 x_i = \left[w_i''(\theta) + n^2 w_i(\theta)\right] r^{n-2} + \mathcal{O}\left(r^{n-2}\right). \tag{4.7e}$$

Using this, the most dominant first terms of J as $r \to 0$ become

$$J(r,\theta) = \chi(\theta)r^{n-3/2} + \mathcal{O}\left(r^{n-3/2}\right), \tag{4.8}$$

$$\text{where} \quad \chi(\theta) \equiv \tfrac{1}{2}a\left[nw_1(\theta)\cos(\theta/2) - w_1'(\theta)\sin(\theta/2)\right]. \tag{4.9}$$

Note that $\nabla_x x_1 = \mathcal{O}\left(r^{n-1}\right)$, $\nabla_x x_2 = \mathcal{O}\left(r^{-1/2}\right)$, $J = \mathcal{O}\left(r^{n-3/2}\right)$, and therefore $\nabla_x J = \mathcal{O}\left(r^{n-5/2}\right)$. It is not clear at this point which terms in the governing body equations (3.27) or the free end conditions in (3.29) are most dominant. To determine this, consider the difference in the power of r in each term from Eqn. (3.27a) as

$$\eta \equiv -2(\beta+1)(n-3/2) + (n-5/2) + (-1/2) - (n-2). \tag{4.10}$$

In the event that $\eta < 0$, then the right hand term of Eqn. (3.27a) is most dominant and recalling that $J > 0$ then

$$(n-3/2)\chi(\theta)\cos(\theta/2) - \chi'(\theta)\sin(\theta/2) = 0,$$

which implies

$$\frac{\frac{1}{2}a\sin(\pi/2)}{[\chi(\pi)]^{2\beta+1}} = 0 \qquad \Longrightarrow \quad \therefore \quad \frac{-1}{w_1'(\pi)} = 0.$$

This is not physically reasonable because it results in an infinite deflection on the free edge, therefore this case is rejected and it must be that $\eta \geq 0$. If $\eta = 0$, both terms in the first governing body Eqn. (3.27a) have the same dominance as $r \to 0$, leading to the non-linear ordinary differential equation (ODE)

$$\frac{d^2w_1}{d\theta^2} + n^2 w_1 + \frac{a(2\beta+1)}{2\chi^{2(\beta+1)}}\left[(n-\tfrac{3}{2})\chi\cos(\theta/2) - \frac{d\chi}{d\theta}\sin(\theta/2)\right] = 0. \tag{4.11}$$

Eqn. (4.11) with the boundary conditions in Eqns. (3.29a) and (3.12) has no apparent analytical solution and was found numerically to have no solution for any positive β [1]. Given this, it is required that the left hand term in Eqn. (3.27a) is most dominant and since $\eta > 0$, then

$$\frac{1}{2} < n < \frac{3\beta+2}{2\beta+2}, \tag{4.12}$$

so that (for $i = 1, 2$)

$$w_i(\theta) = A_i\sin(n\theta) + B_i\cos(n\theta), \tag{4.13}$$

where A_i and B_i are arbitrary constants. Using the boundary conditions from Eqns. (3.29), (3.12) and (3.10)

$$w_2(0) = 0, \quad w_1'(0) = 0, \quad w_1'(\pi) = 0, \quad \text{and} \quad w_2'(\pi) = 0.$$

Immediately, we see $A_1 = B_2 = 0$ and with the range from Eqn. (4.12) then $A_2 = 0$ and $n = 1$. By assuming b is a real constant, then the deflected coordinates in the frictionless case as $r \to 0$ are

$$x_1(r,\theta) = \bar{x}_1 + br\cos\theta + \mathcal{O}(r), \tag{4.14a}$$

and $$x_2(r,\theta) = ar^{1/2}\sin(\theta/2) + \mathcal{O}(r). \tag{4.14b}$$

The stress field for the frictionless bonded case can be computed from Eqns. (4.14) by utilizing Eqn. (3.25). Recall the deformation gradient components from Eqn. (3.5)

$$\begin{aligned}
\mathcal{F}_{11} &= \cos\theta(b\cos\theta) - \sin\theta(-b\sin\theta) + \mathcal{O}(1),\\
\mathcal{F}_{12} &= \sin\theta(b\cos\theta) + \cos\theta(-b\sin\theta) + \mathcal{O}(1),\\
\mathcal{F}_{21} &= \cos\theta\left(\tfrac{1}{2}ar^{-1/2}\sin(\theta/2)\right) - \sin\theta\left(\tfrac{1}{2}ar^{-1/2}\cos(\theta/2)\right) + \mathcal{O}(1),\\
\mathcal{F}_{22} &= \sin\theta\left(\tfrac{1}{2}ar^{-1/2}\sin(\theta/2)\right) + \cos\theta\left(\tfrac{1}{2}ar^{-1/2}\cos(\theta/2)\right) + \mathcal{O}(1),
\end{aligned}$$

which becomes

$$\mathcal{F}_{11}(r,\theta) = b + \mathcal{O}(1), \tag{4.15a}$$

$$\mathcal{F}_{12}(r,\theta) = \mathcal{O}(1), \tag{4.15b}$$

$$\mathcal{F}_{21}(r,\theta) = -\tfrac{1}{2}ar^{-1/2}\sin(\theta/2) + \mathcal{O}(1), \tag{4.15c}$$

and $$\mathcal{F}_{22}(r,\theta) = \tfrac{1}{2}ar^{-1/2}\cos(\theta/2) + \mathcal{O}(1). \tag{4.15d}$$

Using Eqns. (3.6a), (3.6b) and (4.28) with the result in (4.15), the plane-strain invariants have the form

$$\begin{aligned}
I &= b^2 + \mathcal{O}(1) + \tfrac{1}{4}a^2r^{-1} + \mathcal{O}\left(r^{-1/2}\right),\\
J &= (b\cos\theta)\left(\tfrac{1}{2}ar^{-1/2}\cos(\theta/2)\right) - (-b\sin\theta)\left(\tfrac{1}{2}ar^{-1/2}\sin(\theta/2)\right) + \mathcal{O}\left(r^{-1/2}\right),
\end{aligned}$$

where

$$I(r,\theta) = \tfrac{1}{4}a^2 r^{-1} + \mathfrak{o}\big(r^{-1/2}\big), \tag{4.16a}$$

$$\text{and} \quad J(r,\theta) = \tfrac{1}{2}abr^{-1/2}\cos(\theta/2) + \mathfrak{o}\big(r^{-1/2}\big). \tag{4.16b}$$

With Eqns. (4.16a) and (4.16b), the strain energy density function from (3.23) has the near-field form

$$\mathcal{W} = \tfrac{1}{2}\mu\left(\tfrac{1}{4}a^2 r^{-1} + \mathfrak{o}\big(r^{-1/2}\big) - 2 + \frac{1}{\beta}\big[\mathcal{O}\big(r^{\beta}\big) - 1\big]\right),$$

therefore

$$\mathcal{W}(r,\theta) = \tfrac{1}{8}\mu a^2 r^{-1} + \mathfrak{o}\big(r^{-1/2}\big). \tag{4.16c}$$

Also, utilizing the result from Eqns. (4.16a) and (4.16b) with Eqns. (3.26a) through (3.26c) the stress components are

$$\begin{aligned}
\sigma_{11} &= \mu\big[\tfrac{1}{2}abr^{-1/2}\cos(\theta/2)\big]^{-1}\big[b^2 + \mathfrak{o}(1) + \mathcal{O}\big(r^{\beta}\big)\big],\\
\sigma_{12} = \sigma_{21} &= \mu\big[\tfrac{1}{2}abr^{-1/2}\cos(\theta/2)\big]^{-1}\big[-\tfrac{1}{2}abr^{-1/2}\sin(\theta/2) + \mathfrak{o}\big(r^{-1/2}\big)\big], \quad \text{and}\\
\sigma_{22} &= \mu\big[\tfrac{1}{2}abr^{-1/2}\cos(\theta/2)\big]^{-1}\big[\tfrac{1}{4}a^2 r^{-1} + \mathfrak{o}(1)\big] - \big[\tfrac{1}{2}abr^{-1/2}\cos(\theta/2)\big]^{-(2\beta+1)}.
\end{aligned}$$

Therefore, for any $\beta > 0$

$$\sigma_{11}(r,\theta) = \mu\left(\frac{2b}{a}\right)r^{1/2}\sec(\theta/2) + \mathfrak{o}\big(r^{1/2}\big), \tag{4.17a}$$

$$\sigma_{12}(r,\theta) = -\mu\tan(\theta/2) + \mathfrak{o}(1), \tag{4.17b}$$

$$\text{and} \quad \sigma_{22}(r,\theta) = \mu\left(\frac{a}{2b}\right)r^{-1/2}\sec(\theta/2) + \mathfrak{o}\big(r^{-1/2}\big). \tag{4.17c}$$

This provides the useful part of the near field approximation for the frictionless case, and the deformation and stress field approximations are summarized in Table 4.1.

Table 4.1: Summary of the Asymptotic Solution near $r \to 0$ for the frictionless case.

Field Type	**Near Field Approximation Equations Near** $r = 0$
Deformation:	Eqns. (4.14a), $x_1 \simeq \bar{x}_1 + br\cos\theta$
	(4.14b): $x_2 \simeq ar^{1/2}\sin(\theta/2)$
Stress:	Eqns. (4.17a), $\sigma_{11} \simeq \mu\left(\frac{2b}{a}\right) r^{1/2}\sec(\theta/2)$
	(4.17b), $\sigma_{12} = \sigma_{21} \simeq -\mu\tan(\theta/2)$
	(4.17c): $\sigma_{22} \simeq \mu\left(\frac{a}{2b}\right) r^{-1/2}\sec(\theta/2)$
Scalar	Eqns. (4.16a), $I \simeq \frac{1}{4}a^2 r^{-1}$
Functions:	(4.16b): $J \simeq \frac{1}{2}abr^{-1/2}\cos(\theta/2)$
	(4.16c), $\mathcal{W} \simeq \frac{1}{8}\mu a^2 r^{-1}$

Recall that Geubelle et al [50] studied the general crack problem using the GNH material in plane stress, which is the equivalent problem posed here for the specific case when the compressibility parameter $\beta = 1$ and the hardening parameter is chosen as unity. In Geubelle's work, the orders of r matched the solution here and the angular variation (i.e. the separable functions of θ in the asymptotic analysis) were numerically plotted and confirmed the solutions of the deformation field from Eqns. (4.14). The general crack problems by Stephenson [80] and Knowles and Sternberg [79] were shown to have a the same order $\mathcal{O}(r)$ for the second term in x_1 (Eqn. (4.14a)), however the angular variation was $\sin^2(\theta/2)$ instead of $\cos\theta$. This difference is attributed to the finding that Stephenson, Knowles and Sternberg utilized incompressible material formulations ($J = 1$) which would require in our case the arbitrary function $w_1(\theta) = [\sin(\theta/2)]^{n/m}$, and recall it was determined that $n = 1$ and $m = 1/2$.

4.2 The No-Slip Bonding Case

The eigenvalue problem to solve for the no-slip case is defined by Eqns. (3.27), (3.29), (3.10) and (3.11) is given by

$$
\begin{aligned}
&\nabla_{\mathrm{x}}^2 x_1 + (2\beta+1)J^{-2(\beta+1)}|\nabla_{\mathrm{x}} J \times \nabla_{\mathrm{x}} x_2| = 0, && \text{in} \quad 0 \le \theta \le \pi,\\
&\nabla_{\mathrm{x}}^2 x_2 - (2\beta+1)J^{-2(\beta+1)}|\nabla_{\mathrm{x}} J \times \nabla_{\mathrm{x}} x_1| = 0, && \text{in} \quad 0 \le \theta \le \pi,\\
&\frac{1}{r}\frac{\partial x_1}{\partial \theta} + J^{-(2\beta+1)}\frac{\partial x_2}{\partial r} = 0, \qquad \frac{1}{r}\frac{\partial x_2}{\partial \theta} - J^{-(2\beta+1)}\frac{\partial x_1}{\partial r} = 0, && \text{on} \quad \theta = \pi,\\
&x_1 = r, \qquad x_2 = 0, && \text{on} \quad \theta = 0.
\end{aligned}
$$

Like the frictionless case, look for near-field solutions (as $r \to 0$) in the form of Eqn. (4.1) ($i = 1, 2$)

$$x_i(r,\theta) = \bar{x}_i + r^m v_i(\theta) + \mathcal{O}(r^m),$$

where v_i are arbitrary functions of θ, $\bar{x}_1$ and $\bar{x}_2$ are arbitrary constants, and $0 < m < 1$. The first BCs are revealed using Eqn. (4.1) with Eqns. (3.10), (3.11), and (3.29), so that

$$\bar{x}_1 = \bar{x}_2 = 0, \quad v_1(0) = v_2(0) = 0, \quad \text{and} \quad v_1'(\pi) = v_2'(\pi) = 0. \tag{4.18}$$

Similar to the frictionless case, the $\nabla_{\mathrm{x}}^2 x_i$ terms in the body Eqns. (3.27) are most dominant as $r \to 0$, yielding a solution in the form of Eqn. (4.4). With the boundary conditions, the first near-field terms are determined and following the same procedure as the frictionless case:

$$
\begin{aligned}
&x_1(r,\theta) = a_1 r^{1/2}\sin(\theta/2) + \mathcal{O}\left(r^{1/2}\right),\\
\text{and} \quad &x_2(r,\theta) = a_2 r^{1/2}\sin(\theta/2) + \mathcal{O}\left(r^{1/2}\right).
\end{aligned}
$$

This is a slightly different result than the opposing extent shown by the frictionless case and in general $a_1 \neq 0$. However, like the frictionless case it is noted that with only the first asymptotic terms for the deformed coordinates x_1 and x_2, then $J = \mathcal{O}\left(r^{2(m-2)}\right)$. Given this, it is required to gain more terms and so we proceed with a proposed solution in the form

$$x_1(r,\theta) = a_1 r^{1/2}\sin(\theta/2) + r^n w_1(\theta) + \mathcal{O}(r^n), \tag{4.19a}$$

$$\text{and} \quad x_2(r,\theta) = a_2 r^{1/2}\sin(\theta/2) + r^n w_2(\theta) + \mathcal{O}(r^n), \tag{4.19b}$$

where w_1 and w_2 are arbitrary functions of θ and the constant $n > 1/2$. Using Eqns. (3.10), (3.11), and (3.29) the boundary conditions for w_1 and w_2 are

$$w_1'(0) = \begin{cases} 0, & \text{if } n \neq 1 \\ \\ 1, & \text{if } n = 1 \end{cases}, \quad w_2(0) = 0, \quad w_1'(\pi) = 0, \quad \text{and} \quad w_2'(\pi) = 0.$$

Given the boundary condition for $w_1(0)$, it is required that $n \leq 1$ in order to obtain a non-contradictory result so that $1/2 < n \leq 1$. With this range for n, the $\nabla_x^2 x_i$ terms are most dominant as $r \to 0$ concluding (for $i = 1, 2$)

$$w_i''(\theta) + n^2 w_i(\theta) = 0, \tag{4.20}$$

which has a solution in the form of Eqn. (4.13). Using the boundary conditions it is concluded that $n = 1$ requiring that $w_1(\theta) = \cos\theta$, $w_2(\theta) = 0$ and the near-field solution becomes

$$x_1(r,\theta) = a_1 r^{1/2}\sin(\theta/2) + r\cos\theta + \mathcal{O}(r), \tag{4.21a}$$

$$\text{and} \quad x_2(r,\theta) = a_2 r^{1/2}\sin(\theta/2) + \mathcal{O}(r). \tag{4.21b}$$

Using Eqns. (3.6a) and (3.6b), the plane-strain invariants become

$$
\begin{aligned}
I &= \left[\tfrac{1}{2}a_1 r^{-1/2}\sin(\theta/2) + \cos\theta + \mathfrak{o}(1)\right]^2 + \left[\tfrac{1}{2}a_1 r^{-1/2}\cos(\theta/2) - \sin\theta + \mathfrak{o}(1)\right]^2 \\
&\quad + \left[\tfrac{1}{2}a_2 r^{-1/2}\sin(\theta/2) + \mathfrak{o}(1)\right]^2 + \left[\tfrac{1}{2}a_2 r^{-1/2}\cos(\theta/2) + \mathfrak{o}(1)\right]^2 \\
&= \tfrac{1}{4}\left(a_1^2 + a_2^2\right) r^{-1} + a_1 r^{-1/2}\left[\sin(\theta/2)\cos\theta - \cos(\theta/2)\sin\theta\right] + \mathfrak{o}\left(r^{-1/2}\right), \quad \text{and} \\
J &= \left[\tfrac{1}{2}a_1 r^{-1/2}\sin(\theta/2) + \cos\theta + \mathfrak{o}(1)\right]\left[\tfrac{1}{2}a_2 r^{-1/2}\cos(\theta/2) + \mathfrak{o}(1)\right] \\
&\quad - \left[\tfrac{1}{2}a_1 r^{-1/2}\cos(\theta/2) - \sin\theta + \mathfrak{o}(1)\right]\left[\tfrac{1}{2}a_2 r^{-1/2}\sin(\theta/2) + \mathfrak{o}(1)\right] \\
&= \tfrac{1}{4}a_1 a_2 r^{-1}\sin(\theta/2)\cos(\theta/2) + \tfrac{1}{2}a_2 r^{-1/2}\cos\theta\cos(\theta/2) + \mathfrak{o}\left(r^{-1/2}\right) \\
&\quad - \tfrac{1}{4}a_1 a_2 r^{-1}\sin(\theta/2)\cos(\theta/2) + \tfrac{1}{2}a_2 r^{-1/2}\sin\theta\sin(\theta/2),
\end{aligned}
$$

therefore

$$
I(r,\theta) = \tfrac{1}{4}\left(a_1^2 + a_2^2\right) r^{-1} - a_1 r^{-1/2}\sin(\theta/2) + \mathfrak{o}\left(r^{-1/2}\right), \tag{4.22a}
$$

$$
\text{and} \quad J(r,\theta) = \tfrac{1}{2}a_2 r^{-1/2}\cos(\theta/2) + \mathfrak{o}\left(r^{-1/2}\right). \tag{4.22b}
$$

The near-field strain energy density function from Eqn. (3.23) is quantified using Eqns. (4.22a) and (4.22b), where

$$
\mathcal{W} = \tfrac{1}{2}\mu\left(\tfrac{1}{4}\left(a_1^2 + a_2^2\right) r^{-1} - a_1 r^{-1/2}\sin(\theta/2) + \mathfrak{o}\left(r^{-1/2}\right) - 2 + \frac{1}{\beta}\left[\mathcal{O}\left(r^{\beta}\right) - 1\right]\right),
$$

so that

$$
\mathcal{W}(r,\theta) = \tfrac{1}{8}\mu\left[\left(a_1^2 + a_2^2\right) r^{-1} - 4a_1 r^{-1/2}\sin(\theta/2)\right] + \mathfrak{o}\left(r^{-1/2}\right). \tag{4.22c}
$$

Using Eqn. (3.5), the deformation gradient components become

$$
\begin{aligned}
\mathcal{F}_{11} &= \cos\theta\left(\tfrac{1}{2}a_1 r^{-1/2}\sin(\theta/2) + \cos\theta\right) - \sin\theta\left(\tfrac{1}{2}a_2 r^{-1/2}\cos(\theta/2) - \sin\theta\right) + \mathfrak{o}(1) \\
\mathcal{F}_{12} &= \sin\theta\left(\tfrac{1}{2}a_1 r^{-1/2}\sin(\theta/2) + \cos\theta\right) + \cos\theta\left(\tfrac{1}{2}a_1 r^{-1/2}\cos(\theta/2) - \sin\theta\right) + \mathfrak{o}(1)
\end{aligned}
$$

$$\mathcal{F}_{21} = \cos\theta\left(\tfrac{1}{2}a_2 r^{-1/2}\sin(\theta/2)\right) - \sin\theta\left(\tfrac{1}{2}a_2 r^{-1/2}\cos(\theta/2)\right) + o(1)$$
$$\mathcal{F}_{22} = \sin\theta\left(\tfrac{1}{2}a_2 r^{-1/2}\sin(\theta/2)\right) + \cos\theta\left(\tfrac{1}{2}a_2 r^{-1/2}\cos(\theta/2)\right) + o(1),$$

which yields

$$\mathcal{F}_{11}(r,\theta) = -\tfrac{1}{2}a_1 r^{-1/2}\sin(\theta/2) + 1 + o(1), \tag{4.23a}$$
$$\mathcal{F}_{12}(r,\theta) = \tfrac{1}{2}a_1 r^{-1/2}\cos(\theta/2) + o(1), \tag{4.23b}$$
$$\mathcal{F}_{21}(r,\theta) = -\tfrac{1}{2}a_2 r^{-1/2}\sin(\theta/2) + o(1), \tag{4.23c}$$
and $$\mathcal{F}_{22}(r,\theta) = \tfrac{1}{2}a_2 r^{-1/2}\cos(\theta/2) + o(1). \tag{4.23d}$$

Combining the deformation gradient components from Eqns. (4.23) with (3.26) and (4.22b), the Cauchy stress is

$$\sigma_{11} = \mu\left[\tfrac{1}{2}a_2 r^{-1/2}\cos(\theta/2)\right]^{-1}\left[\tfrac{1}{4}a_1^2 r^{-1} - a_1 r^{-1/2}\sin(\theta/2) + o\left(r^{-1/2}\right) + \mathcal{O}\left(r^{\beta}\right)\right],$$
$$\sigma_{12} = \mu\left[\tfrac{1}{2}a_2 r^{-1/2}\cos(\theta/2)\right]^{-1}\left[\tfrac{1}{4}a_1 a_2 r^{-1} - \tfrac{1}{2}a_2 r^{-1/2}\sin(\theta/2) + o\left(r^{-1/2}\right)\right],$$
$$\sigma_{22} = \mu\left[\tfrac{1}{2}a_2 r^{-1/2}\cos(\theta/2)\right]^{-1}\left[\tfrac{1}{4}a_2^2 r^{-1} + o\left(r^{-1/2}\right) + \mathcal{O}\left(r^{\beta}\right)\right],$$

which, after some algebra yields for any $\beta > 0$

$$\sigma_{11}(r,\theta) = \tfrac{1}{2}\mu a_1 a_2^{-1}\left[a_1 r^{-1/2}\sec(\theta/2) - 4\tan(\theta/2)\right] + o(1), \tag{4.24a}$$
$$\sigma_{12}(r,\theta) = \sigma_{21}(r,\theta) = \tfrac{1}{2}\mu\left[a_1 r^{-1/2}\sec(\theta/2) - 2\tan(\theta/2)\right] + o(1), \tag{4.24b}$$
and $$\sigma_{22}(r,\theta) = \tfrac{1}{2}\mu a_2 r^{-1/2}\sec(\theta/2) + o(1). \tag{4.24c}$$

The near-field deflection and stress field approximations close to the crack tip ($r \to 0$) for the no-slip case are summarized in Table 4.2

Confirmation of this solution can also be found from Geubelle et al [51] where the GNH

model in plane stress was used to analyze an interface crack bonded to a rigid substrate (the same problem presented in this section). With the special case of $\beta = 1$ in the present Blatz-Ko plane strain case and turning off the stiffening effect in the GNH model, the problem formulations are the same and solutions from Eqns. (4.21), (4.22a), (4.22b) visually matched the plots of the various numerical solutions produced by Geubelle et al [51].

Table 4.2: Summary of the asymptotic solution near $r \to 0$ for the no-slip Case.

Field Type	**Near Field Approximation Equations Near** $r = 0$
Deformation:	Eqns. (4.21a), $x_1 \simeq a_1 r^{1/2}\sin(\theta/2) + r\cos\theta$
	(4.21b): $x_2 \simeq a_2 r^{1/2}\sin(\theta/2)$
Stress:	Eqns. (4.24a), $\sigma_{11} \simeq \frac{1}{2}\mu a_1 a_2^{-1}\left[a_1 r^{-1/2}\sec(\theta/2) - 4\tan(\theta/2)\right]$
	(4.24b), $\sigma_{12} = \sigma_{21} \simeq \frac{1}{2}\mu\left[a_1 r^{-1/2}\sec(\theta/2) - 2\tan(\theta/2)\right]$
	(4.24c): $\sigma_{22} \simeq \frac{1}{2}\mu a_2 r^{-1/2}\sec(\theta/2)$
Scalar Functions:	Eqns. (4.22a), $I \simeq \frac{1}{4}\left(a_1^2 + a_2^2\right) r^{-1} - a_1 r^{-1/2}\sin(\theta/2)$
	(4.22b): $J \simeq \frac{1}{2} a_2 r^{-1/2}\cos(\theta/2)$
	(4.22c): $\mathcal{W} \simeq \frac{1}{8}\mu\left[\left(a_1^2 + a_2^2\right) r^{-1} - 4a_1 r^{-1/2}\sin(\theta/2)\right]$

4.3 The Finite Friction Bonding Case

Recall from the third column in Table 3.2 that the eigenvalue problem to for the finite friction case is defined by Eqns. (3.27), (3.29), (3.10) and (3.30) and is given by

$$\nabla_x^2 x_1 + (2\beta+1)J^{-2(\beta+1)}\left|\nabla_x J \times \nabla_x x_2\right| = 0, \qquad \text{in} \quad 0 \le \theta \le \pi,$$

$$\nabla_x^2 x_2 - (2\beta+1)J^{-2(\beta+1)}\left|\nabla_x J \times \nabla_x x_1\right| = 0, \qquad \text{in} \quad 0 \le \theta \le \pi,$$

$$\frac{1}{r}\frac{\partial x_1}{\partial \theta} + J^{-(2\beta+1)}\frac{\partial x_2}{\partial r} = 0, \qquad \frac{1}{r}\frac{\partial x_2}{\partial \theta} - J^{-(2\beta+1)}\frac{\partial x_1}{\partial r} = 0, \qquad \text{on} \quad \theta = \pi,$$

$$\frac{1}{r}\frac{\partial x_1}{\partial \theta} - \xi \frac{\partial x_1}{\partial r} = 0, \qquad x_2 = 0, \qquad \text{on} \quad \theta = 0.$$

Again, assume a solution in the form of Eqn. (4.1), being

$$x_i(r,\theta) = \bar{x}_1 + r^m v_i(\theta) + \mathcal{O}(r^m).$$

From here, the technique is identical to the frictionless case from Section 4.1 and using the boundary conditions from Eqns. (3.10), (3.29), & (3.30)

$$\bar{x}_2 = 0, \quad v_1'(0) - m\xi v_1(0) = 0, \quad v_2(0) = 0, \quad v_1'(\pi) = 0, \quad \text{and} \quad v_2'(\pi) = 0,$$

so that the governing equations (3.27) yields the form from Eqn. (4.4) ($i = 1, 2$)

$$v_i(\theta) = A_i \sin(m\pi) + B_i \cos(m\theta).$$

For $i = 1$, the boundary conditions require that $A_1 = \xi B_1 = \tan(m\pi)$, hence $\xi = \tan(m\pi)$. However, using $i = 2$, it is determined that $B_2 = 0$ and $A_2 \cos(m\pi) = 0$ which yields $m = 1/2$ and $v_2 = a \sin(\theta/2)$. Since there is no finite value for ξ that satisfies $\xi = \tan(\pi/2)$, it is required that both $A_1 = B_1 = 0$ so that $v_1(\theta) = 0$. Hence, we have the same result as the frictionless case so far and proceed directly to the same expanded form in Eqn. (4.6):

$$\begin{aligned} & x_1(r,\theta) = \bar{x}_1 + r^n w_1(\theta) + \mathcal{O}(r^n), \\ \text{and} \quad & x_2(r,\theta) = a r^{1/2} \sin(\theta/2) + r^n w_2(\theta) + \mathcal{O}(r^n), \end{aligned}$$

where w_1 and w_2 are arbitrary functions of θ and $n > 1/2$. The derivatives were already worked out as the set in Eqns. (4.7)

$$\frac{\partial x_1}{\partial r} = n r^{n-1} w_1(\theta) + \mathcal{O}\left(r^{n-1}\right), \qquad \frac{1}{r}\frac{\partial x_1}{\partial \theta} = r^{n-1} w_1'(\theta) + \mathcal{O}\left(r^{n-1}\right),$$

$$\frac{\partial x_2}{\partial r} = \tfrac{1}{2} a r^{-1/2} \sin(\theta/2) + n r^{n-1} w_2(\theta) + \mathcal{O}\left(r^{n-1}\right),$$
$$\frac{1}{r}\frac{\partial x_2}{\partial \theta} = \tfrac{1}{2} a r^{-1/2} \cos(\theta/2) + r^{n-1} w_2'(\theta) + \mathcal{O}\left(r^{n-1}\right),$$
$$\nabla_x^2 x_i = \left[w_i''(\theta) + n^2 w_i(\theta)\right] r^{n-2} + \mathcal{O}\left(r^{n-2}\right),$$

and $$J = \chi(\theta) r^{n-3/2} + \mathcal{O}\left(r^{n-3/2}\right),$$

where the definition for χ is given in Eqn. (4.9),

$$\chi(\theta) \equiv \tfrac{1}{2} a \left[n w_1(\theta) \cos(\theta/2) - w_1'(\theta) \sin(\theta/2)\right].$$

Here, it is again not clear which terms are most dominant in the governing Eqn. (3.27a). Recall the exponent difference defined in Eqn. (4.10) was

$$\eta \equiv -2(\beta+1)(n-3/2) + (n-5/2) + (-1/2) - (n-2).$$

When $\eta < 0$, we get the same contradiction as the frictionless case where no finite value for $w_1'(\pi)$ is possible. When $\eta = 0$ we are left with the non-linear ordinary differential equation in the form of Eqn. (4.11). A numerical solution may exist for certain ranges of ξ and β of the problem defined by Eqns. (4.11), (3.29a) and (3.30) however it does not allow for a closed form analytical solution. Since a full numerical study is done in Part III, this is not pursued and we look for a closed form algebraic solution and proceed with the case that $\eta > 0$ so that we have the range given by Eqn. (4.12), where

$$\frac{1}{2} < n < \frac{3\beta+2}{2\beta+2},$$

and for $i = 1, 2$, then

$$w_i(\theta) = A_i \sin(n\theta) + B_i \cos(n\theta),$$

where A_i and B_i are arbitrary constants. Using the boundary conditions from Eqns. (3.29), (3.30) and (3.10)

$$w_1'(0) - n\xi w_1(0) = 0, \quad w_2(0) = 0 \quad w_1'(\pi) = 0, \quad \text{and} \quad w_2'(\pi) = 0.$$

For w_1, we find $A_1 = \xi B_1$ so that

$$\xi = \tan(n\pi). \tag{4.25}$$

Note that the expression in Eqn. (4.25) is periodic and provides an infinite number of values for n, meaning for any arbitrary angle Θ and integer N

$$\tan\Theta = \tan\left(\Theta \pm N\pi\right). \tag{4.26}$$

The other set requires that $B_2 = 0$ and either $n = 1/2$ (a contradiction given the range for n in Eqn. (4.12)), or $A_2 = 0$, making $w_2(0) = 0$. Also, using the range from Eqn. (4.12), then for any $\beta > 0$, we define the 'blunting parameter' $\bar{n}$ as the unique value of n from Eqn. (4.25) which is the only viable value that satisfies the eigenvalue problem and assumptions made. So

$$\bar{n}(\xi) \equiv 1 + \frac{1}{\pi}\tan^{-1}\xi, \tag{4.27}$$

and without a lack of generality,

$$x_1(r,\theta) = \bar{x}_1 + br^{\bar{n}}w(\theta) + \mathcal{O}\left(r^{\bar{n}}\right), \tag{4.28a}$$

$$\text{and} \quad x_2(r,\theta) = ar^{1/2}\sin(\theta/2) + \mathcal{O}\left(r^{\bar{n}}\right), \tag{4.28b}$$

where b is an arbitrary constant and the angular variation function $w(\theta)$ is defined as

$$w(\theta) \equiv \xi \sin(\bar{n}\theta) + \cos(\bar{n}\theta). \tag{4.29}$$

With the definition of $\bar{n}$ from Eqn. (4.27), then given Eqn. (4.12) the limited allowable range for ξ is

$$\frac{1}{2} < 1 + \frac{1}{\pi}\tan^{-1}\xi < \frac{3\beta+2}{2\beta+2} \quad \Longrightarrow \quad \therefore \quad -\frac{\pi}{2} < \tan^{-1}\xi < \frac{\pi}{2}\left(\frac{\beta}{\beta+1}\right),$$

so that

$$-\infty < \xi < \tan\left[\frac{\pi}{2}\left(\frac{\beta}{\beta+1}\right)\right]. \tag{4.30}$$

From this, there are a few important details worth noting. First, the limited range for ξ is a result of the analysis, but means that the solution for the deformation field from Eqns. (4.28) is viable only in the range given by (4.30). So, with highly compressible materials (which have low β) the results here may not be useful. However, for nearly incompressible materials, β is large and there is a larger admissible range for ξ therefore it should be these cases where this model is used. The second thing to note here is that the solution in Eqns. (4.28) indeed converges to the frictionless case when $\xi = 0$. This is expected given that the formulated problem for the finite friction case also converged to the frictionless case. However, also note that when $\xi \neq 0$, then the value of $\bar{n} \neq 1$ and can be less than or greater than unity depending on the sign of the stress threshold ξ.

The sign of ξ depends on the slip threshold induced on the bonded surface. Recall that this is a threshold value on the bonded surface after loading and therefore this method requires solving the no-slip condition solved in Section 4.2 first, and noting the sign of the constant a_1 from Eqns. (4.24b) and (4.21a). Cases where $\xi < 0$ indicate that the shear on the bonded edge has a negative value and threshold since $\sigma_{12}(r,0) < 0$ near $r \to 0$. More discussion on what the value of $\bar{n}$ means for the solution and stress fields are found in the later chapters

of this manuscript.

Using these results, stress fields and invariants can be found by taking the derivatives of Eqns. (4.28). Recalling the definition for $w(\theta)$ in Eqn. (4.29), then

$$\frac{\partial x_1}{\partial r} = b\bar{n}w(\theta)r^{\bar{n}-1} + \mathcal{O}\left(r^{\bar{n}-1}\right), \quad \frac{1}{r}\frac{\partial x_1}{\partial \theta} = bw'(\theta)r^{\bar{n}-1} + \mathcal{O}\left(r^{\bar{n}-1}\right),$$
$$\frac{\partial x_2}{\partial r} = \tfrac{1}{2}ar^{-1/2}\sin(\theta/2) + \mathcal{O}\left(r^{n-1}\right),$$
$$\text{and} \quad \frac{1}{r}\frac{\partial x_2}{\partial \theta} = \tfrac{1}{2}ar^{-1/2}\cos(\theta/2) + \mathcal{O}\left(r^{n-1}\right).$$

Using the definition in Eqn. (4.9), the function χ becomes

$$\begin{aligned}\chi(\theta) &= \tfrac{1}{2}ab\left[\bar{n}w(\theta)\cos(\theta/2) - w'(\theta)\sin(\theta/2)\right] \\ &= \tfrac{1}{2}ab\bar{n}\left[[\xi\sin(\bar{n}\theta) + \cos(\bar{n}\theta)]\cos(\theta/2) - [\xi\cos(\bar{n}\theta) - \cos(\bar{n}\theta)]\sin(\theta/2)\right],\end{aligned}$$

and utilizing the two known identities [90]

$$\sin\theta_1\sin\theta_2 + \cos\theta_1\cos\theta_2 = \cos(\theta_2 - \theta_1), \tag{4.31a}$$
$$\text{and} \quad \cos\theta_1\sin\theta_2 - \sin\theta_1\cos\theta_2 = \sin(\theta_2 - \theta_1), \tag{4.31b}$$

then

$$\begin{aligned}\chi(\theta) &= \tfrac{1}{2}ab\bar{n}\left[\tan(\bar{n}\pi)\sin[(\bar{n}-1/2)\theta] + \cos[(\bar{n}-1/2)\theta]\right] \\ &= \tfrac{1}{2}ab\bar{n}\left[\sin(\bar{n}\pi)\sin[(\bar{n}-1/2)\theta] + \cos(\bar{n}\pi)\cos[(\bar{n}-1/2)\theta]\right]\sec(\bar{n}\pi).\end{aligned}$$

Therefore utilizing Eqn. (4.31) once more,

$$\chi(\theta) = \tfrac{1}{2}ab\bar{n}\sec(\bar{n}\pi)\cos\left[(\bar{n}-1/2)\theta - \bar{n}\pi\right]. \tag{4.32}$$

The invariants can now be computed, where

$$\begin{aligned} I &= \left[b\bar{n}w(\theta)r^{\bar{n}-1} + \mathfrak{o}\left(r^{\bar{n}-1}\right)\right]^2 + \left[bw'(\theta)r^{\bar{n}-1} + \mathfrak{o}\left(r^{\bar{n}-1}\right)\right]^2 \\ &\qquad + \left[\tfrac{1}{2}ar^{-1/2}\sin(\theta/2) + \mathfrak{o}\left(r^{\bar{n}-1}\right)\right]^2 + \left[\tfrac{1}{2}ar^{-1/2}\cos(\theta/2) + \mathfrak{o}\left(r^{\bar{n}-1}\right)\right]^2 \\ &= \tfrac{1}{4}a^2r^{-1} + \mathfrak{o}\left(r^{\bar{n}-3/2}\right) + \mathcal{O}\left(r^{2(\bar{n}-1)}\right), \end{aligned}$$

and because $\bar{n} > 1/2$ then $2\bar{n} - \bar{n} > 2 - 3/2$, or $2\bar{n} - 2 > \bar{n} - 3/2$ making the $\mathcal{O}\left(r^{2(\bar{n}-1)}\right)$ term drop off as $r \to 0$. Finally, using Eqn. (4.32) the invariants are

$$I(r,\theta) = \tfrac{1}{4}a^2r^{-1} + \mathfrak{o}\left(r^{\bar{n}-3/2}\right), \tag{4.33a}$$

$$\text{and} \quad J(r,\theta) = \tfrac{1}{2}ab\bar{n}\sec(\bar{n}\pi)\cos\left[(\bar{n}-1/2)\theta - \bar{n}\pi\right]r^{\bar{n}-3/2} + \mathfrak{o}\left(r^{\bar{n}-3/2}\right). \tag{4.33b}$$

Note that Eqn. (4.33b) shows $J > 0$ as required for all $\xi > 0$, $0 \le \theta \le \pi$ and $r \ge 0$. Using Eqns. (4.22a) and (4.22b), the strain energy density from Eqn. (3.23) becomes

$$\mathcal{W} = \tfrac{1}{2}\mu\left(\tfrac{1}{4}a^2r^{-1} + \mathfrak{o}\left(r^{\bar{n}-3/2}\right) - 2 + \frac{1}{\beta}\left[\mathcal{O}\left(r^{\beta(3-2\bar{n})}\right) - 1\right]\right),$$

so that

$$\mathcal{W}(r,\theta) = \tfrac{1}{8}\mu a^2r^{-1} + \mathfrak{o}\left(r^{\bar{n}-3/2}\right). \tag{4.33c}$$

Also, with the help of Eqns. (4.31) the in-plane components of the deformation gradient from Eqn. (3.5) are

$$\begin{aligned} \mathcal{F}_{11} &= \cos\theta\left(b\bar{n}w(\theta)r^{\bar{n}-1}\right) - \sin\theta\left(bw'(\theta)r^{\bar{n}-1}\right) + \mathfrak{o}\left(r^{\bar{n}-1}\right) \\ &= \bar{n}br^{\bar{n}-1}\left[\cos\theta\left(\xi\sin(\bar{n}\theta) + \cos(\bar{n}\theta)\right)\right. \\ &\qquad \left. - \sin\theta\left(\xi\cos(\bar{n}\theta) - \sin(\bar{n}\theta)\right)\right] + \mathfrak{o}\left(r^{\bar{n}-1}\right) \end{aligned}$$

$$
\begin{aligned}
&= \bar{n}br^{\bar{n}-1}\left[\xi\left(\cos\theta\sin(\bar{n}\theta)-\sin\theta\cos(\bar{n}\theta)\right)\right.\\
&\qquad\left.+\left(\cos\theta\cos(\bar{n}\theta)+\sin\theta\sin(\bar{n}\theta)\right)\right]+\mathcal{O}\left(r^{\bar{n}-1}\right)\\
&= \bar{n}br^{\bar{n}-1}\left[\frac{\sin(\bar{n}\pi)\sin((\bar{n}-1)\theta)+\cos(\bar{n}\pi)\cos((\bar{n}-1)\theta)}{\cos(\bar{n}\pi)}\right]+\mathcal{O}\left(r^{\bar{n}-1}\right).
\end{aligned}
$$

Similarly,

$$
\begin{aligned}
\mathcal{F}_{12} &= \sin\theta\left(b\bar{n}w(\theta)r^{\bar{n}-1}\right)+\cos\theta\left(bw'(\theta)r^{\bar{n}-1}\right)+\mathcal{O}\left(r^{\bar{n}-1}\right)\\
&= \bar{n}br^{\bar{n}-1}\left[\sin\theta\left(\xi\sin(\bar{n}\theta)+\cos(\bar{n}\theta)\right)\right.\\
&\qquad\left.+\cos\theta\left(\xi\cos(\bar{n}\theta)-\sin(\bar{n}\theta)\right)\right]+\mathcal{O}\left(r^{\bar{n}-1}\right),\\
&= \bar{n}br^{\bar{n}-1}\left[\xi\left(\sin\theta\sin(\bar{n}\theta)+\cos\theta\cos(\bar{n}\theta)\right)\right.\\
&\qquad\left.+\left(\sin\theta\cos(\bar{n}\theta)-\cos\theta\sin(\bar{n}\theta)\right)\right]+\mathcal{O}\left(r^{\bar{n}-1}\right),\\
&= \bar{n}br^{\bar{n}-1}\left[\frac{\sin(\bar{n}\pi)\cos((\bar{n}-1)\theta)-\cos(\bar{n}\pi)\sin((\bar{n}-1)\theta)}{\cos(\bar{n}\pi)}\right].
\end{aligned}
$$

The remaining two components of the deformation gradient have the same form of the no-slip and frictionless cases, where

$$
\begin{aligned}
\mathcal{F}_{21} &= \cos\theta\left(\tfrac{1}{2}ar^{-1/2}\sin(\theta/2)\right)-\sin\theta\left(\tfrac{1}{2}ar^{-1/2}\cos(\theta/2)\right)+\mathcal{O}\left(r^{\bar{n}-1}\right),\\
\mathcal{F}_{22} &= \sin\theta\left(\tfrac{1}{2}ar^{-1/2}\sin(\theta/2)\right)+\cos\theta\left(\tfrac{1}{2}ar^{-1/2}\cos(\theta/2)\right)+\mathcal{O}\left(r^{\bar{n}-1}\right).
\end{aligned}
$$

Hence, the deformation gradient components are

$$\mathcal{F}_{11}(r,\theta) = \bar{n}br^{\bar{n}-1}\sec(\bar{n}\pi)\cos[\bar{n}\pi-(\bar{n}-1)\theta]+\mathcal{O}\left(r^{\bar{n}-1}\right), \tag{4.34a}$$

$$\mathcal{F}_{12}(r,\theta) = \bar{n}br^{\bar{n}-1}\sec(\bar{n}\pi)\sin[\bar{n}\pi-(\bar{n}-1)\theta]+\mathcal{O}\left(r^{\bar{n}-1}\right), \tag{4.34b}$$

$$\mathcal{F}_{21}(r,\theta) = -\tfrac{1}{2}ar^{-1/2}\sin(\theta/2)+\mathcal{O}\left(r^{\bar{n}-1}\right), \tag{4.34c}$$

and $$\mathcal{F}_{22}(r,\theta) = \tfrac{1}{2}ar^{-1/2}\cos(\theta/2)+\mathcal{O}\left(r^{\bar{n}-1}\right). \tag{4.34d}$$

Finally, the Cauchy stress components can be determined. Recall Eqns. (3.26)

$$\begin{aligned}
\sigma_{11} &= \mu\big[\chi(\theta)r^{\bar{n}-3/2}\big]^{-1}\big[\bar{n}^2b^2r^{2(\bar{n}-1)}\sec^2(\bar{n}\pi)+\mathfrak{o}\big(r^{2(\bar{n}-1)}\big)+\mathcal{O}\big(r^{\beta(3-2\bar{n})}\big)\big],\\
\sigma_{12} &= \mu\big[\chi(\theta)r^{\bar{n}-3/2}\big]^{-1}\Bigg[\bigg(\bar{n}br^{\bar{n}-1}\frac{\cos[\bar{n}\pi-(\bar{n}-1)\theta]}{\cos(\bar{n}\pi)}\bigg)\big(-\tfrac{1}{2}ar^{-1/2}\sin(\theta/2)\big)\\
&\qquad+\bigg(\bar{n}br^{\bar{n}-1}\frac{\sin[\bar{n}\pi-(\bar{n}-1)\theta]}{\cos(\bar{n}\pi)}\bigg)\big(\tfrac{1}{2}ar^{-1/2}\cos(\theta/2)\big)+\mathfrak{o}\big(r^{\bar{n}-3/2}\big)\Bigg],\\
&= \mu\Big(\cancel{\frac{ab\bar{n}}{2}}\Big)\Bigg[\Big(\cancel{\frac{2}{ab\bar{n}}}\Big)\frac{\cancel{\cos(\bar{n}\pi)}}{\cos[\bar{n}\pi-(\bar{n}-1/2)\theta]}\Bigg]\Bigg[\frac{\sin[\bar{n}\pi-(\bar{n}-1/2)\theta]}{\cancel{\cos(\bar{n}\pi)}}\Bigg]+\mathfrak{o}(1),\\
\sigma_{22} &= \mu\big[\chi(\theta)r^{\bar{n}-3/2}\big]^{-1}\big[\tfrac{1}{4}a^2r^{-1}+\mathfrak{o}\big(r^{2(\bar{n}-1)}\big)+\mathcal{O}\big(r^{\beta(3-2\bar{n})}\big)\big],
\end{aligned}$$

which, after recalling the definition for $\bar{n}$ from Eqn. (4.27) and noting another identity

$$\sec(\bar{n}\pi)=\sec\big(\pi+\tan^{-1}\xi\big)=-\sqrt{1+\xi^2}, \tag{4.35}$$

then

$$\sigma_{11}(r,\theta)=\mu\left(\frac{\bar{n}^2b^2}{\chi(\theta)}\right)\big(1+\xi^2\big)r^{\bar{n}-1/2}+\mathfrak{o}\big(r^{\bar{n}-1/2}\big), \tag{4.36a}$$

$$\sigma_{12}(r,\theta)=\sigma_{21}(r,\theta)=\mu\tan[\bar{n}\pi-(\bar{n}-1/2)\theta]+\mathfrak{o}(1), \tag{4.36b}$$

$$\sigma_{22}(r,\theta)=\mu\left(\frac{a^2}{4\chi(\theta)}\right)r^{1/2-\bar{n}}+\mathfrak{o}\big(r^{1/2-\bar{n}}\big). \tag{4.36c}$$

This concludes the solution of the finite friction case. The near field results are summarized in Table 4.3. As a final check, note that the stresses given by Eqns. (4.36) collapse to the frictionless case (when $\xi=0$ or $\bar{n}=1$) as shown by Eqns. (4.17). Given this, we can conclude that the frictionless case is simply a special case of finite friction when the slip threshold is set to $\xi=0$ (or $\tau=0$).

Table 4.3: Summary of the asymptotic solution near $r \to 0$ for the finite friction case.

Field Type	**Near Field Approximation Equations Near** $r = 0$
Deformation:	Eqns. (4.28a), $x_1 \simeq \bar{x}_1 + b r^{\bar{n}} [\xi \sin(\bar{n}\theta) + \cos(\bar{n}\theta)]$
	(4.28b): $x_2 \simeq a_2 r^{1/2} \sin(\theta/2)$
Stress:	Eqns. (4.36a), $\sigma_{11} \simeq \mu \left(\dfrac{\bar{n}^2 b^2}{\chi(\theta)} \right) \left(1 + \xi^2\right) r^{\bar{n}-1/2}$
	(4.36b), $\sigma_{12} = \sigma_{21} \simeq \mu \tan[\bar{n}\pi - (\bar{n} - 1/2)\theta]$
	(4.36c): $\sigma_{22} \simeq \mu \left(\dfrac{a^2}{4\chi(\theta)} \right) r^{1/2-\bar{n}}$
Scalar Functions:	Eqns. (4.33a), $I \simeq \frac{1}{4} a^2 r^{-1}$
	(4.33b), $J \simeq \chi(\theta) r^{\bar{n}-3/2}$
	(4.33c): $\mathcal{W} \simeq \frac{1}{8} \mu a^2 r^{-1}$
Other Definitions:	Eqns. (4.32), $\chi(\theta) \equiv \frac{1}{2} a b \bar{n} \sec(\bar{n}\pi) \cos[(\bar{n} - 1/2)\theta - \bar{n}\pi]$
	(4.27), $\bar{n}(\xi) \equiv 1 + \dfrac{1}{\pi} \tan^{-1} \xi$

5 - Evaluation of Near-Field Solutions

5.1 A Comparison of the Extents of Friction

From the results for the frictionless (Table 4.1) and no-slip (Table 4.2) cases, we see there is no direct dependence on the compressibility parameter β, however dependence may be reside in higher terms. Another possibility is that dependence on β resides in the constants a, b, a_1, and a_2 from Eqns. (4.14) and (4.21), which are investigated further in Chapters 7 and 8. For the two limiting cases shown, the shape of the crack front on the free edge is found by combining the deflected coordinate solutions. Starting with the frictionless case, use Eqns. (4.14a) and (4.14b) with $\theta = \pi$ so that

$$x_1(r,\pi) \simeq \bar{x}_1 - br, \qquad \text{and} \qquad x_2(r,\pi) \simeq ar^{1/2},$$

which combined show a parabolic curve on deflected the free edge

$$x_1 \simeq \bar{x}_1 - \left(\frac{b}{a^2}\right) x_2^2. \tag{5.1}$$

Similarly, on the traction free edge, the deflected shape for the no-slip case from Eqns. (4.21a) and (4.21b) also has a quadratic shape,

$$x_1(r,\pi) \simeq a_1 r^{1/2} - r, \qquad \text{and} \qquad x_2(r,\pi) \simeq a_2 r^{1/2},$$

where combining yields

$$x_1 \simeq \left(\frac{a_1}{a_2}\right) x_2 - \left(\frac{1}{a_2^2}\right) x_2^2. \tag{5.2}$$

The first notable difference is that at the crack tip, the no-slip case shows a finite slope ($\phi \neq \pi/2$) on the traction free edge after loading and the frictionless case yields a vertical slope. The finite slope at the crack tip in the no-slip case is the wedge angle ϕ (as shown in Figure 1.1b) and is quantified by the limit

$$\tan\phi \equiv \lim_{\substack{r\to 0 \\ \theta\to\pi}} \frac{dx_2}{dx_1}. \tag{5.3}$$

This slope can be worked out by taking the implicit derivative of Eqn. (5.2), or

$$1 \simeq \left(\frac{a_1}{a_2}\right)\frac{dx_2}{dx_1} - \left(\frac{2}{a_2^2}\right) x_2 \frac{dx_2}{dx_1}.$$

Re-arranging, and solving for dx_2/dx_1 yields

$$\frac{dx_2}{dx_1} \simeq \frac{a_2^2}{a_1 a_2 - 2x_2} = \frac{a_2}{a_1 - 2r^{1/2}}.$$

Taking the limit, the wedge angle defined in Eqn. (5.3) becomes

$$\tan\phi \simeq \frac{a_2}{a_1} \quad \text{as} \quad r \to 0. \tag{5.4}$$

Noting the coefficient with the x_2^2 term from Eqn. (5.2) being $-1/a_2^2 < 0$ indicates that the opening shape is to the left, however depending on the sign of a_1 (it is expected that $a_2 \geq 0$ given Eqn. (4.28b) and requiring $x_2 \geq 0$), it would be expected that the vertex of the opening

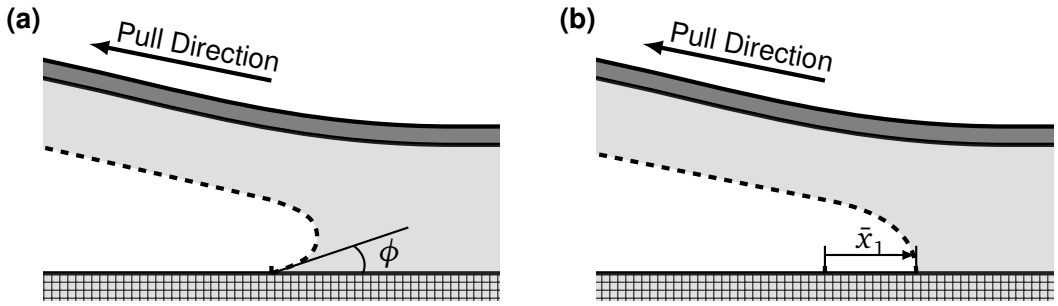

Figure 5.1: Visualization of the Extents of Friction for a Loaded Interface Crack. (a) Loaded Interface Crack with No-Slip Bonding (b) Loaded Interface Crack with Frictionless Bonding.

shape may reside above or below the $\hat{\mathbf{e}}_1$ axis, depending on the sign of the constant a_1. While in the absence of friction, the shape of Eqn. (5.1) suggests that the wedge angle $\phi \to \pi/2$ and the crack displacement $\bar{x}_1$ on the bonded edge is the vertex of the parabolic shape. This makes sense given that it is expected that the frictionless solution is the top half of the full crack problem, hence symmetric with the horizontal $\hat{\mathbf{e}}_1$ axis.

Given the visualization shown in Figure 5.1a, there is a physical limitation that $0 \leq \phi \leq \pi$ because the elastomer would penetrate the substrate. Using Eqn. (5.4), it is expected the constant $a_1 = 0$ when $\phi = \pi/2$ (the vertical wedge angle) and a_1 is positive or negative if the wedge angle ranges are $0 \leq \phi < \pi/2$ and $\pi/2 < \phi \leq \pi$ respectively. At this transition point (when $a_1 = 0$), we see from Eqn. (5.2) a similarly shaped function to the frictionless case (eqn (5.1)) with no crack tip movement. To model the effect of this transition on the stresses, let $a_1 = 0$ in Eqns. (4.24) where

$$\sigma_{11} \simeq 0, \quad \sigma_{12} \simeq -\mu \tan(\theta/2), \quad \text{and} \quad \sigma_{22} \simeq \tfrac{1}{2}\mu a_2 r^{-1/2} \sec(\theta/2). \tag{5.5}$$

Here, the σ_{11} term loses the singularity as $r \to 0$ and the stress state has a similar form as the frictionless stresses from Eqns. (4.17), although not enough terms are left to confirm if $\sigma_{11} \to \mathcal{O}\left(r^{1/2}\right)$ as $a_1 \to 0$ in the no-slip case. This transition is of interest and could be a

link between the two extents of interfacial friction. This transition point is investigated further in Section 7.2 of this manuscript.

In the frictionless case, the most dominant stress as $r \to 0$ is the normal stress σ_{22} and hence it is expected that failure should occur by delamination in the x_2 direction. Much has been published on the general crack problem [85, 48, 79, 80, 50] (which is a full plane problem of the frictionless case) and cohesive tearing models can be used. The no-slip case has the same order of singularity as $r \to 0$ for all three in plane stress components and it is then expected that in this case failure can happen in either x_1 or x_2 direction. The stresses along the bonded edge where delamination is expected can be found by making $\theta = 0$ in Eqns. (4.17) and (4.24) and both cases are summarized below.

No-Slip Stresses		**Frictionless Stresses**
$\sigma_{11} \simeq \mu\left(\frac{a_1^2}{2a_2}\right) r^{-1/2},$		$\sigma_{11} \simeq \mu\left(\frac{2b}{a}\right) r^{1/2},$
$\sigma_{12} \simeq \mu\left(\frac{a_1}{2}\right) r^{-1/2},$	and	$\sigma_{12} \simeq 0,$ and
$\sigma_{22} \simeq \mu\left(\frac{a_2}{2}\right) r^{-1/2}.$		$\sigma_{22} \simeq \mu\left(\frac{a}{2b}\right) r^{-1/2}.$

As expected, the frictionless condition $\mathcal{P}_{12}(r,0) = 0$ implies $\sigma_{12}(r,0) = 0$. Also worth noting here is the product of the stresses on the bonded edge from Eqns. (4.17a) and (4.17c) yields a positive, finite, and constant value expressed as a tidy closed form relation

$$\sigma_{11}\sigma_{22} \simeq \mu^2 \quad \text{and} \quad \sigma_{12} \simeq 0, \qquad \text{on} \quad \theta = 0. \tag{5.6}$$

While all stress terms on the bonded edge in the no-slip case are singular as $r \to 0$, since they have the same asymptotic order, a tearing mechanism can be expressed as stress ratios. Using this idea with the finding from Eqn. (5.4), we see a direct relationship between the stresses, the constants a_1 and a_2, and wedge angle ϕ where

$$\frac{\sigma_{22}}{\sigma_{11}} \simeq \left(\frac{a_2}{a_1}\right)^2 = \tan^2\phi \quad \text{and} \quad \frac{\sigma_{12}}{\sigma_{11}} \simeq \frac{a_2}{a_1} = \tan\phi, \qquad \text{on} \quad \theta = 0. \tag{5.7}$$

For low wedge angles $\phi < \pi/4$, then $\tan\phi < 1$ and σ_{11} dominates over the other two stress components. If the wedge angle increases above $\phi > \pi/4$, then the opposite is true and σ_{22} dominates both σ_{12} and σ_{11}.

Fracture can also occur near the crack tip inside the bulk material away from the bonded edge ($\theta \neq 0$) and even along the traction free edge [20]. Unfortunately, due to the degeneracy of the expressions for J in both cases (Eqns. (4.22b) and (4.16b)) the stress field expressions near the free edge $\theta \simeq \pi$ are not valid. However, assuming the Blatz-Ko material from Eqn. (3.23), then the method used by Knowles and Sternberg can be utilized to approximate the stresses on the free edge [79, 1]. Note that

$$\det\left[\mathcal{F}^T\mathcal{P}\right] = \det\left[\mu\mathcal{F}^T\mathcal{F} - \mu J^{-2\beta}\mathbf{I}\right] = \mu^3 \det\left[\mathcal{C} - J^{-2\beta}\mathbf{I}\right]. \tag{5.8}$$

The right hand term can be put into characteristic polynomial form, which for any second order tensor is [40]

$$\det(\mathbf{A} - x\mathbf{I}) = -x^3 + I_1^A x^2 - I_2^A x + I_3^A, \tag{5.9}$$

where I_i^A $(i = 1,2,3)$ and are the principal invariants of the tensor $\mathbf{A}$. So, for the referential displacement tensor $\mathcal{C}$, then using Eqns. (2.29) we have the equivalent polynomial form

$$\begin{aligned}\det\left[\mathcal{C} - \left(J^{-2\beta}\right)\mathbf{I}\right] &= -\left(J^{-2\beta}\right)^3 + (I+1)\left(J^{-2\beta}\right)^2 - (I+J^2)\left(J^{-2\beta}\right) + J^2 \\ &= J^{-2\beta}\left(1 - J^{-2\beta}\right)\left[J^{-2\beta} + J^{2\beta+2} - I\right].\end{aligned}$$

Another form of Eqn. (5.8) is

$$\det\left[\mathcal{F}^T\mathcal{P}\right] = \det\mathcal{F}\det\mathcal{P} = J\det\mathcal{P}.$$

Since we imposed $\mathcal{P}_{12}= \mathcal{P}_{22}= 0$ on the traction free edge ($\theta = \pi$) and $\mathcal{P}_{32}= 0$ in plane strain, then as $\theta \to \pi$ the determinant of the first Piola tensor on the free edge $\det\mathcal{P} = 0$ and

$$0 = J^{-2\beta}\left(1-J^{-2\beta}\right)\left[J^{-2\beta}+J^{2\beta+2}-I\right].$$

Since this material is assumed compressible, then $J \neq 1$ identically and it must be assumed that for any finite J then $J^{-2\beta} \neq 0$ requiring

$$I = J^{-2\beta}+J^{2(\beta+1)}. \tag{5.10}$$

Recall that $J > 0$ and assuming $J = \mathcal{O}\left(r^{\bar{\alpha}}\right)$ as $r \to 0$, then $\bar{\alpha} < 0$ so it is assumed that the $J^{2\beta+2}$ term is most dominant. From both Eqns. (4.16a) and (4.22a) it was found that $I = \mathcal{O}\left(r^{-1}\right)$, therefore we can conclude for any case near $r \to 0$ that

$$J(r,\pi) \simeq [I(r,\pi)]^{\frac{1}{2\beta+2}} = \mathcal{O}\left(r^{-\frac{1}{2\beta+2}}\right). \tag{5.11}$$

The implication of the expression in Eqn. (5.11) is that there is a small boundary layer near $\theta \to \pi$ which has an asymptotic field of $\mathcal{O}\left(r^{-1/(2\beta+2)}\right)$ as $r \to 0$. Using the expression in Eqn. (5.11), then J can be worked out for both cases on $\theta = \pi$. Using Eqns. (4.16a), (4.16b), (4.22a), and (4.22b), J for the no-slip and frictionless cases have the asymptotic relations near the free edge $\theta = \pi$:

No-Slip Case: $$J(r,\pi) \simeq \left(\frac{a_1^2+a_2^2}{4r}\right)^{\frac{1}{2\beta+2}}, \tag{5.12}$$

Frictionless Case: $$J(r,\pi) \simeq \left(\frac{a^2}{4r}\right)^{\frac{1}{2\beta+2}}. \tag{5.13}$$

Using this result, the in-plane stress components on the free edge for the frictionless case are

$$\sigma_{11}(r,\pi) = \mu\left[\frac{4r}{a^2}\right]^{\frac{1}{2\beta+2}}\left[b^2 + \mathfrak{o}(1) + \mathcal{O}\left(r^{\beta}\right)\right],$$
$$\sigma_{12}(r,\pi) = \sigma_{21} = \mu\left[\frac{4r}{a^2}\right]^{\frac{1}{2\beta+2}}\left[-b\left(\frac{a}{2\sqrt{r}}\right) + \mathfrak{o}\left(r^{-1/2}\right)\right],$$
and $$\sigma_{22}(r,\pi) = \mu\left[\frac{4r}{a^2}\right]^{\frac{1}{2\beta+2}}\left[\frac{a^2}{4r} + \mathfrak{o}(1) - \left[\frac{4r}{a^2}\right]^{\frac{\beta}{\beta+1}}\right].$$

Therefore, for any $\beta > 0$ the stress field on the traction free edge has the form as $r \to 0$:

$$\sigma_{11}(r,\pi) = \mu b^2\left(\frac{4r}{a^2}\right)^{\frac{1}{2\beta+2}} + \mathfrak{o}\left(r^{\frac{1}{2\beta+2}}\right), \tag{5.14a}$$
$$\sigma_{12}(r,\pi) = -\mu b\left(\frac{a^2}{4r}\right)^{\frac{\beta}{2\beta+2}} + \mathfrak{o}\left(r^{-\frac{\beta}{2\beta+2}}\right), \tag{5.14b}$$
and $$\sigma_{22}(r,\pi) = \mu\left(\frac{a^2}{4r}\right)^{\frac{2\beta+1}{2\beta+2}} + \mathfrak{o}\left(r^{-\frac{2\beta+1}{2\beta+2}}\right). \tag{5.14c}$$

This result indicates that the normal stress σ_{22} singularity remains on the free edge, and while we found zero lateral traction ($\sigma_{12} = 0$) on the bonded edge, there is now a shear singularity which would indicate a potential scissoring mode of fracture. Also, the nature of singularity for the normal stress σ_{22} as $r \to 0$ is increased and depends on the material compressibility parameter β. However, this result indicates that incompressible materials (as $\beta \to \infty$) will have singularities in both σ_{12} and σ_{22}. While the asymptotic order of the stress terms are not in a form that we can simply show a ratio or product, using some creative algebra a potentially useful tearing mechanism for the frictionless case on the free edge is

$$\frac{\sigma_{12}^2\sigma_{22}}{\sigma_{11}} \simeq \mu^2, \qquad \text{on} \quad \theta = \pi. \tag{5.15}$$

Using the same method as the frictionless case with the finding in Eqn. (5.12), the stresses for the no-slip case on the free edge are

$$\sigma_{11}(r,\pi) = \mu\left[\frac{4r}{a_1^2+a_2^2}\right]^{\frac{1}{2\beta+2}}\left[\frac{a_1^2}{4r} - \frac{a_1}{\sqrt{r}} + o\left(r^{-1/2}\right) + \mathcal{O}\left(r^{\beta}\right)\right],$$

$$\sigma_{12}(r,\pi) = \mu\left[\frac{4r}{a_1^2+a_2^2}\right]^{\frac{1}{2\beta+2}}\left[\frac{a_1 a_2}{4r} - \frac{a_2}{2\sqrt{r}} + o\left(r^{-1/2}\right)\right], \quad \text{and}$$

$$\sigma_{22}(r,\pi) = \mu\left[\frac{4r}{a_1^2+a_2^2}\right]^{\frac{1}{2\beta+2}}\left[\frac{a_2^2}{4r} + o\left(r^{-1/2}\right) + \mathcal{O}\left(r^{\beta}\right)\right].$$

Defining the constant $\bar{a} \equiv \sqrt{a_1^2+a_2^2}$ (for brevity), then the Cauchy stress components on the free edge for the no-slip case have the final form

$$\sigma_{11}(r,\pi) = \mu\frac{a_1}{\bar{a}}\left(\frac{a_1}{\bar{a}}\left[\frac{\bar{a}^2}{4r}\right]^{\frac{2\beta+1}{2\beta+2}} - 2\left[\frac{\bar{a}^2}{4r}\right]^{\frac{\beta}{\beta+1}}\right) + o\left(r^{-\frac{\beta}{\beta+1}}\right), \tag{5.16a}$$

$$\sigma_{12}(r,\pi) = \mu\frac{a_2}{\bar{a}}\left(\frac{a_1}{\bar{a}}\left[\frac{\bar{a}^2}{4r}\right]^{\frac{2\beta+1}{2\beta+2}} - \left[\frac{\bar{a}^2}{4r}\right]^{\frac{\beta}{\beta+1}}\right) + o\left(r^{-\frac{\beta}{\beta+1}}\right), \tag{5.16b}$$

$$\text{and} \quad \sigma_{22}(r,\pi) = \mu\left(\frac{\bar{a}^2}{4r}\right)^{\frac{2\beta+1}{2\beta+2}} + o\left(r^{-\frac{\beta}{\beta+1}}\right). \tag{5.16c}$$

This is an interesting result given that again the singularities as $r \to 0$ all have the same order like on the bonded edge and these singularities become more severe as the material becomes more incompressible ($\beta \to \infty$). While all stress terms on the bonded edge in the no-slip case are singular as $r \to 0$, since they have the same asymptotic order, a tearing mechanism can be expressed as stress ratios of the most dominant asymptotic terms. Again, utilizing Eqn. (5.4), then a relationship between the stresses and wedge angle ϕ for the no-slip case on the free edge is

$$\frac{\sigma_{22}}{\sigma_{11}} \simeq 1 + \frac{a_2^2}{a_1^2} = \sec^2\phi \quad \text{and} \quad \frac{\sigma_{12}}{\sigma_{11}} \simeq \frac{a_2}{a_1} = \tan\phi, \qquad \text{on} \quad \theta = \pi. \tag{5.17}$$

This result shows finite stress ratios unless the wedge angle is $\phi = \pi/2$, or when $a_1 = 0$. In this case, making $a_1 = 0$ in Eqns. (5.16) reveals a reduced singularity as $r \to 0$ on the free edge in both σ_{11} and σ_{12} so that

$$\sigma_{11} = \mathcal{O}\Big(r^{-\frac{\beta}{\beta+1}}\Big), \quad \sigma_{12} \simeq -\frac{\mu}{a_2}\left[\frac{a_2^2}{4r}\right]^{\frac{\beta}{\beta+1}}, \quad \text{and} \quad \sigma_{22} \simeq \mu\left[\frac{a_2^2}{4r}\right]^{\frac{2\beta+1}{2\beta+2}}.$$

As a final comparison between the two limiting cases of friction, the $\mathcal{J}$-integral (a path independent contour integral which is related to the stress intensity factors used in LEFM [99]) is equivalent to the energy release rate [99, 22, 20] (the ratio of the energy dissipated in fracture opening and the crack surface area). For finite strain elastostatics, this has the form [85, 79]

$$\mathcal{J} = \int_\Gamma \left[\mathcal{W}N_1 - \mathcal{P}_{iA}N_A\frac{\partial u_i}{\partial X_1}\right]d\Gamma. \tag{5.18}$$

Since this integral is path independent, choose the path as a 'small' circle around the origin of radius R so that $N_A = \tilde{\mathbb{C}}_A(\theta)$ $(A = 1, 2)$ and then take the limit as $R \to 0$. Using the plane strain $(i = 1, 2)$ Eqns. (2.1) and (3.4) this integral becomes

$$\mathcal{J} = \lim_{R\to 0}\int_0^\pi \left[\mathcal{W}(R,\theta)\tilde{\mathbb{C}}_1(\theta) - \mathcal{P}_{iA}(R,\theta)\tilde{\mathbb{C}}_A(\theta)\left(\frac{\partial u_i}{\partial r}\tilde{\mathbb{C}}_1(\theta) - \frac{1}{r}\frac{\partial u_i}{\partial \theta}\tilde{\mathbb{C}}_2(\theta)\right)\right](Rd\theta).$$

The integral is with respect to the angular coordinate θ, so the limit can be brought inside the integral. After taking the limit and using Eqns. (3.24) and (4.22a), then the $\mathcal{J}$-Integral for the no-slip case becomes

$$\mathcal{J} = \frac{\mu}{8}\int_0^\pi \left[\bar{a}^2\cos\theta - 2\bar{a}^2\sin^2\left(\frac{\theta}{2}\right)\cos\theta + 2\bar{a}^2\cos\left(\frac{\theta}{2}\right)\sin\left(\frac{\theta}{2}\right)\sin\theta\right]d\theta.$$

The three integrands are worked out to be

$$\int_0^\pi \cos\theta\, d\theta = 0,$$
$$\int_0^\pi \sin^2\left(\frac{\theta}{2}\right)\cos\theta\, d\theta = -\frac{\pi}{4},$$

and $\int_0^{\pi} \sin\left(\frac{\theta}{2}\right)\cos\left(\frac{\theta}{2}\right)\cos\theta\, d\theta = \frac{\pi}{4}.$

The procedure for the frictionless case is identical, and we find the path independent opening release rate for the no-slip and frictionless cases to be

No-Slip Case: $\mathcal{J} = \frac{1}{8}\mu\pi\left(a_1^2 + a_2^2\right),$ (5.19a)

Frictionless Case: $\mathcal{J} = \frac{1}{8}\mu\pi a^2.$ (5.19b)

Both $\mathcal{J}$-integral formulations have a similar form and the frictionless case in Eqn. (5.19a) is confirmed by Knowles and Sternberg [79] for the general crack problem, however their result is double the value because they used an angle range of $-\pi \leq \theta \leq \pi$ while the interface crack problem is only from $0 \leq \theta \leq \pi$. In comparison to the stresses found earlier, the frictionless case was dominated by normal stresses ($\sigma_{22} >> \sigma_{11}, \sigma_{12}$) while the no-slip case showed stresses of the same order in r as $r \to 0$ and has effects from both normal and lateral stresses. The expressions in Eqns. (5.19) shows that for the frictionless case, there is no opening energy from any lateral movement because the constant b is not represented in Eqn. (5.19b), however the no-slip case has opening energy that takes into account both lateral and normal movement.

5.2 Between the Extents of Friction

Similar to the no-slip and frictionless cases, the finite friction result (summarized in Table 4.3) shows no direct dependence on β. Dependence of β on the constants a and b are discussed in more detail in the numerical study from Chapter 8.

For the present case, the deformed shape of the free edge can be approximated using Eqns. (4.28) at $\theta = \pi$, where

$x_1(r,\pi) \simeq \bar{x}_1 + b\left[\xi\sin(\bar{n}\pi) + \cos(\bar{n}\pi)\right] r^{\bar{n}}, \quad \text{and} \quad x_2(r,\pi) \simeq a_1 r^{-1/2}.$

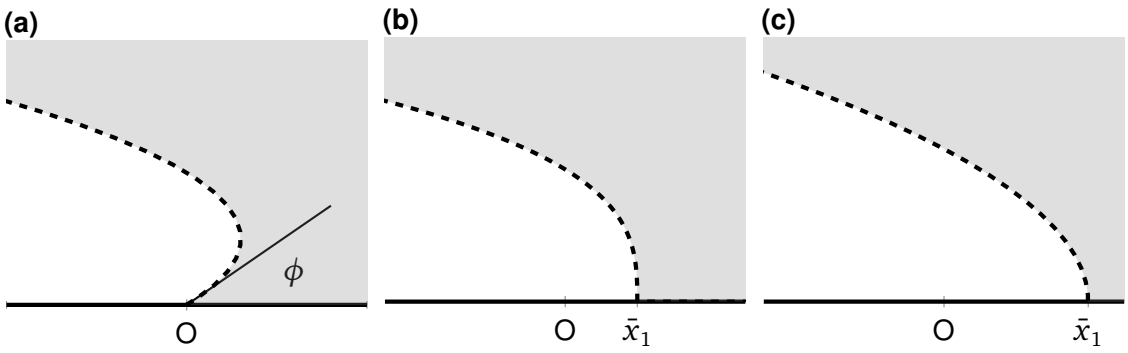

Figure 5.2: Visualization of the Three Loaded Interface Crack Deflection Shapes. (a) No-Slip Case (b) Finite Friction Case ($\xi \neq 0$) (c) Frictionless Case ($\xi = 0$)

Using two more trig identities

$$\sin(\pi + \tan^{-1}\xi) = -\frac{\xi}{\sqrt{1+\xi^2}}, \tag{5.20}$$

$$\text{and} \quad \cos(\pi + \tan^{-1}\xi) = -\frac{1}{\sqrt{1+\xi^2}}, \tag{5.21}$$

together with Eqn. (4.27), the free edge for the finite friction case has a deformed shape near $r \to 0$

$$x_1 \simeq \bar{x}_1 - \left(\frac{b\sqrt{1+\xi^2}}{a^{2\bar{n}}}\right) x_2^{2\bar{n}}. \tag{5.22}$$

Recall that the no-slip and frictionless solutions from Eqns. (5.1) and (5.2) respectively showed parabolic curves near the crack front. As Eqn. (5.22) shows, unless $\bar{n} = 1$ (when $\xi = 0$, the frictionless case) the free edge takes either a blunted ($\xi > 0$ so that $\bar{n} > 1$) or sharpened ($\xi < 0$, hence $\bar{n} < 1$) parabola. A visualization of this blunting effect is shown in Figure 5.2. Here, Figures 5.2a and 5.2c represent the no-slip and frictionless cases respectively (also shown in Figure 5.1) and Figure 5.2b represents an interface crack that is blunted ($\xi > 0$) from slippage under friction.

It was found in Section 4.3 that the finite friction case converges to the frictionless case

when $\xi \to 0$. This case also shows a vertical wedge angle ϕ like the frictionless case. Both of these findings imply a direct connection of the finite friction case and the frictionless case. Given the theoretical range of solution (Eqn. (4.30)) when $\xi > 0$ (the blunting case), a finite slip threshold is required which implies no direct connection to the no-slip case. However, under left induced slippage, $\xi < 0$ and the range from Eqn. (4.30) allows the case where the threshold $\xi \to -\infty$ so that $\bar{n} \to 1/2$. Unfortunately, one can not blindly plug in $\bar{n} = 1/2$ (and by extension $\xi \to \infty$) into any of the expressions in Table 4.3 because they show indeterminate limits.

Further insight into a potential connection between the no slip and finite friction cases can be gained by evaluating the stresses. Recall the tearing mechanism identified for the no-slip case in Eqn. (5.7) where a ratio of the stresses were given. Using Eqns. (4.36), the same ratios for the finite friction case yield

$$\begin{aligned}
\lim_{\bar{n}\to\frac{1}{2}} \frac{\sigma_{22}}{\sigma_{11}} &\simeq \lim_{\xi\to-\infty} \left(\frac{a^2}{4b^2\bar{n}^2(1+\xi^2)}\right) r^{1-2\bar{n}} \simeq \lim_{\bar{n}\to\frac{1}{2}} \left(\frac{a\cos(\bar{n}\pi)}{2b\bar{n}}\right)^2 r^{1-2\bar{n}} = 0, \\
\lim_{\bar{n}\to\frac{1}{2}} \frac{\sigma_{12}}{\sigma_{11}} &\simeq \lim_{\xi\to-\infty} \left(\frac{1}{b^2\bar{n}^2(1+\xi^2)}\right)\left(\frac{\sin(\bar{n}\pi-[\bar{n}-1/2]\theta)}{\cos(\bar{n}\pi)}\right) r^{1/2-\bar{n}} \\
&\simeq \lim_{\bar{n}\to\frac{1}{2}} \left(\frac{1}{b\bar{n}}\right)^2 \cos(\bar{n}\pi)\sin(\bar{n}\pi-[\bar{n}-1/2]\theta) r^{1/2-\bar{n}} = 0, \\
\text{and} \quad \lim_{\bar{n}\to\frac{1}{2}} \frac{\sigma_{22}}{\sigma_{12}} &\simeq \lim_{\bar{n}\to\frac{1}{2}} \left(\frac{a}{2b\bar{n}}\right)\left(\frac{\cos(\bar{n}\pi)}{\sin(\bar{n}\pi-[\bar{n}-1/2]\theta)}\right) r^{1/2-\bar{n}} = 0.
\end{aligned}$$

In the cases above, as $\xi \to -\infty$, each expression is of $\mathcal{O}(1)$ as $r \to 0$ and the stress relations must be $\sigma_{11} > \sigma_{12} > \sigma_{22}$. This result is primarily because both σ_{11} and σ_{12} are singular as $\bar{n} \to 1/2$, while a constant value for σ_{22} is found to be

$$\lim_{\bar{n}\to\frac{1}{2}} \sigma_{22} \simeq \lim_{\bar{n}\to\frac{1}{2}} \mu\left(\frac{a}{2b\bar{n}}\right)\left(\frac{\cos(\bar{n}\pi)}{\cos([\bar{n}-1/2]\theta-\bar{n}\pi)}\right) r^{1/2-\bar{n}} = \mu\left(\frac{a}{b}\right).$$

This result does not make sense given the comparison to the no-slip result. Further, Eqn. (4.24c) shows a singularity in r as $r \to 0$ and the fact that none of the ratios found above give

finite, non-zero values it is then concluded that the finite friction solution does not converge to the no-slip solution and the direct comparison is not viable.

However, another comparison can be found by considering the stresses on the bonded edge ($\theta = 0$). The stress field from Eqns. (4.24) (4.32), and (4.36) we find

$$\chi(0) = \tfrac{1}{2} a b \bar{n} \cancel{\sec(\bar{n}\theta)} \cancel{\cos(-\bar{n}\theta)} = \frac{a b \bar{n}}{2},$$

so that

No-Slip Stresses

$$\sigma_{11}(r,0) \simeq \mu \left(\frac{a_1^2}{2a_2} \right) r^{-1/2},$$
$$\sigma_{12}(r,0) \simeq \mu \left(\frac{a_1}{2} \right) r^{-1/2}, \quad \text{and}$$
$$\sigma_{22}(r,0) \simeq \mu \left(\frac{a_2}{2} \right) r^{-1/2}.$$

Finite Friction Stresses

$$\sigma_{11}(r,0) \simeq \mu \left(\frac{2b\bar{n}}{a} \right) \left(1 + \xi^2\right) r^{\bar{n}-1/2},$$
$$\sigma_{12}(r,0) \simeq \tau, \quad \text{and}$$
$$\sigma_{22}(r,0) \simeq \mu \left(\frac{a}{2b\bar{n}} \right) r^{1/2-\bar{n}}.$$

Similar to the frictionless case, the product of the normal stresses with finite friction yields a constant value and re-arranging we get

$$\sigma_{11}\sigma_{22} - \tau^2 = \mu^2 + \mathcal{O}(1).$$

Using this same evaluation for the no-slip case, note that

$$\sigma_{11}\sigma_{22} - \sigma_{12}^2 = \mathcal{O}\left(r^{-1/2}\right).$$

Recalling that $\sigma_{12}(r,0) = \tau$ in the finite friction case, a direct comparison of the stresses on the bonded edge applies:

$$\sigma_{11}\sigma_{22}-\sigma_{12}^2=\begin{cases}\mathfrak{o}\left(r^{-1/2}\right), & \text{No-Slip}\\ \mu^2+\mathfrak{o}(1), & \text{Finite Friction}\end{cases}\qquad \text{on}\quad \theta=0. \tag{5.23}$$

Like the two limiting cases, the stresses from Eqns. (4.36) become unbound as $\theta\to\pi$, again due to the degeneracy of J from Eqn. (4.33b). In Section 5.1, it was proven that on the free edge that J has a different form near $\theta=\pi$ in the form of Eqn. (5.11) and utilizing Eqn. (4.33a) we arrive at Eqn. (5.13). The stresses on the free edge become

$$\begin{aligned}
\sigma_{11}&=\mu\left[\frac{4r}{a^2}\right]^{\frac{1}{2\beta+2}}\left[\bar{n}^2b^2r^{2(\bar{n}-1)}\sec^2(\bar{n}\pi)+\mathfrak{o}\left(r^{2(\bar{n}-1)}\right)+\mathcal{O}\left(r^{\beta(3-2\bar{n})}\right)\right],\\
\sigma_{12}&=\mu\left[\frac{4r}{a^2}\right]^{\frac{1}{2\beta+2}}\left[\left(-\bar{n}br^{\bar{n}-1}\sec(\bar{n}\pi)\right)\left(-\tfrac{1}{2}ar^{-1/2}\right)+\mathfrak{o}\left(r^{\bar{n}-3/2}\right)\right],\\
\sigma_{22}&=\mu\left[\frac{4r}{a^2}\right]^{\frac{1}{2\beta+2}}\left[\tfrac{1}{4}a^2r^{-1}+\mathfrak{o}\left(r^{2(\bar{n}-1)}\right)+\mathcal{O}\left(r^{\beta(3-2\bar{n})}\right)\right],
\end{aligned}$$

which for any $\beta>0$ yields

$$\sigma_{11}(r,\pi)=\mu b^2\bar{n}^2\left(1+\xi^2\right)\left(\frac{2}{a}\right)^{\frac{1}{\beta+1}}r^{\frac{4(\bar{n}-1)(\beta+1)+1}{2\beta+2}}+\mathfrak{o}\left(r^{\frac{4(\bar{n}-1)(\beta+1)+1}{2\beta+2}}\right), \tag{5.24a}$$

$$\sigma_{12}(r,\pi)=-\mu\left(b\bar{n}\sqrt{1+\xi^2}\right)\left(\frac{a}{2}\right)^{\frac{\beta}{\beta+1}}r^{\frac{(2\bar{n}-3)(\beta+1)+1}{2\beta+2}}+\mathfrak{o}\left(r^{\frac{(2\bar{n}-3)(\beta+1)+1}{2\beta+2}}\right), \tag{5.24b}$$

$$\text{and}\quad \sigma_{22}(r,\pi)=\mu\left(\frac{a}{2}\right)^{\frac{2\beta+1}{\beta+1}}r^{-\frac{2\beta+1}{2\beta+2}}+\mathfrak{o}\left(r^{-\frac{2\beta+1}{2\beta+2}}\right). \tag{5.24c}$$

Another important finding is that the near-field order (as $r\to 0$) of the Cauchy stress expressions in Eqns. (4.36) and (5.24) depend on the value of $\bar{n}$ and by proxy ξ. As a counterpart to the blunting and sharpening discussed previously in this section, when post loaded frictional blunting is imposed on the bonded edge, then $\bar{n}>1$ (and $\xi>0$) the normal stress $\sigma_{22}=\mathcal{O}\left(r^{1/2-\bar{n}}\right)$ which is of higher asymptotic order than both the no-slip and frictionless cases. Correspondingly, this blunting results in the other normal stress component $\sigma_{11}=\mathcal{O}\left(r^{\bar{n}-1/2}\right)$ which has lower asymptotic order than the frictionless case.

The shear stress component with finite friction is of the order $\sigma_{12} = \mathcal{O}(1)$. Defining the difference between the finite friction and frictionless shear stress magnitudes as $\bar{\chi}$, then using Eqns. (4.36b) and (4.17b)

$$\bar{\chi} \equiv |\sigma_{12}|_{\xi\neq 0} - |\sigma_{12}|_{\xi=0} = |\tan[\bar{n}\pi - (\bar{n}-1/2)\theta]| - |\tan(\theta/2)|.$$

In the range $0 \leq \theta \leq \pi$, we find that for any real values of $\bar{n} > 1$ that $\bar{\chi} < 0$. However, using the same arguments we see that in the sharpening case ($\bar{n} < 1$, and $\xi < 0$) has the opposite effects.

So, compared to the frictionless case: when blunted, the presence of interfacial slip friction reduces σ_{11}, nominally decreases the shear stress σ_{12} and dramatically increases the normal stresses σ_{22}. However, and more interestingly, we can also conclude that slip friction when pulled to the left actually increases the overall magnitude of the imposed shear σ_{12} and dramatically reduces the order of the normal stress σ_{22} while increasing σ_{11}. Compared to the no-slip case, it can be concluded that the same effect occurs with σ_{22} that increases or decreases when interfacial friction blunts or sharpens respectively. From an adhesive strength perspective, this result indicates that interfacial slippage can increase or decrease depending on which direction the material is pulled. Recall from Section 5.1 that the transition happens when the no-slip constant $a_1 = 0$ and further discussion of how this transition happens is quantified in Sections 7.2.

From Eqns. (5.24), the dependence on $\bar{n}$ disappears in the σ_{22} term but resides in the σ_{11} and σ_{12} terms. For σ_{22}, the order of singularity depends only on β and indicates that for incompressible materials ($\beta \to \infty$) that $\sigma_{22}(r,\pi) = \mathcal{O}\left(r^{-1}\right)$ and has the same order as the no-slip case on the free edge (recall Eqn. (5.16c)). While away from the free edge ($\theta \neq \pi$), σ_{11} and σ_{12} are finite as $r \to 0$, Eqns. (5.24a) and (5.24b) show that asymptotic dominance increases with σ_{12} which was always being singular for the range given in (4.12) and when $\bar{n} < (4\beta+5)/(4\beta+4)$ the normal stress σ_{11} is also singular.

Finally, it must be noted that the $\mathcal{J}$-integral may not be directly used here. Park et al [74] pointed out that with mixed-mode problems, true path independence is not clearly shown. To explain this point, a diagram showing how the traction σ versus separation in the tangential x_1 direction may change depending on the stretch of the material in the normal x_2 direction, indicating that linear superposition of traction separation in the normal x_2 and tangential x_1 directions does not hold. Given the ambiguity here, this analysis not pursued but may be the subject of future works.

Part III

Numerical Simulations

6 - Finite Element Analysis Model

6.1 Setup and Geometry

In order to compare and utilize the analytical findings from Chapters 4 and 5, an extensive finite element analysis (FEA) study was done utilizing the commercial software ABAQUS (versions 6.12 and 6.13, by Dassault Systems Simulia Corp., Providence, RI). For these simulations, the ABAQUS Hyperfoam model [100] was used, which has the form

$$\psi = \sum_{i=1}^{N} \frac{2\mu_i}{\bar{\alpha}_i^2}\left[I_1 - 3 + \frac{1}{\beta_i}\left(\left(\frac{J_{th}}{J}\right)^{\alpha_i\beta_i} - 1\right)\right], \tag{6.1}$$

where $\bar{\alpha}_i$, β_i and μ_i are material constants which may or may not depend on temperature and the total value of N allows for fitting for up to six terms. Here, we simply use $N = 1$ and note that $\beta_i \equiv \beta$, $\mu_i \equiv \mu$, and J_{th} is the ratio of the material volumetric expansion due to thermal effects so that

$$J_{th} \equiv \left(1 + \tilde{E}_{th}\right)^3, \tag{6.2}$$

with $\tilde{E}_{th}$ being the linear coefficient of thermal expansion. With the thermal effects turned off, then $J_{th} = 1$. In plane strain $I_1 = I + 1$, and choosing the material constant $\bar{\alpha}_1 = 2$ then we

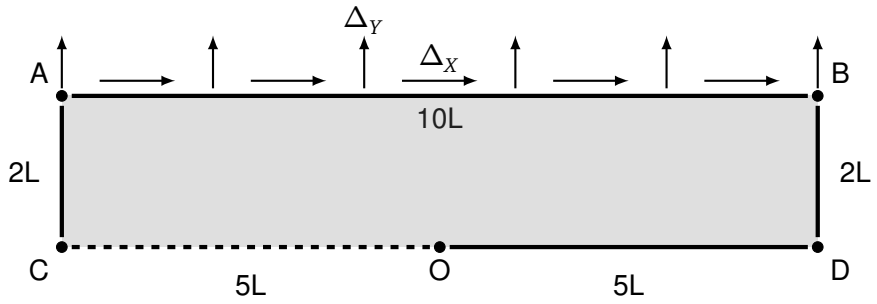

Figure 6.1: FEA Setup Geometry

are left with the Blatz-Ko strain energy density function given by Eqn. (3.23).

The goal is to model something resembling the three examples of plane strain shown in Figures 1.2, which also has geometry similar to the half-plane problem shown in Figure 3.1 and requires a reasonably large geometry (thick and long) with finely sized elements near an interface crack tip. The undeformed geometry used for all simulations discussed in this manuscript is shown in Figure 6.1 with a dimensional characteristic length L. The point "O" represents the origin (and crack tip, where $r = 0$) with triangular mesh elements sized $0.0001L$ increasing radially outward to $0.05L$-sized quad-dominated elements on faces AC, AB and BD. The sides OD and CO (the dashed line) represent the bonded edge ($\theta = 0$) and the traction free edge ($\theta = \pi$) respectively. Since these edges are of most interest near the crack tip O, the mesh sizes along OD and CO increase from $0.0001L$ to $0.05L$ sized elements from O toward points D and C. The mesh described here was found through refinement and validated at various stages as described in Sections 6.3, 7.1 and 8.1

To simulate far-field pulling and tearing loads, the traction is applied across the entire top face (AB) in the form of nominal and lateral displacement, with Δ_X and Δ_Y being positive in the directions shown in Figure 6.1. The far left and right edges (AC and BD respectively) had varied conditions depending on the study and date of simulation. See the remarks in the other studies found in the later sections for specific conditions.

To explore solutions that most resemble an incompressible material, it was intended to

make β as large as possible. However, with simulations using values $\beta > 25$, numerical instabilities occurred. The reason for these instabilities can be understood when considering that as $\beta \to \infty$, we approach the incompressible case where $J \to 1$. Consider the body Eqns. (3.27), where evaluation requires numerical integration of each term and evaluation of J (a number very close to unity) to a large negative power. While the $J^{-2(\beta+1)}$ term should remain close to unity, the numerical error in this term can become quite large. Values up to $\beta = 24.5$ ($\nu = 0.49$) were used in each study to determine the effects of nearly incompressible materials.

It must also be noted here that in the cases of pure lateral strain to the left ($\Delta_Y = 0$ and $\Delta_X < 0$), the material deflection away from the crack tip on the traction free edge displaced below the $\hat{\mathbf{E}}_1$ axis, meaning the material had self contact with the substrate. This result is not by any means unreasonable, as experimental studies showed that with large lateral strain a similar result where the free edge had self contact with the substrate to which the elastomer was bonded [66]. The numerical model utilized was not designed with surface contact in mind, mainly because we used a traction free condition without displacement constraints when $\theta = \pi$. Due to this, all numerical studies discussed in later sections utilized at least a small amount of positive normal loading ($\Delta_Y > 0$) to ensure material contact would not occur at reasonable distances from the crack tip.

6.2 Tie in with Near Field Solutions

Recall from Chapters 4 and 5 that the shape of the traction free edge ($\theta = \pi$) after loading was determined for the no-slip and finite friction cases to be

$$\text{No-Slip Case:} \qquad x_1 \simeq \left(\frac{a_1}{a_2}\right) x_2 - \left(\frac{1}{a_2^2}\right) x_2^2,$$

$$\text{Finite Friction Case:} \qquad x_1 \simeq \bar{x}_1 - \left(\frac{b\sqrt{1+\xi^2}}{a^{2\bar{n}}}\right) x_2^{2\bar{n}}.$$

Defining the point estimates

$$\hat{a}_1 \equiv \frac{a_1}{a_2}, \quad \hat{a}_2 \equiv \left(\frac{1}{a_2}\right)^2, \quad \text{and} \quad \hat{b} \equiv \frac{b\sqrt{1+\xi^2}}{a^{2\bar{n}}}, \tag{6.3}$$

then the expressions can be curve fit with the shapes of the traction free edge deflection at $\theta = \pi$, which have the form

$$\text{No-Slip:} \qquad x_1 \simeq \hat{a}_1 x_2 - \hat{a}_2 x_2^2, \tag{6.4}$$

$$\text{Finite Friction:} \qquad \bar{x}_1 - x_1 \simeq \hat{b} x_2^{2\bar{n}}. \tag{6.5}$$

Note that $\bar{x}_1$ is found directly from the data (i.e. is not a point estimate) and that with $\hat{b}$ alone it is not possible to determine both a and b uniquely. However, the finite friction case allows for slippage on the bonded edge where

$$x_1(r,0) \simeq \bar{x}_1 + b r^{\bar{n}}.$$

Noting that $X_1(r,0) = r$, then the finite friction data can also be curve fit

$$x_1 - \bar{x}_1 \simeq b X_1^{\bar{n}}. \tag{6.6}$$

So, we can determine the no-slip constants a_1 and a_2 at different loading conditions by curve fitting the point estimates $\hat{a}_1$ and $\hat{a}_2$ from Eqn. (6.4) using FEA data along the traction free edge CO (or when $\theta = \pi$). For the finite friction simulations the constant a can be determined by curve fitting the point estimates $\hat{b}$ on the edge CO (or $\theta = \pi$) and b on the edge OD (or $\theta = 0$) from Eqns. (6.5) and (6.6) respectively. Once b and $\hat{b}$ are obtained, the value for a can be found by re-arranging the definition of $\hat{b}$ from Eqn. (6.3), therefore

$$a = \left[\frac{b}{\hat{b}}\sqrt{1+\xi^2}\right]^{\frac{1}{2\bar{n}}}. \tag{6.7}$$

Note that $x_2 \geq 0$ because we do not allow inter-penetration of the substrate material, and $\sin(\theta/2) \geq 0$ for $0 \leq \theta \leq \pi$, then a must be positive and the negative root is discarded.

Given the geometry from Figure 6.1 and noting that Abaqus provides non-dimensionalized data, each point estimate must be scaled according to it's dimensions. Given this, the dimensional length L is used as a scaling reference for the coordinate variables x_1 and x_2 as well as the constant $\bar{x}_1$. From this, the constants a_1, a_2 and a all have the units $L^{1/2}$, while b and $\hat{b}$ have the units $L^{1-\bar{n}}$ and $L^{1-2\bar{n}}$ respectively.

Each point estimate described in this section was found using the Least Squares method [101]. By starting with the first few points near $r = 0$ along the edge of interest, then the number of points used were increased until the coefficient of determination, also known as the R^2 value and is a measure of how well the data fits the tested curve [101], dropped below a value of $R^2 = 0.999$. Validation methods of the analytical and FEA models are discussed in Section 6.3.

6.3 Numerical Validation Methods

Several other measures of validation of the analytical model were also used on top of mesh refinement and evaluating the coefficient of determination for the point estimates which were described in the previous section. For example, recall the Cauchy stresses on the bonded edge ($\theta = 0$ in Eqns. (4.17) and (4.36)), where

No-Slip Stresses

$$\sigma_{11} \simeq \mu\left(\frac{a_1^2}{2a_2}\right) r^{-1/2},$$
$$\sigma_{12} \simeq \mu\left(\frac{a_1}{2}\right) r^{-1/2}, \quad \text{and}$$
$$\sigma_{22} \simeq \mu\left(\frac{a_2}{2}\right) r^{-1/2}.$$

Finite Friction Stresses

$$\sigma_{11} \simeq \mu\left(\frac{2b\bar{n}}{a}\right)\left(\xi^2 + 1\right) r^{\bar{n}-1/2},$$
$$\sigma_{12} \simeq \tau, \quad \text{and}$$
$$\sigma_{22} \simeq \mu\left(\frac{a}{2b\bar{n}}\right) r^{1/2-\bar{n}}.$$

For each case, the slope of stress versus the crack tip distance (a log-log plot is required for this) should directly match the powers in the equations shown above. Meaning that when

$\theta = 0$ as $r \to 0$, for each case below:

No-Slip: σ_{11}, σ_{12}, and $\sigma_{22} \to \mathcal{O}\left(r^{-1/2}\right)$,

Finite Friction: $\sigma_{11} \to \mathcal{O}\left(r^{\bar{n}-1/2}\right)$, $\sigma_{12} \to \tau$, and $\sigma_{22} \to \mathcal{O}\left(r^{1/2-\bar{n}}\right)$.

For further validation, the constants a_1, a_2, a and b found from the point estimates from Eqns. (6.4), (6.5), and (6.6) can be used to compute the stresses on the bonded edge ($\theta = 0$) and a direct comparison to the FEA data on the bonded edge can then be made. As the FEA mesh was being refined, the number of elements were increased until the stress magnitudes on the bonded edge showed reasonable agreement with the expected values. Validation plots and details for each specific simulation are described in the upcoming sections.

7 - FEA: Extents of Friction

7.1 Extents of Friction with Normal Loading

A series of no-slip and frictionless FEA studies were done using the geometry from Figure 6.1, as described in Section 6.1. For the simulations in this section, the far right and left edges (AC and BD) were allowed to slide freely in the vertical direction but constrained in the horizontal direction. The reason for this choice was because the wedge angle ϕ was of most interest and by constraining horizontal deflection on the edges AC and BD it was anticipated that through lateral material contraction (i.e. Hooke's Law), larger ranges of the wedge angle ϕ could be observed.

Recall from Section 4.3 that the wedge angle was shown analytically to be $\phi = \pi/2$ in finite friction and had interfacial slippage of the interface crack tip denoted by the quantity $\bar{x}_1$ from Eqn. (4.28a). To best visualize this effect with finite friction, the edges AC and BD were set as traction free edges and movement was not restricted so that these edges resembled the same traction free conditions as edge CO. So, in order to understand and compare the transition process between no-slip and finite friction, the studies from Section 7.2 also used this condition. For the comparison between the extents of friction with normal loading, the top edge (AB) was deflected upwards with no lateral movement ($\Delta_Y > 0$ and $\Delta_X = 0$).

The vertical far-field displacement was then increased (in steps) as necessary for numerical convergence to reach 100% normal strain, or $\Delta_Y \to 2.0L$.

A validation example with $\Delta_Y = 2.0L$ can be seen in Figure 7.1 with $\beta = 4.5$. Figure 7.1a shows the crack opening shape along the traction free edge ($\theta = \pi$) of the FEA data together with the curve fit of Eqn. (5.2). This data set produced a wedge angle $\phi < \pi/2$ and showed excellent agreement with the near the crack tip ($r \to 0$) opening shape. However, these plots quickly deviate from each other beyond the values used for point estimates. The FEA data of the stresses on the bonded edge ($\theta = 0$) are plotted in Figure 7.1b along with curves with $\mathcal{O}\left(r^{-1/2}\right)$ for comparison. The slopes of these log-log plots also show good agreement with the expected values. Using the values determined from the deflection in this example, the coefficients were determined to be $a_1 \simeq 0.5918L^{1/2}$ and $a_2 \simeq 2.2545L^{1/2}$ so that the stresses near $r \to 0$ on the bonded edge ($\theta = 0$) are

$$\frac{\sigma_{11}\sqrt{r}}{\mu} \simeq 0.0777, \quad \frac{\sigma_{12}\sqrt{r}}{\mu} \simeq 0.2959, \quad \text{and} \quad \frac{\sigma_{22}\sqrt{r}}{\mu} \simeq 1.1273. \tag{7.1}$$

We can also approximate the stress coefficients using the first two data points for each stress field in Figure 7.1b. For example, assuming the form for each Cauchy stress $\sigma_{ij} \propto \bar{\sigma}_{ij} r^{-1/2}$, then

$$\begin{aligned} \frac{\bar{\sigma}_{11}}{\mu} &\simeq \frac{5.0520 - 7.1469}{(0.000202)^{-1/2} - (0.0001)^{-1/2}} = 0.0706, \\ \frac{\bar{\sigma}_{12}}{\mu} &\simeq \frac{20.88 - 29.595}{(0.000202)^{-1/2} - (0.0001)^{-1/2}} = 0.2940, \\ \text{and} \quad \frac{\bar{\sigma}_{22}}{\mu} &\simeq \frac{86.499 - 122.7}{(0.000202)^{-1/2} - (0.0001)^{-1/2}} = 1.221. \end{aligned}$$

When comparing these approximations with the ones computed in Eqn. (7.1), we see agreement within 10%.

For comparison, the same parameters as the series in Figure 7.1 ($\Delta_Y = 2.0L$ and

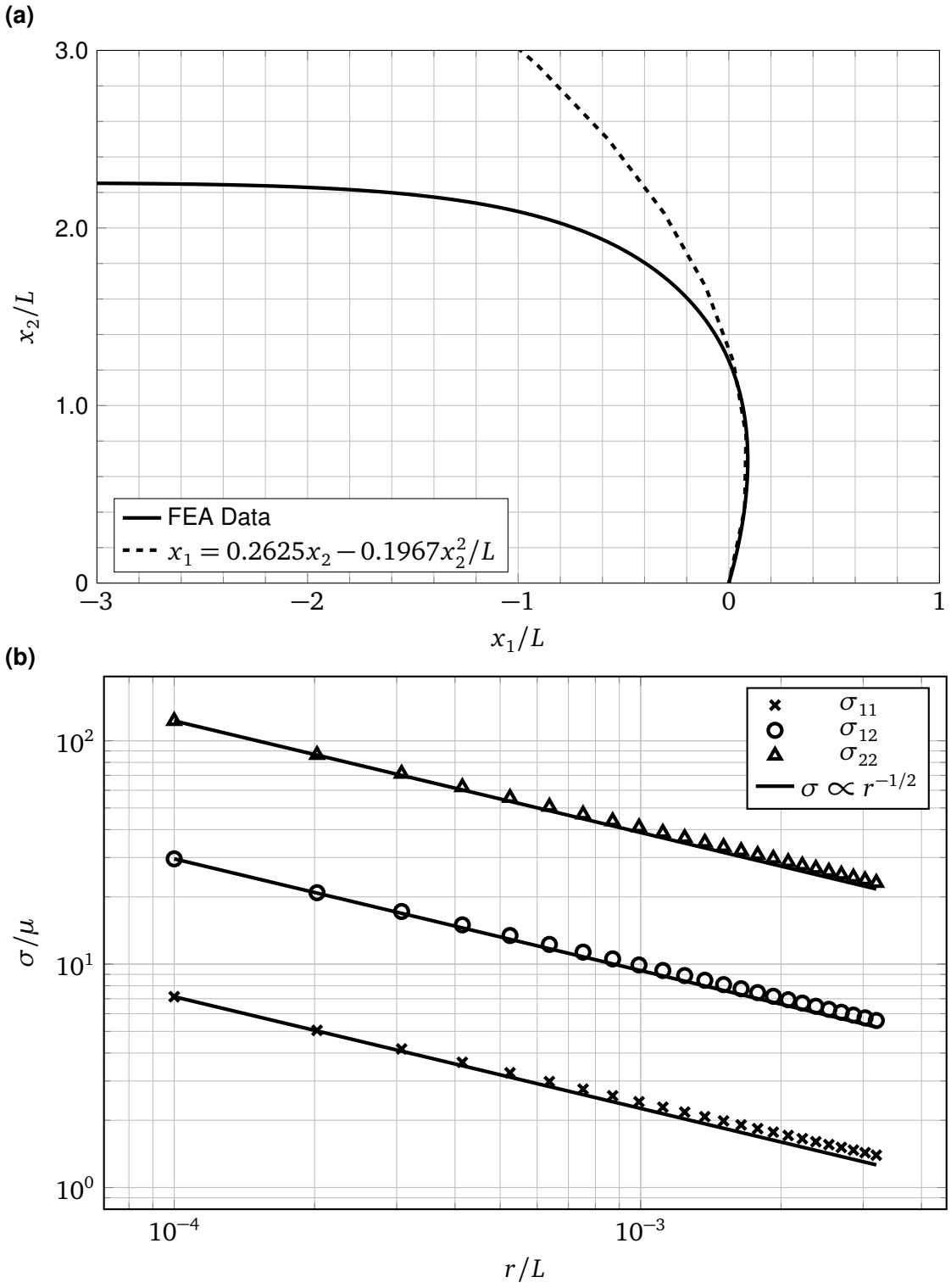

Figure 7.1: No-slip with nominal loading $\Delta_X = 0$ with $\beta = 4.5$ and $\Delta_Y = 2.0L$. (a) Deflected shape on $\theta = \pi$, (b) Cauchy stresses on $\theta = 0$.

$\beta = 4.5$) were used and with the frictionless boundary condition, we see in Figure 7.2a the expected opening geometry given by a vertical wedge angle ($\phi = \pi/2$) and the presence of interfacial slippage with a crack tip displacement of $\bar{x}_1 \simeq 0.9787L$. The constants a and b for this example can not be computed directly without curve fitting for b using the deformation along the bonded edge (recall Eqn. (5.1)), however further validation of finite friction cases is more completely covered in Section 8.1. As expected via Eqns. (4.36), the stresses on the bonded edge (see Figure 7.2b) show the expected order (the slope of the log-log plots) in r so that $\sigma_{11} \sim \mathcal{O}\left(r^{1/2}\right)$ and $\sigma_{22} \sim \mathcal{O}\left(r^{-1/2}\right)$ at $\theta = 0$ near $r \to 0$.

Proceeding with the conclusion that everything is in order, an extensive set of simulations with normal loading was performed using the no-slip boundary condition and various values of β. The wedge angle ϕ was computed from each data set using Eqn. (5.4). The effect of applied normal loading Δ_Y on the wedge angle ϕ with various values of β is shown in Figure 7.3. At small applied displacements ($\Delta_Y < 0.1L$), the wedge angle ϕ dramatically decreases from $\phi = \pi$ (the undeformed wedge angle) to $\phi < \pi/2$. As the applied normal displacement Δ_Y increases further, the wedge angles ϕ for each value of β tend toward $\phi \to \pi/2$. The wedge angle ϕ consistently decreases as material becomes less compressible (or β increases). For example, with $\beta = 1$, the wedge angle was determined to be $\phi \simeq 1.4321$ (less than $\pi/2$) radians at $\Delta_Y = 1.0L$.

Using the same data, the effect of compressibility on the wedge angle ϕ is shown in Figure 7.4 with various applied normal displacements Δ_Y. Since we are most interested in soft elastomers with large strain, the plots where $\Delta_Y < 0.1L$ were omitted here. The effect of compressibility on the wedge angle ϕ diminishes as β increases and the larger the applied normal loading Δ_Y, the wedge angle ϕ saturates (meaning $\frac{\partial \phi}{\partial \beta} \to 0$ as β increases).

The data here implies that the wedge angle $\phi \to \pi/2$ as Δ_Y increases, even for the incompressible Neo-Hookean material ($\beta \to \infty$). Also, since the effect of β on the wedge angle ϕ diminishes for large β, it is assumed that any flat portion ($\frac{\partial \phi}{\partial \beta} = 0$) from

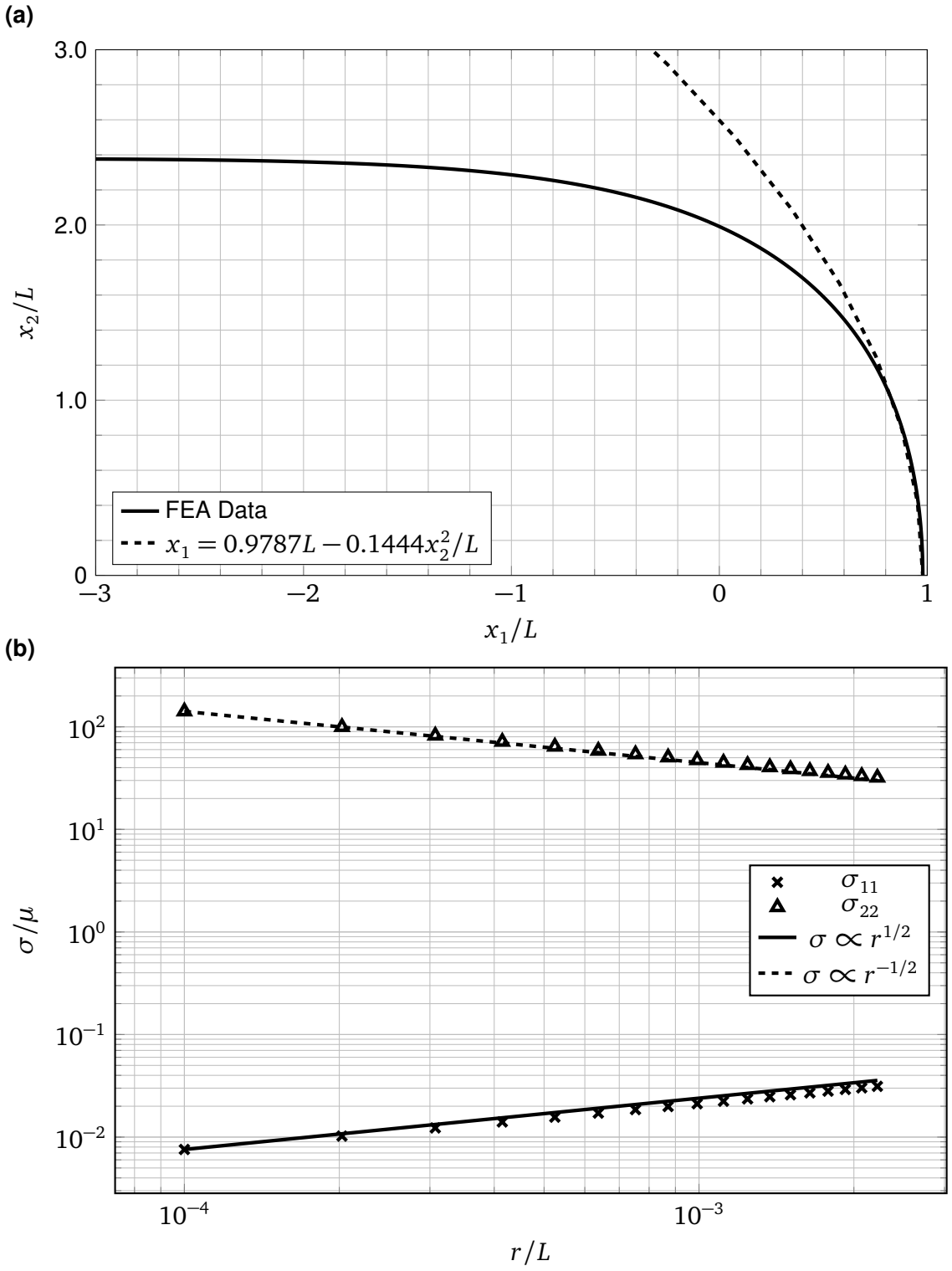

Figure 7.2: Frictionless with nominal loading $\Delta_X = 0$ with $\beta = 4.5$ and $\Delta_Y = 2.0L$. (a) Deflected shape on $\theta = \pi$, (b) Cauchy stresses on $\theta = 0$.

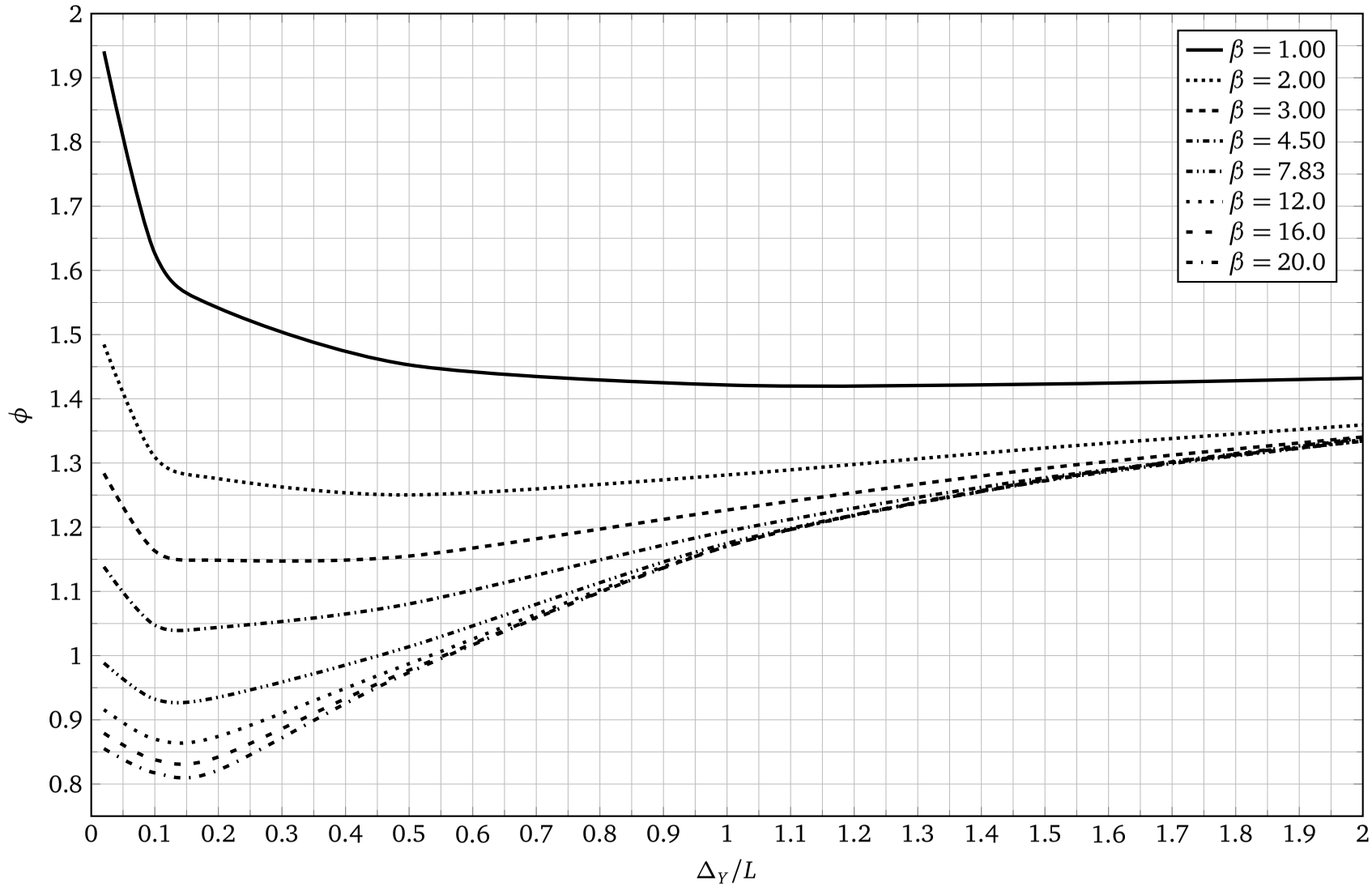

Figure 7.3: Wedge Angle ϕ versus Δ_Y in pure normal loading with various β.

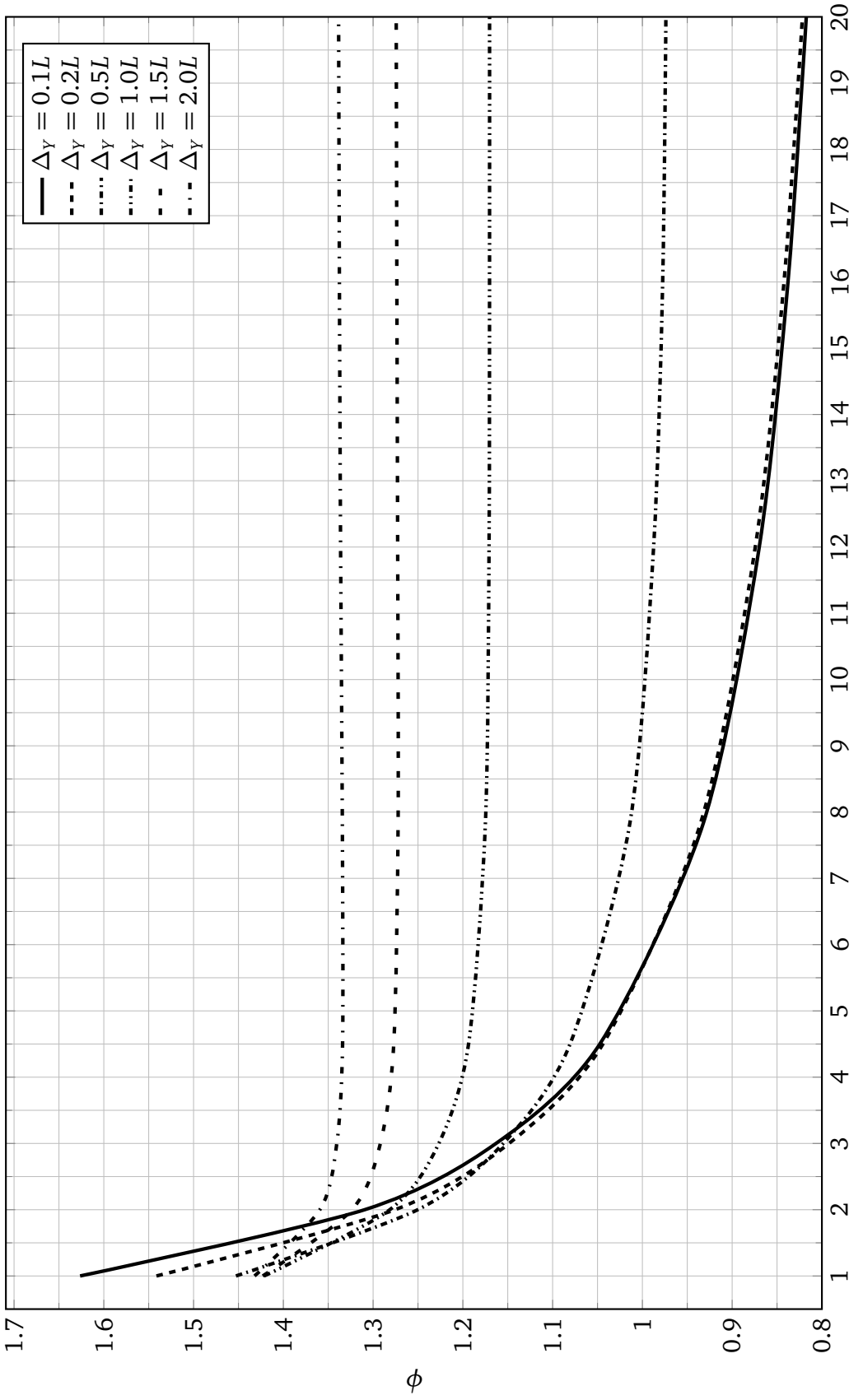

Figure 7.4: Wedge Angle ϕ versus β with various normal loading Δ_Y.

Figure 7.4 indicates insensitivity to β and should therefore approximate the incompressible Neo-Hookean case.

7.2 Lateral Loading and The Transition Angle

For the simulations described in this section, the mesh and geometry from Figure 6.1 and the far left and right sides (AC and BD) were left traction free. Here, the effect of lateral loading ($\Delta_X \neq 0$) on the top face AB with no-slip conditions on OD are discussed. In each simulation run, a small amount of positive normal loading ($\Delta_Y > 0$) was needed to ensure material inter-penetration did not occur along the free edge CO.

Recall from Section 5.1 that when $a_1 = 0$, the no slip case solution outlined in Table 4.2 yields a wedge angle $\phi = \pi/2$ and the corresponding stress $\sigma_{12} \to 0$ on the bonded surface ($\theta = 0$). Given that the numerical runs with only normal loading ($\Delta_X = 0$) all showed positive shear on the bonded surface, it is logical to look for some loading angle less than $\alpha < \pi/2$ where this transition occurs. Recall that the load angle α was defined in Section 1.2 from the negative horizontal axis (from the left) so that

$$\tan\alpha \equiv -\frac{\Delta_Y}{\Delta_X}, \quad 0 \leq \alpha \leq \pi, \tag{7.2}$$

and we expect the transition to happen at some critical loading angle $\tilde{\alpha}$ somewhere in the range $0 \leq \alpha < \pi/2$ so that the loading on the top face AB produces a vertical wedge angle $\phi = \pi/2$. The total loading displacement is represented as Δ and is defined as

$$\Delta \equiv \sqrt{\Delta_X^2 + \Delta_Y^2}. \tag{7.3}$$

Numerically, this critical loading angle $\tilde{\alpha}$ can be iteratively found by applying the no-slip conditions at various load angles α until the induced shear stress on the bonded edge yields $\sigma_{12} = 0$.

An example of this method is outlined in Figure 7.5, where various loading angles were imposed on the top face AB using $\beta = 24.5$. Figures 7.5a and 7.5b show the near-field deformed geometry and stresses using $\Delta_X = 1.002L$ and $\Delta_Y = 0.5L$ ($\Delta = 1.12L$ and $\alpha = 0.463$ rad). In this case, negative shear stress is induced on the bonded edge and corresponding to a finite wedge angle $\phi > \pi/2$, which matches the expected deformed shape in the form of Eqn. (5.2). Also, the asymptotic order of the in-plane Cauchy stresses all showed $\sigma \simeq \mathcal{O}\big(r^{-1/2}\big)$. From this point, the lateral loading Δ_X can be increased (or the magnitude reduced). However, it is also possible to determine the effects of total loading Δ. Keeping this loading displacement the same as Figures 7.5a and 7.5b ($\Delta = 1.12L$) and increasing the load angle α until the critical loading angle $\tilde{\alpha}$ is reached, shown in Figures 7.5c and 7.5d, the critical loading angle was found to be $\tilde{\alpha} \simeq 1.103$ rad. From Figure 7.5d, it is confirmed that the normal stresses $\sigma_{11} = \mathcal{O}\big(r^{1/2}\big)$ and $\sigma_{22} = \mathcal{O}\big(r^{-1/2}\big)$ and the no-slip case takes the form of the frictionless case with no interfacial slippage ($\bar{x}_1 = 0$); a result previously found by making $a_1 = 0$ in Eqn. (5.5). If the loading angle α is increased with the same total deflected loading ($\Delta = 1.12L$), then the deflection and stress state revert back to the no-slip result (Figures 7.5e and 7.5f) with a finite wedge angle ϕ and all three stresses again showed the asymptotic order $\sigma = \mathcal{O}\big(r^{-1/2}\big)$.

The critical angle $\tilde{\alpha}$ with respect to loading magnitude Δ is shown in Figure 7.6a. As the total loading Δ increases, the critical angle appears to approach $\tilde{\alpha} \to \pi/2$. For loading above $\Delta \simeq 0.7L$, the data fit nicely with a quadratic as shown in Figure 7.6b and for the range and geometry used it was determined

$$\tilde{\alpha}(\Delta) \simeq \frac{\pi}{2} - \frac{L^2}{\Delta[0.405\Delta + 1.50L]}, \qquad \text{where} \quad \Delta \geq 0.7L. \tag{7.4}$$

From this, we can conclude that the imposed stress on the bonded edge depends on the total material stretch Δ. This also clearly shows a link between material stretch and the induced slippage direction. If a material can not undergo a large amount of stretch or if the load is

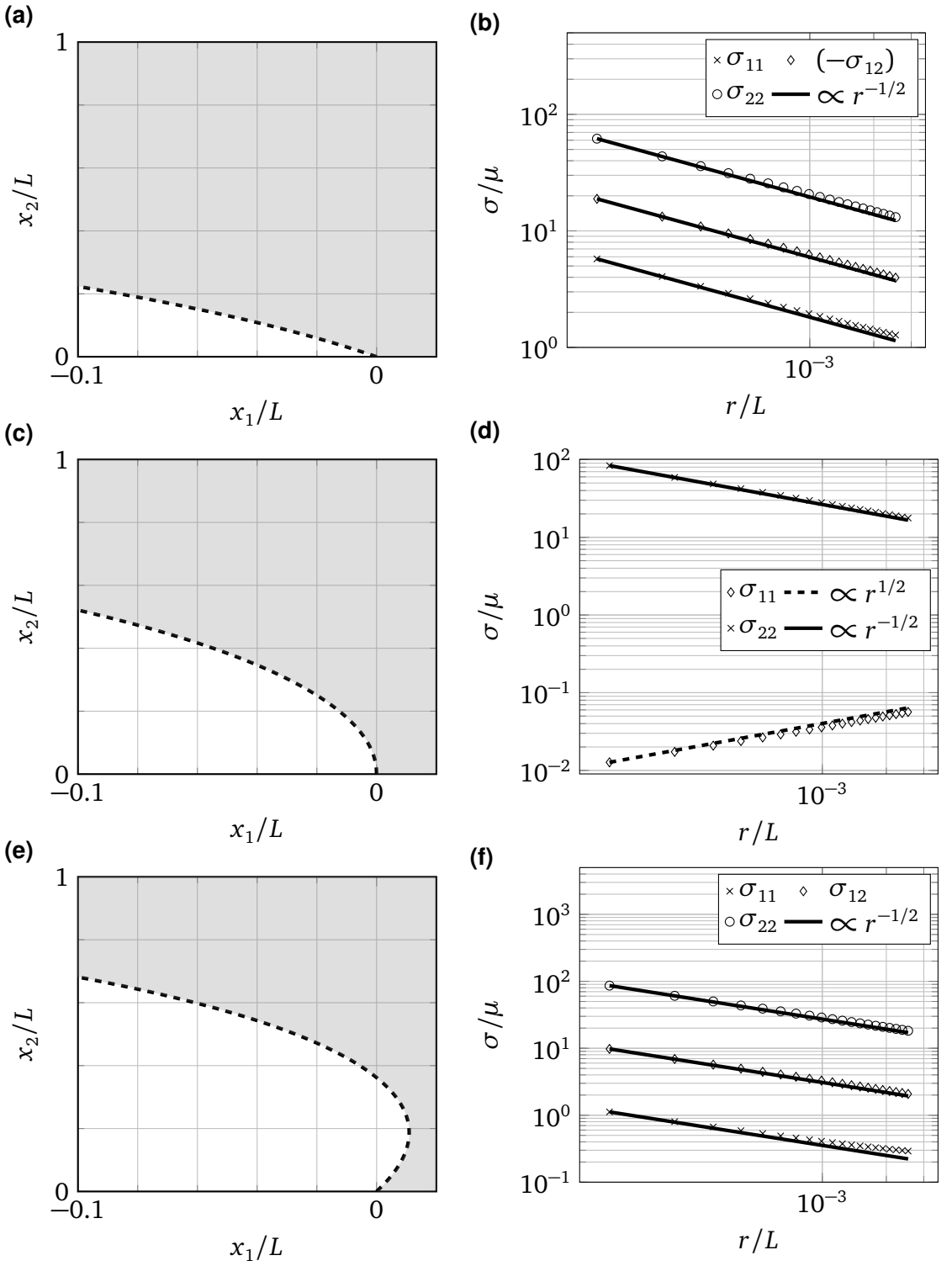

Figure 7.5: Example of the effect of the pull/peel angle α on the no-slip case using $\Delta = 1.12L$ and $\tilde{\alpha} = 1.103$ rad. (a) Crack opening shape with $\alpha = 0.463$ rad (b) Bonded edge stress with $\alpha = 0.463$ rad (c) Crack opening shape with $\alpha = \tilde{\alpha}$ (d) Bonded edge stress with $\alpha = \tilde{\alpha}$ (e) Crack opening shape with $\alpha = 1.337$ rad (f) Bonded edge stress $\alpha = 1.337$ rad.

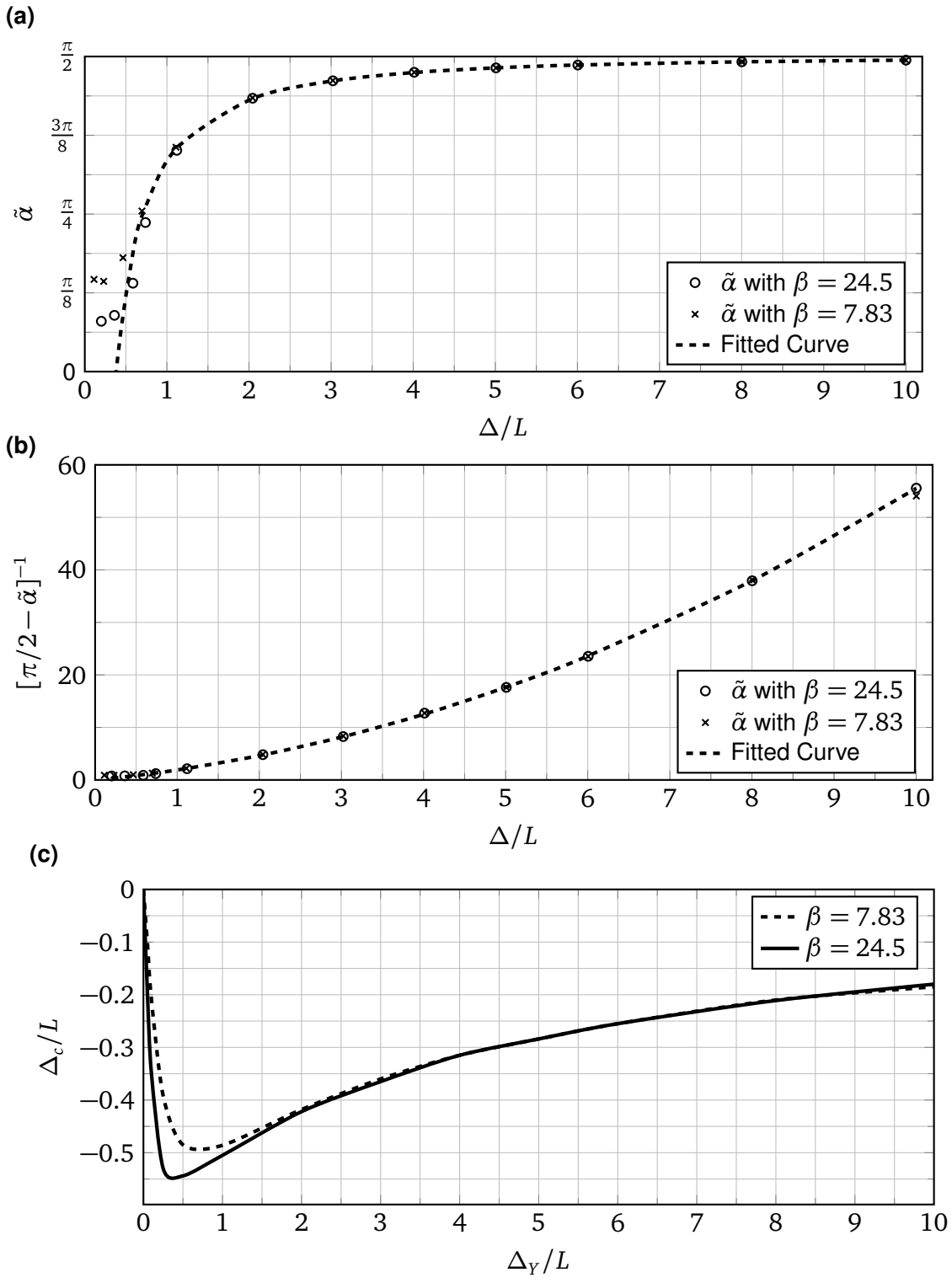

Figure 7.6: Critical loading direction versus total deflection.
(a) $\tilde{\alpha}$ versus Δ (b) Correlation plot for $\tilde{\alpha}$ (c) Δ_c versus Δ_Y.

minimal (i.e. Δ is small), then the corresponding critical angle $\tilde{\alpha}$ will be much smaller than if the material can undergo more stretch. The same data set can be shown in a different way by defining the critical lateral loading Δ_c as the corresponding Δ_X value with respect to normal loading Δ_Y. In Figure 7.6c, we find that the magnitude of critical lateral loading Δ_c sharply increases when normal loading $\Delta_Y \leq 0.7L$, then reaches a minimum value near $\Delta_Y \simeq 0.7L$. Beyond a normal deflection load of $\Delta_Y > 0.7L$, the compressibility parameter β has little effect and $\Delta_c \to 0$ where the curve fit from Eqn. (7.4) is viable.

From these results, we now have a good starting point for determining the sign of the induced shear on the bonded edge, hence the sign of ξ for each finite friction simulation described in Chapter 8.

8 - FEA: Finite Friction

8.1 Finite Friction - Methods and Validation

For the simulations with a non-zero, finite slippage threshold $\xi \neq 0$, the boundary condition in Eqn. (3.10) was used from the crack tip inwards (from point O toward point D in Figure 6.1) inside the length of the slip-zone (defined as δ). The value of δ for each data point was determined using an iterative process. Starting with the no-slip condition (Eqn. (3.11)) across the entire bonded edge OD, a finite stress was imposed starting at point O (where a shear stress singularity occurs in the no-slip case) some finite length to the right (towards point D). With a finite stress imposed inside the slip-zone length δ_{guess}, it was simultaneously ensured that beyond the range $r > \delta_{\text{guess}}$ the material remained bonded following the no-slip condition from Eqn. (3.11). Given that we have imposed a stress boundary condition when $r < \delta_{\text{guess}}$ and a displacement condition when $r > \delta_{\text{guess}}$, a natural stress concentration will occur at $r = \delta_{\text{guess}}$ if the value of δ_{guess} is not set to the correct slip zone length. To visualize this, see the shear stress output σ_{12} plot in Figure 8.1 for several iterations of δ_{guess} which were increased until the stress concentration at $r = \delta$ was no longer measurable in the output data. For the particular plot in Figure 8.1, the far-field strain was imposed on the top edge AB with $\Delta_Y = 2.0L$ and $\Delta_X = 1.0L$, and a slip threshold was

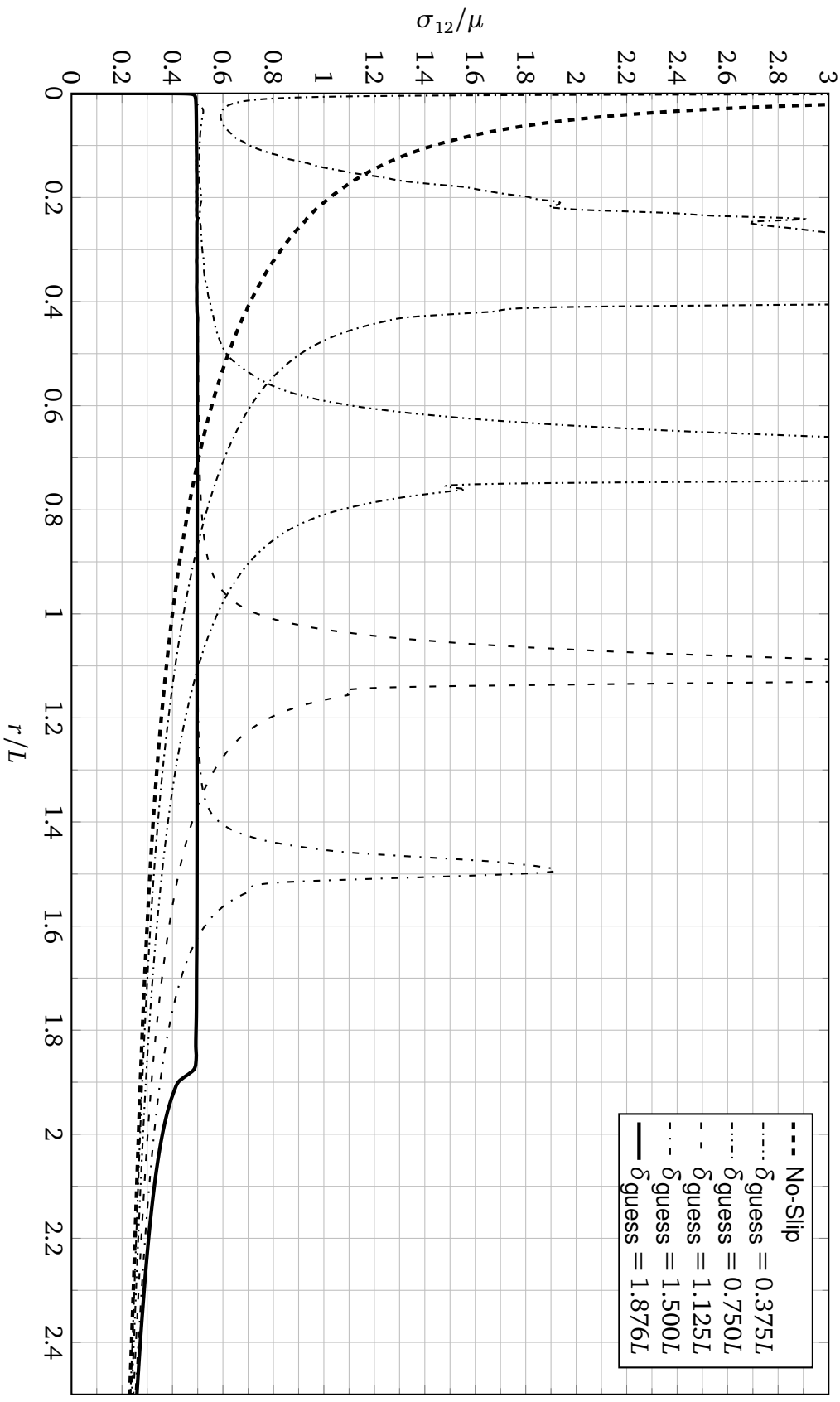

Figure 8.1: Visualization of the iteration method to find slip zone length δ for various FEA simulations with $\beta = 16.0$ and $\xi = 0.5$.

chosen to be $\xi = 0.5$ ($\bar{n} = 1.1476$). In this particular example, $\delta \simeq 1.8758L$

In all numerical exercises with non-zero, finite slippage, the stress concentration between the slip-zone and beyond ($r > \delta$) disappeared and the corresponding value of δ was then recorded. As shown in Figure 8.1, the implied condition $\sigma/\mu = \xi = 0.5$ within the slip-zone ($r \leq \delta$) was arrived at, hence the near-field form of deflection from Eqns. (4.28) is assumed viable in this range. Note that it was also apparent if a slip-zone length guess was too large ($\delta_{\text{guess}} > \delta$) because concentrations in shear stress at the transition re-appeared with spikes in both the positive and negative directions on the right and left sides of the chosen value of $r = \delta_{\text{guess}}$.

For numerical runs, the constants a and b from Eqns. (4.28) were found using the point estimates described in Section 6.2, which allow for curve fitting on both the free and bonded edges ($\theta = \pi$ and $\theta = 0$ respectively). With the point estimates $\hat{b}$ and b, the constant a can be determined from Eqn. (6.7).

Two more examples are outlined below for evaluation of this method. In the first example, shown in Figure 8.2, we chose a material with $\beta = 7.83$ in mixed mode loading with $\Delta_Y = 1.0L$, and $\Delta_X = -1.0L$ (lateral strain to the left). From the findings in Figure 7.6 and using Eqn. (7.2), the loading angle $\alpha = \pi/4$ which is less than the critical angle so that negative shear σ_{12} is expected on the bonded edge, resulting in a negative slip threshold value on the bonded edge of $\xi = -0.75$ ($\bar{n} = 0.7952$). As seen in Figure 8.2a, the shear stress output σ_{12} shows excellent agreement with the imposed stress of $\sigma_{12} = -0.75\mu$ using a slip-zone length δ to be $0.159L$ (found iteratively). The estimated crack tip displacement was determined to be $\bar{x}_1 \simeq -0.057L$ by recording the displacement of the first node along the bonded surface. Here, $\bar{x}_1$ is negative because the lateral stress σ_{12} on the bonded edge points to the left. For further validation with this example, the natural log plots of the other stress outputs σ_{11} and σ_{22} (shown in Figure 8.2b) near the crack tip along the bonded edge showed reasonable agreement with the expected slopes as per Eqns. (4.36a) and (4.36c). Figure 8.2c shows the

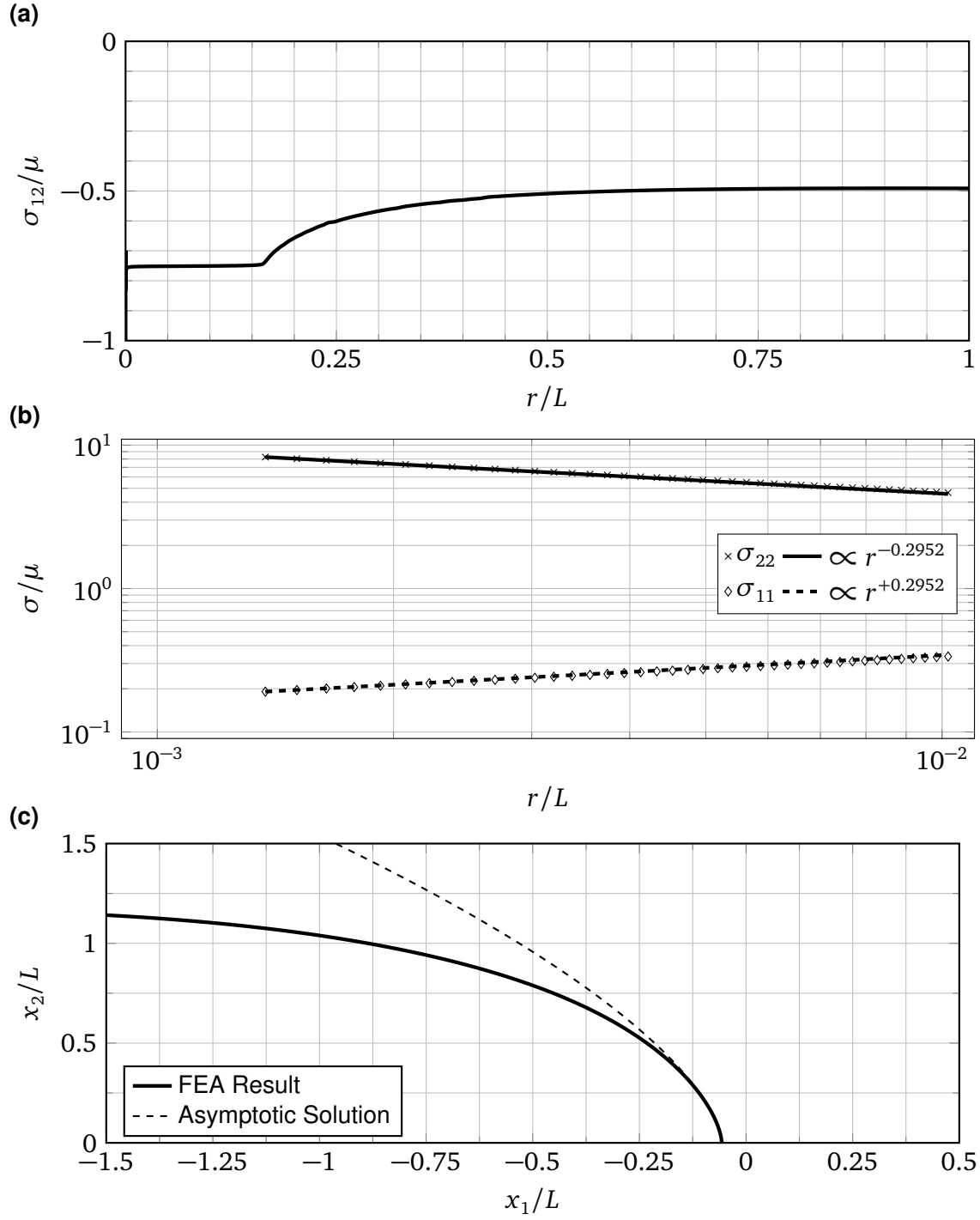

Figure 8.2: Mixed mode validation example with $\beta = 7.83$, $\Delta_X = -1.0L$, $\Delta_Y = 1.0L$ and $\xi = -0.75$ ($\bar{n} = 0.7952$)

opening shape of the free edge along with a near-field plot of Eqn. (5.22) using the fitted FEA data near the crack tip where it was determined that $\hat{b} \simeq 0.475L^{-0.590}$, $b \simeq -0.9561L^{0.205}$, and using Eqn. (6.7) the constant $a \simeq 1.786L^{1/2}$. Notice the strong correlation close to the crack tip in the two plots inside the range $r \leq \delta$. As predicted by the value of $\bar{n} = 0.7952$, the opening shape indicated a vertical wedge angle and resembles a sharpened parabola ($x_1 \propto x_2^{1.59}$).

For the second validation example (shown in Figure 8.3), the same material with $\beta = 7.83$ was used with pure normal loading so that $\Delta_Y = 4.0L$ and $\Delta_X = 0$. Since this corresponds to a loading angle $\alpha = \pi/2$, then the stress threshold is a positive value and in this case it is assumed $\xi = +1.5$ ($\therefore \bar{n} = 1.3128$). Figure 8.3a shows the shear stress output σ_{12} on the bonded edge using an applied slip-zone of $\delta \simeq 0.0816L$. In this example, the point estimates $\hat{b}$ and b were determined to be $0.0237L^{-1.626}$ and $0.660L^{-0.313}$ respectively, and the constant $a \simeq 4.447L^{1/2}$. The FEA output for the slopes of the natural log of the nominal stresses σ_{11} and σ_{22} (shown in Figure 8.3b) also show reasonable agreement inside the slip-zone. In Figure 8.3c, the constant $\bar{x}_1 \simeq 0.0523L$ (the crack tip moves to the right with this example) as well as the data plotted with the curve fit function using the point estimates with Eqn. (5.22). Here we again see the opening shape has a vertical angle but this time, due to $\bar{n} > 1$ and given the sign of the shear stress threshold, it resembles a more obtuse and blunted parabola ($x_1 \propto x_2^{2.626}$).

From both examples presented, it is concluded that the iterative technique for finding δ yields reasonable results and that the near field form of the deformation and stress fields from Table (4.3) correlate well with the FEA solutions found for each case. We move forward to the next sections where the techniques outlined in this section are utilized. An extensive normal loading study is discussed in Section 8.2 and an investigation of lateral loading is found in Section 8.3.

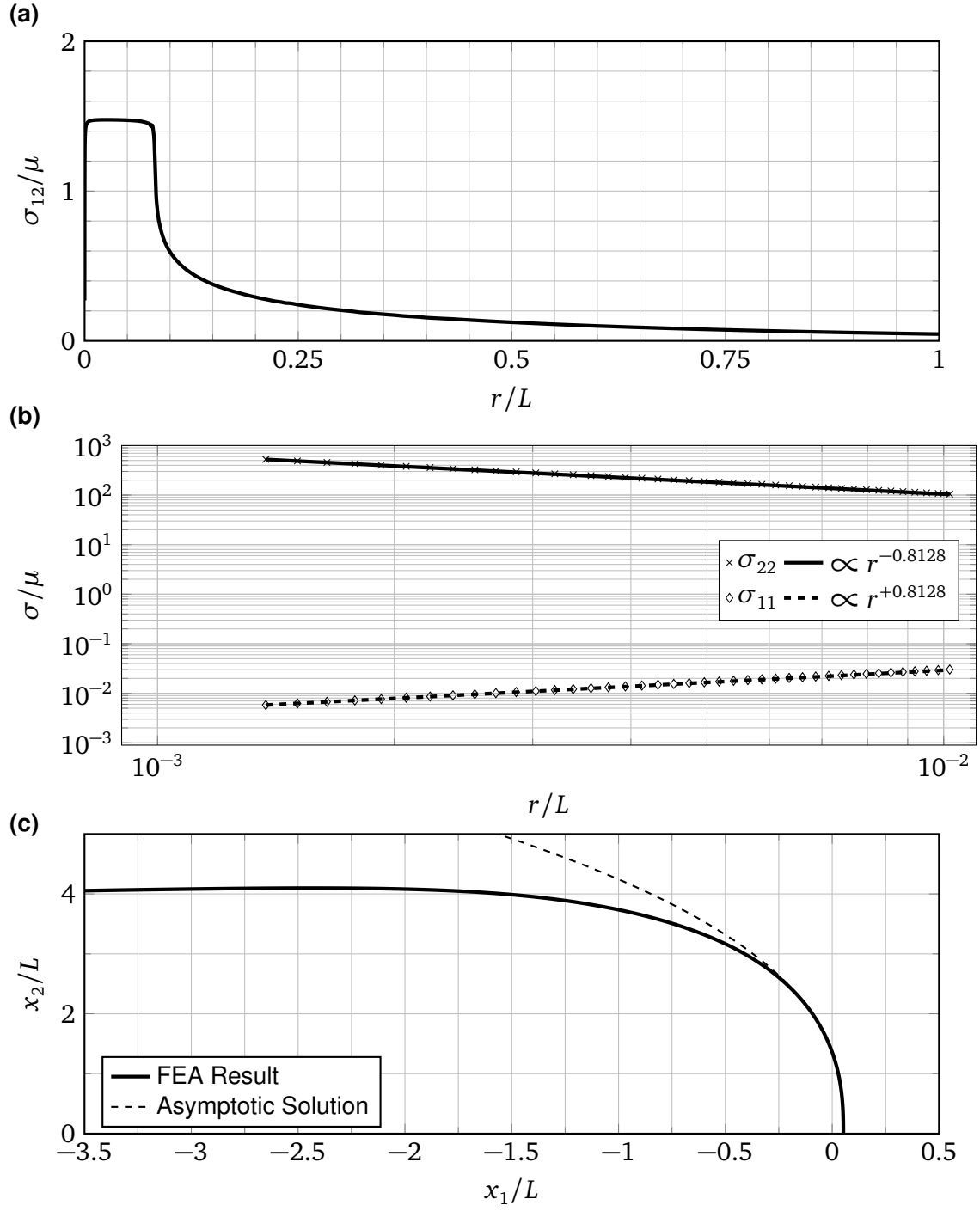

Figure 8.3: Normal loading validation example with $\beta = 7.83$, $\Delta_X = 0$, $\Delta_Y = 4.0L$ and $\xi = 1.5$ ($\bar{n} = 1.3128$)

8.2 Finite Friction With Normal Loading

In the investigation of a tearing mechanism with finite friction, the numerical case with pure normal external loading was extensively explored. Using the geometry and numerical model described in Section 8.1, with $\Delta_X = 0$ and external loading in the range $0 \leq \Delta_Y \leq 4.0L$ in increments of $0.1L$, materials with $\beta = 7.83$, 16.0 and 24.5 were evaluated. Throughout this case study, every FEA data set was used to determine the constants from Eqns. (4.28a) and (4.28b), being $\bar{x}_1$, a and b as well as the value of the slip-zone length δ.

How compressibility affects $\bar{x}_1$, a, b and δ can be seen through a comparison of the three different values of β. Results using various values of ξ are highlighted in Figures 8.4 through 8.7. In Figures 8.4a, 8.5a, 8.5b, 8.6a, 8.6b, 8.7a, and 8.7b, we see that $\bar{x}_1$ and δ converge for each values of β with loading values $\Delta_Y > 1.2L$. Note that since Figure 8.4b represents the frictionless case, the slip zone length δ encompasses the entire bonded edge which for these runs was $\delta = 5L$, and this plot is shown only for completeness. Note that in each study, the interfacial slip (expressed quantitatively through $\bar{x}_1$ and δ) increases sharply for low normal deflection until saturating in the approximate range $\Delta_Y < 0.7L$ and then reduces when loading is increased further. A connection between this finding and the transition angle $\tilde{\alpha}$ described in Section 7.2 is shown in Figure 7.6c, where the largest slippage tends to be be near the maximum value of the critical normal loading values Δ_c. When $\Delta_Y > \Delta_c$, the reduction in δ and $\bar{x}_1$ show that with this model some of the material points return to their previous unloaded values. From Figures 8.4c, 8.4d, 8.5c, 8.5d, 8.6c, 8.6d, 8.7c, and 8.7d, we see that the constants a and b did not show dependence on the compressibility parameter β in the range tested. The constant a showed a monotonically increasing value with Δ_Y, which makes sense because this constant is related to opening in the x_2 direction. The constant b, which is related to the opening deflection in the x_1 direction, appears to decrease from some large value at low loading, and tends to a constant value when $\Delta_Y > \Delta_c$ for each value of β tested.

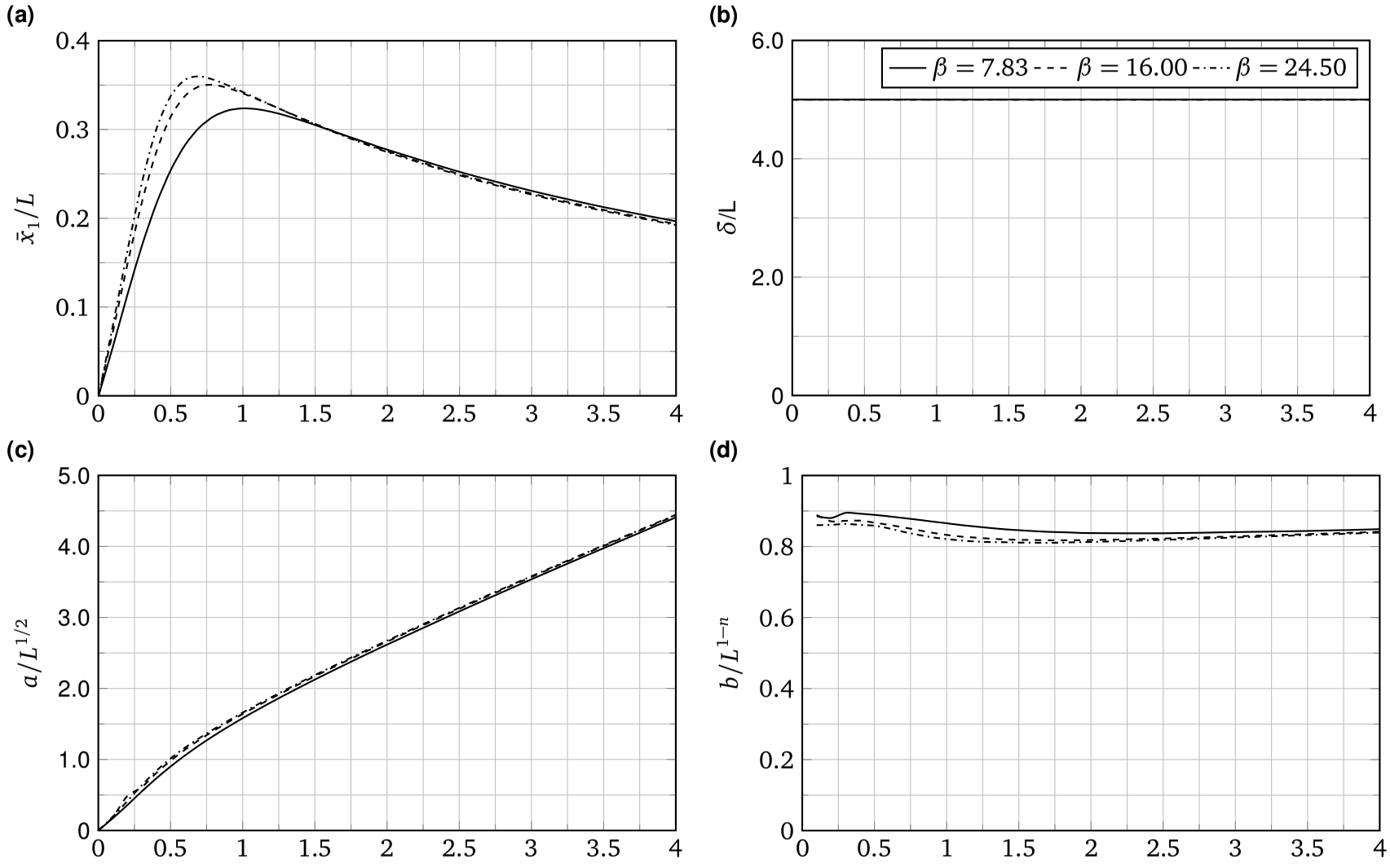

Figure 8.4: Effect of β on various parameters with nominal loading and $\xi = 0$ (frictionless condition).
(a) $\bar{x}_1/L$ vs. Δ_Y/L, (b) δ vs. Δ_Y/L, (c) a vs. Δ_Y/L, (d) b vs. Δ_Y/L.

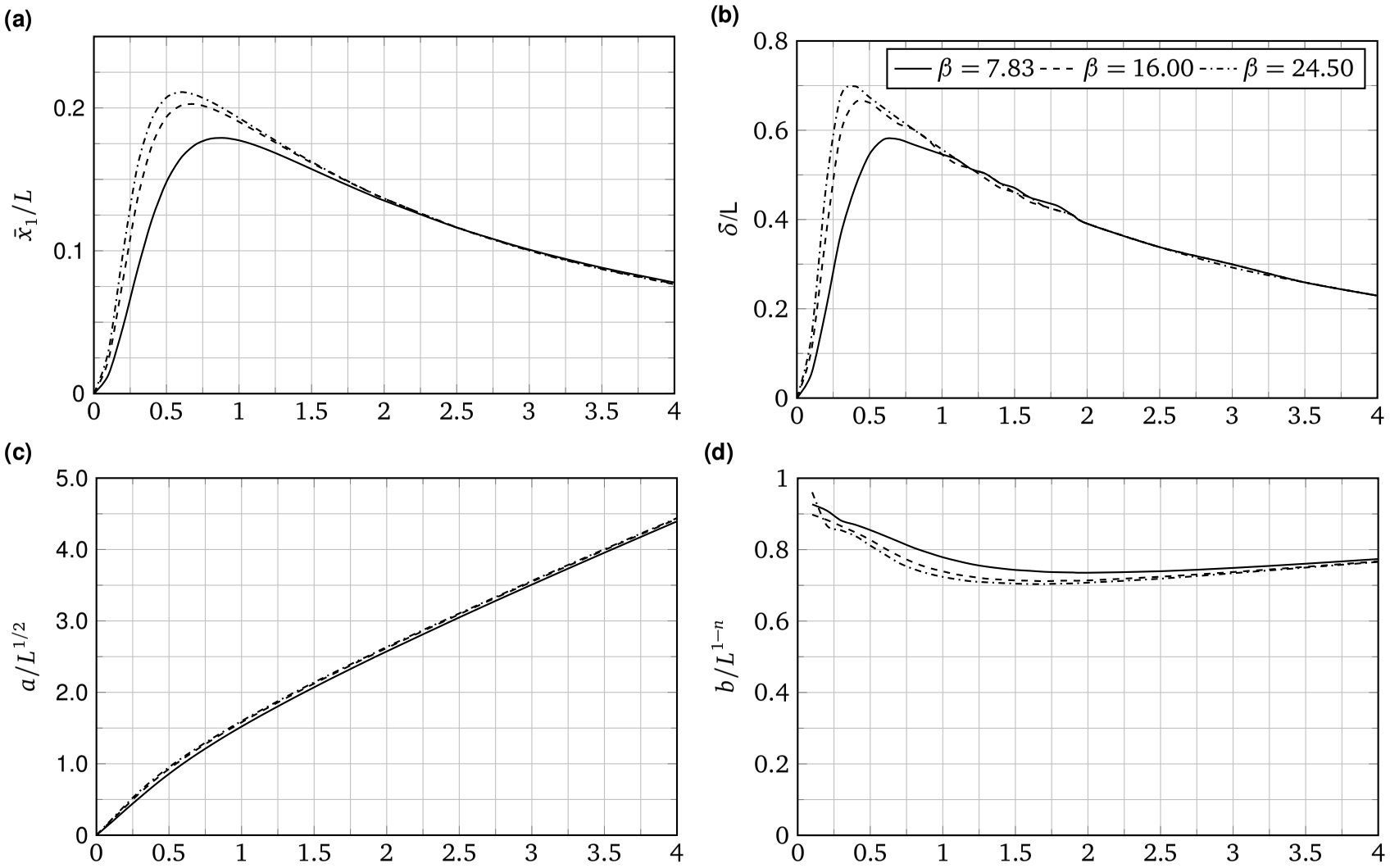

Figure 8.5: Effect of β on various parameters with nominal loading and $\xi = 0.5$.
(a) $\bar{x}_1/L$ vs. Δ_Y/L, (b) δ vs. Δ_Y/L, (c) a vs. Δ_Y/L, (d) b vs. Δ_Y/L.

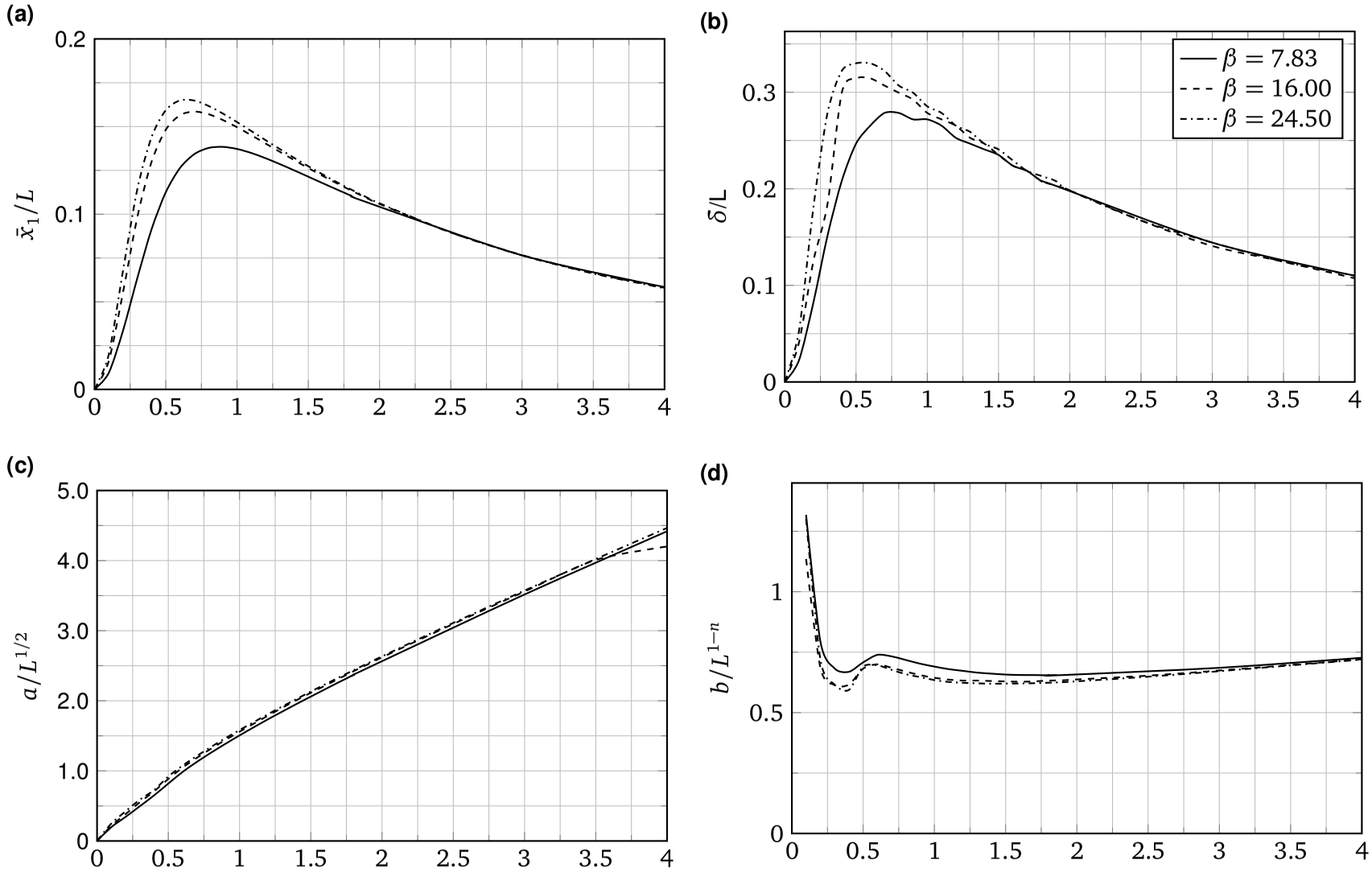

Figure 8.6: Effect of β on various parameters with nominal loading and $\xi = 1.0$.
(a) $\bar{x}_1/L$ vs. Δ_Y/L, (b) δ vs. Δ_Y/L, (c) a vs. Δ_Y/L, (d) b vs. Δ_Y/L.

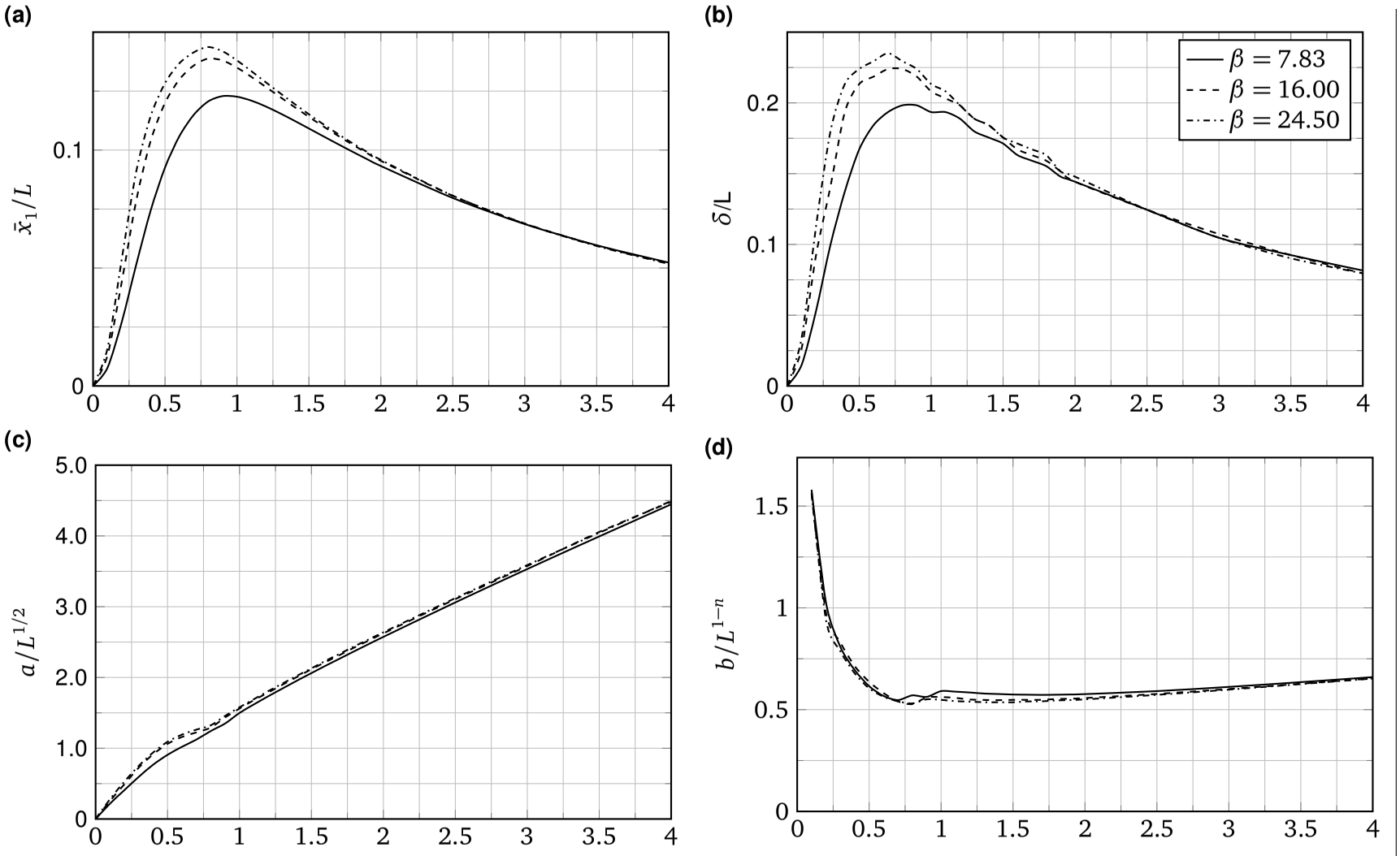

Figure 8.7: Effect of β on various parameters with nominal loading and $\xi = 1.5$.
(a) $\bar{x}_1/L$ vs. Δ_Y/L, (b) δ vs. Δ_Y/L, (c) a vs. Δ_Y/L, (d) b vs. Δ_Y/L.

To determine the effect of the slip threshold value, the same data from Figures 8.4 through 8.7 was utilized and re-plotted into Figures 8.8 through 8.10. Here, we evaluated the normal loading cases with interfacial slippage threshold values $\xi = 0.0,\ 0.5,\ 1.0$ and 1.5 given that most material shear bond strengths τ of various rubber based or pressure-sensitive adhesives (for example, see Table 27.4 of [54] from the Physical Properties of Polymers Handbook [102]) versus material tensile modulus μ (see Table 24.6 of [53]) have an ultimate material strength on the order of $\sigma_u/\mu < 1$. Therefore, no simulations with slip threshold values larger than $\xi = 1.5$ were performed. From Figures 8.8a, 8.8b, 8.9a, 8.9b, 8.10a, and 8.10b, we see a clear dependence on ξ on the material slippage constants $\bar{x}_1$ and δ, as expected. As the slip threshold is increased, the slip zone length δ and the crack tip slippage $\bar{x}_1$ are both reduced. Again, this is an expected result because a higher ξ should impede slippage. Interestingly, as seen in Figures 8.8c, 8.9c, and 8.10c, the constant a is also insensitive to the slip threshold ξ. The constant b showed moderately reduced values (see Figures 8.8d, 8.9d, and 8.10d) as ξ was increased.

Using the data from the twelve different runs discussed in this section, the constant a fit well with a quadratic curve, and assuming b is constant when $\Delta_X > \Delta_c$, dependence on ξ and Δ_Y was found to have the correlations for the geometry from Figure 6.1

$$b \simeq [-0.1727\xi + 0.8276]\, L^{1-\bar{n}} \tag{8.1}$$

$$\text{and} \quad a \simeq [-0.1445\Delta_Y + 1.648L]\, \Delta_Y L^{-3/2}. \tag{8.2}$$

In the above expressions, recall that $\bar{n}$ is a function of ξ given by Eqn. (4.27). Note that with geometry different than $10L \times 2L$, these estimates will have increasing error away from the crack tip at $r = 0$ and we assume large strains above $\Delta_Y > 1.2L$ for the correlation of b in Eqn. (8.1).

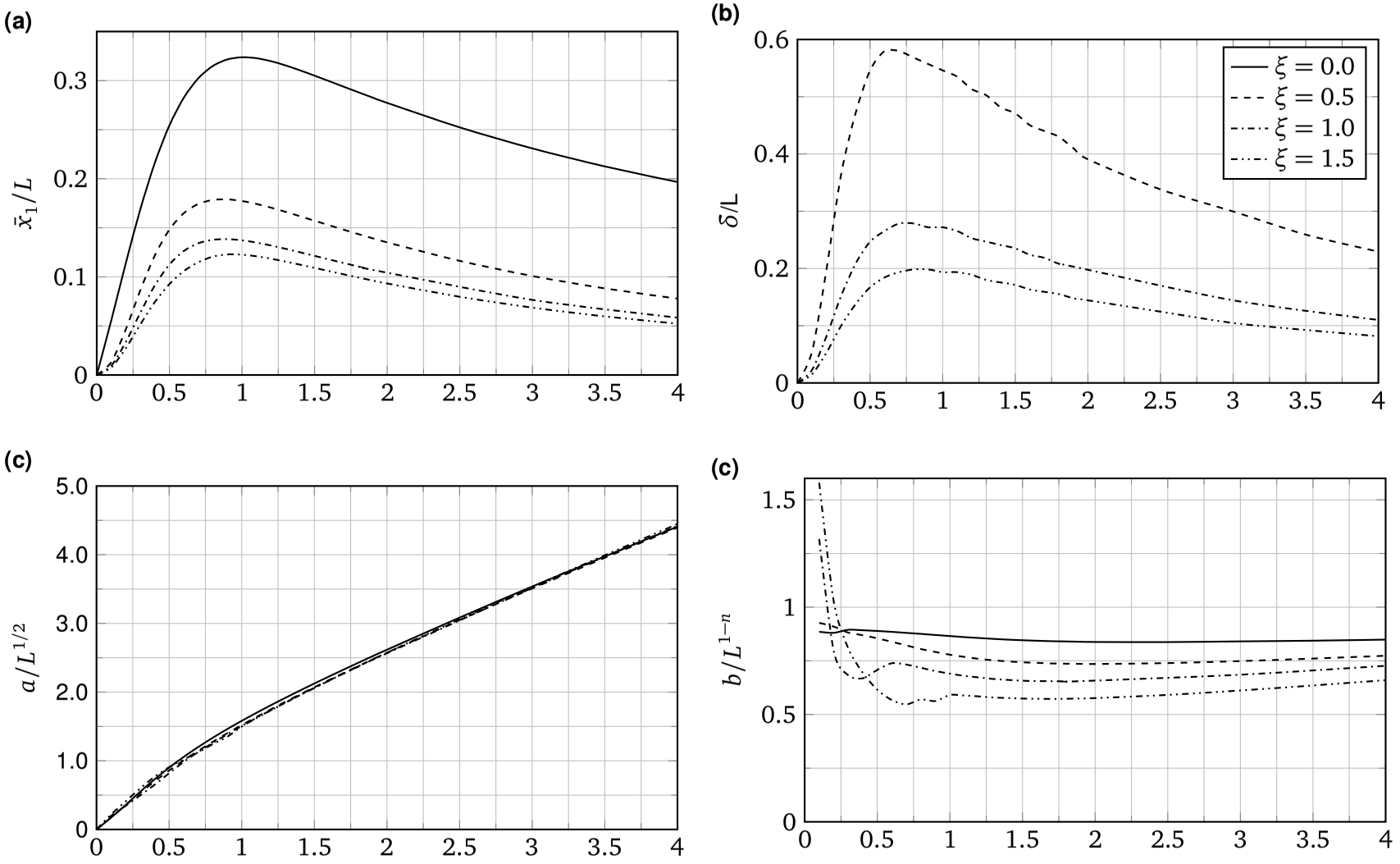

Figure 8.8: Effect of ξ on various parameters with nominal loading and $\beta = 7.83$.
(a) $\bar{x}_1/L$ vs. Δ_Y/L, (b) δ vs. Δ_Y/L, (c) a vs. Δ_Y/L, (d) b vs. Δ_Y/L.

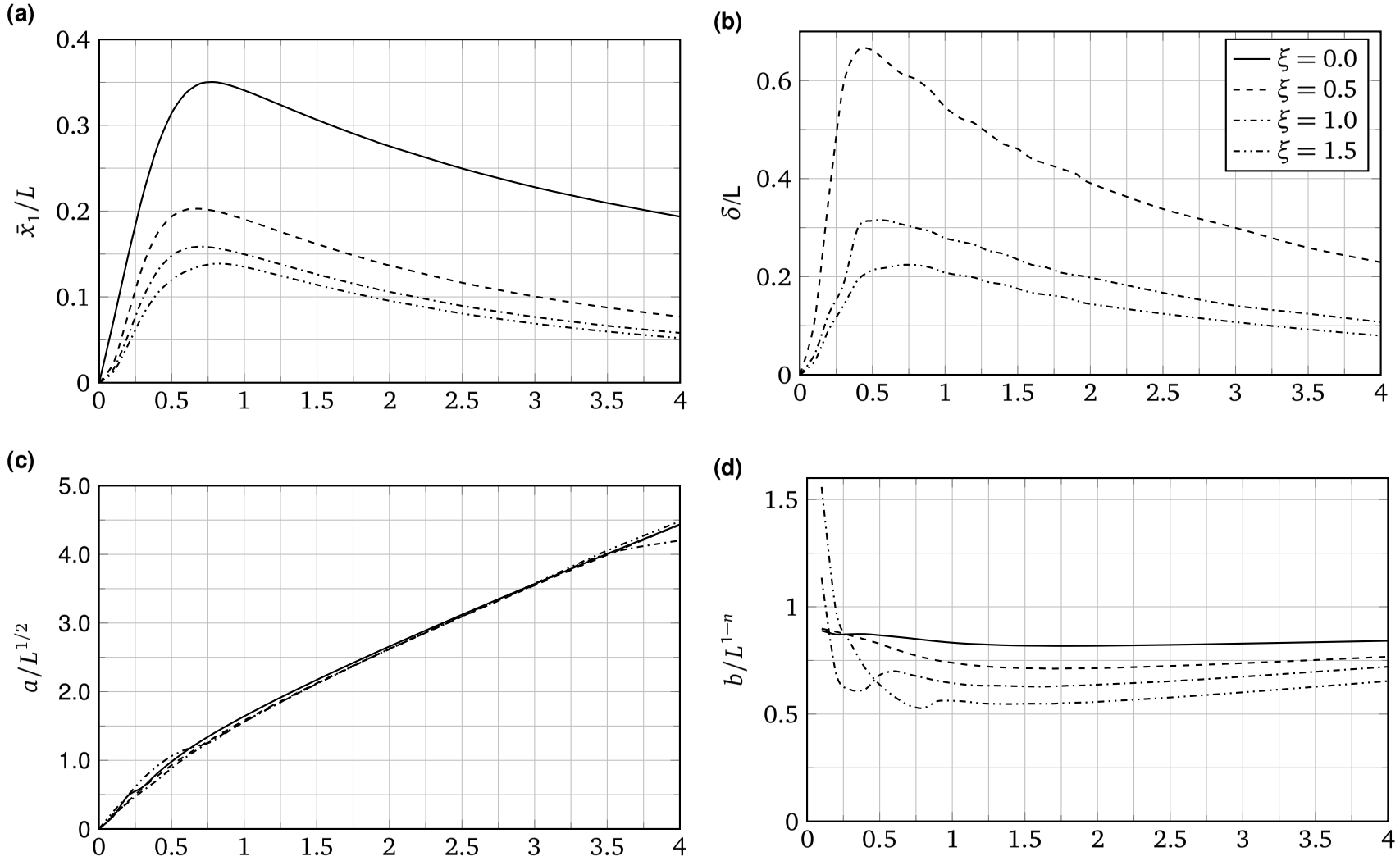

Figure 8.9: Effect of ξ on various parameters with nominal loading and $\beta = 16.0$.
(a) $\bar{x}_1/L$ vs. Δ_Y/L, (b) δ vs. Δ_Y/L, (c) a vs. Δ_Y/L, (d) b vs. Δ_Y/L.

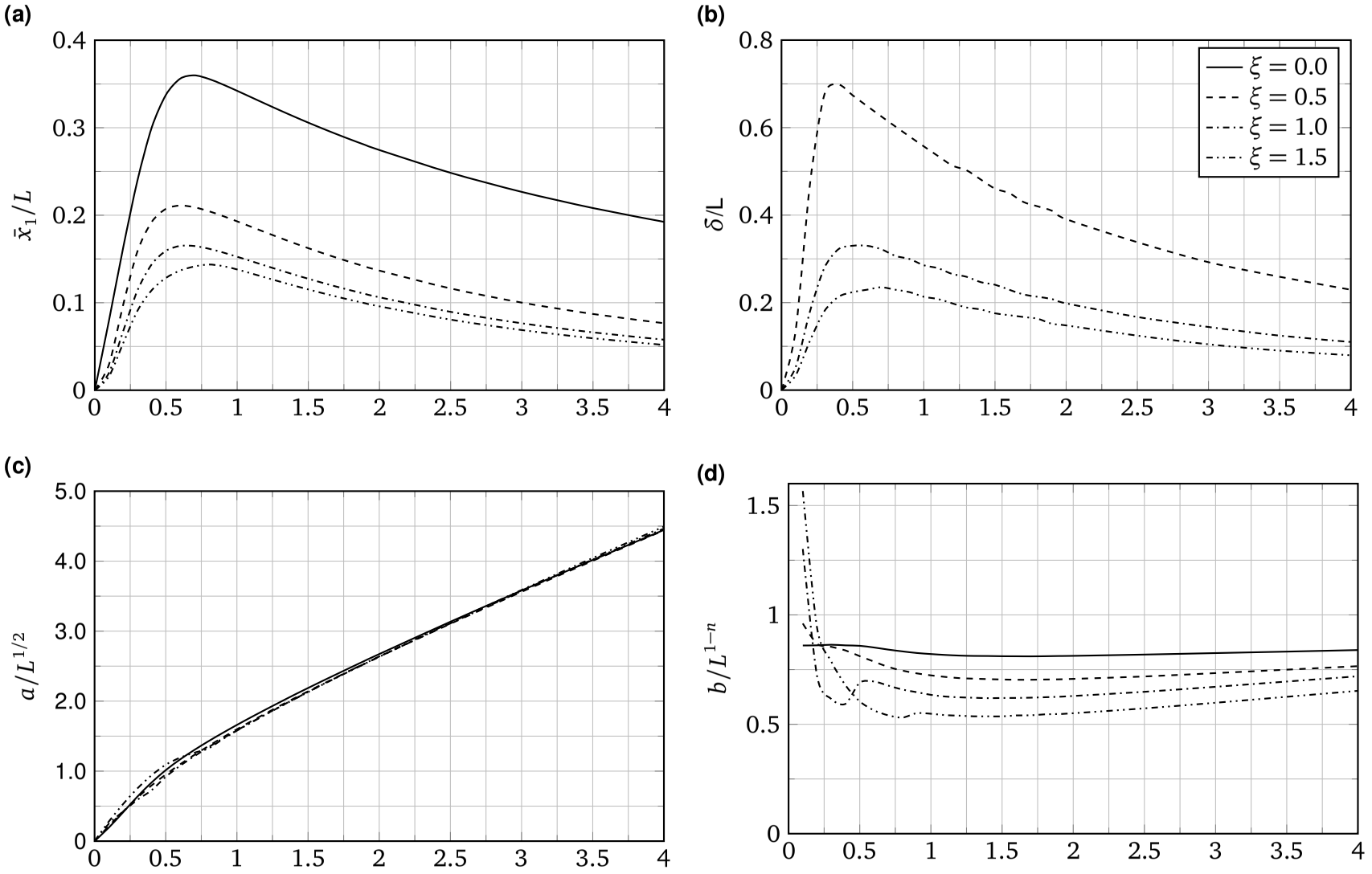

Figure 8.10: Effect of ξ on various parameters with nominal loading and $\beta = 24.50$.
(a) $\bar{x}_1/L$ vs. Δ_Y/L, (b) δ vs. Δ_Y/L, (c) a vs. Δ_Y/L, (d) b vs. Δ_Y/L.

8.3 Finite Friction With Lateral Loading

A series of FEA simulations were performed using various values of lateral loading displacement Δ_X. Each simulation required using a small, constant, normal displacement of $\Delta_Y = 0.1L$ in order to avoid distortion and self contact of the free edge. The lateral loading was varied through the range $-0.8L \leq \Delta_X \leq 0.7L$. Figure 8.11 shows these simulations using a compressibility parameter of $\beta = 16.0$ and a slip threshold magnitude of $|\sigma_{12}|/\mu \leq 0.5$. Recall that in order to determine the sign of ξ for each run, first a no-slip simulation was performed. From this, the direction of shear on the bonded surface was applied and the appropriate slip zone length was determined through the iterative method described in Section 8.1. In this example, the critical lateral loading (denoted by a vertical dashed line) where no-slippage occurs was determined to be $\Delta_c \simeq 0.3L$. As confirmation, this point falls precisely between the two plots (the average of the $\beta = 7.83$ and $\beta = 24.5$ runs) in Figure 7.6c where $\Delta_Y = 0.1L$.

From Figure 8.11a, we see that as lateral loading is increased from $\Delta_X = -0.3L$, the crack tip displacement $\bar{x}_1$ grows more than a linear slope with Δ_X. When the lateral loading magnitude was increased to the left so that $\Delta_X < -0.3L$, a similar trend occurred but the crack tip moving to the left making $\bar{x}_1 < 0$. Also, we see that with loading angles $\alpha < \tilde{\alpha}$ (or $\Delta_X < \Delta_c$ for a corresponding Δ_Y) the magnitude of the crack tip displacement $|\bar{x}_1|$ increases much more for the same $|\Delta_X|$ than when $\alpha > \tilde{\alpha}$. The effect of lateral loading on the slip zone length δ is shown in Figure 8.11b which also shows an increase in both directions from the critical lateral loading $\Delta_X = -0.3L$.

Figures 8.11c and 8.11d show the effect of lateral loading on the constants a and b respectively. When lateral loading Δ_X increases we find that the constant a decreases and tends to transition smoothly through the critical lateral loading $\Delta_X = -0.3L$, meaning the points on the left and right of the dashed vertical line tend to line up. This implies that in both positive and negative shear traction, as the lateral loading Δ_X increases the displacement

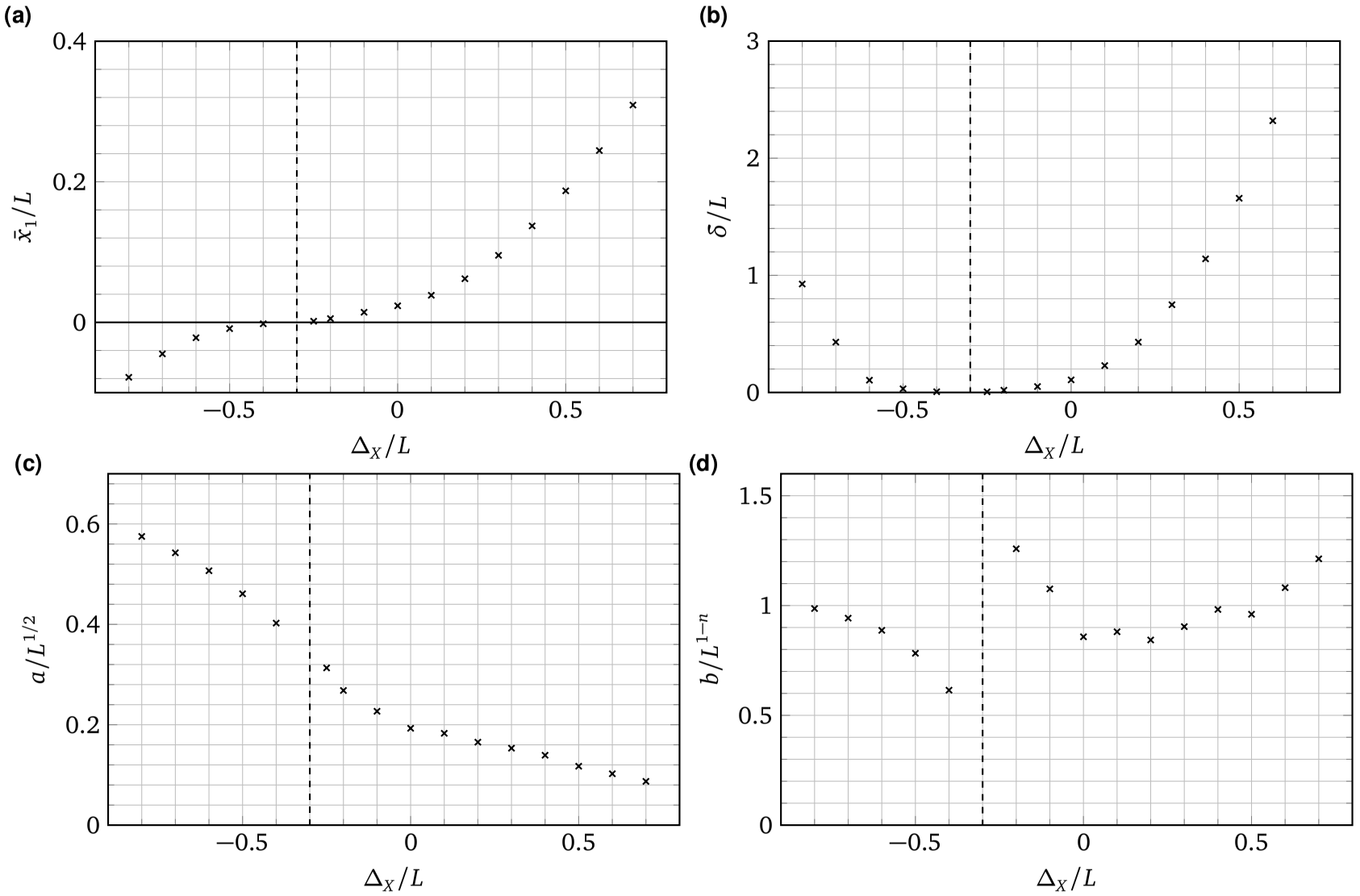

Figure 8.11: Effect of problem parameters versus lateral loading Δ_X. (a) Crack Tip Displacement $\bar{x}_1$, (b) Slip Zone Length δ, (c) x_2 Constant a, (d) x_1 Constant b.

in the x_2 direction is reduced. The constant b does not transition smoothly through the critical lateral loading point, however appears to remain constant either direction away from $\Delta_X = -0.3L$. It is not understood at this time why b shows such deviations near the critical lateral loading point, however one possibility is that since the slip zone length δ is very small near this point, reducing the range of validity in the solution from Eqns. (4.28).

Insight into the differences when lateral loading Δ_X is above and below the critical lateral loading Δ_c can be found by reviewing the shear stress along the entire bonded surface. For example, using the same data set from Figure 8.11, the shear stresses are shown in Figure 8.12. When $\Delta_X < \Delta_c$ (Figure 8.12a), negative shear is imposed all the way across the bonded surface resulting in the slip zone length δ growing rapidly once the average imposed shear stress increases above (or in the negative case, decreases) the threshold limit value of $\tau/\mu = -0.5$, then slippage is imposed over the entire surface. Correspondingly, by plotting the shear stress σ_{12} for the last several data points when $\Delta_X > \Delta_c$ (shown in Figure 8.12b) we see that the slip zone length δ increases marginally. As the lateral loading is increased further, it is not expected to suddenly slip across the entire surface like the cases when $\xi < 0$. Clearly, we have two distinct failure modes and responses to increasing load when the load angle α is less than or greater than the transition angle $\tilde{\alpha}$.

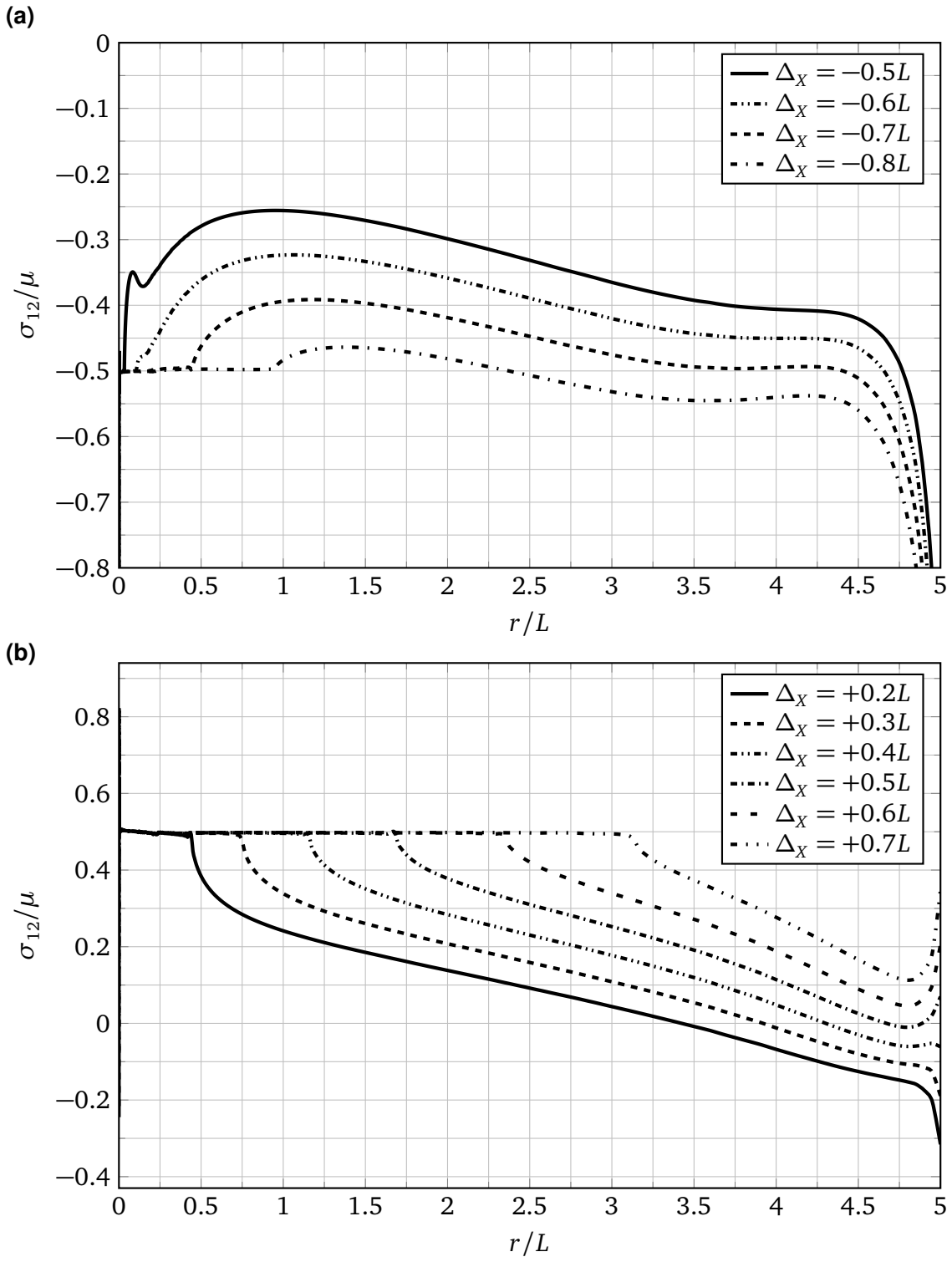

Figure 8.12: Example of shear imposed on the bonded surface at lateral displacements Δ_X, with a stress threshold $|\tau|/\mu = 0.5$. (a) $\Delta_X < \Delta_c$ (b) $\Delta_X > \Delta_c$.

Part IV

Discussion and Results

9 - A Finite Friction Tearing Mechanism

9.1 Interpretation of Experimental Results

The peel tests by Newby et al [7] highlighted the unexplained result that when adhesive tape is peeled away from a substrate at low pull angles (loosely interpreted as small loading angles, α), the bonds with higher adhesion energy slipped more but broke free of the surface with less pull force. With the idea that energy is dissipated through interfacial slippage, this lower slip resistance requiring higher peel forces [8, 9, 12, 13, 14, 15, 16, 11] is clearly not always shown to be the case. Partly, the results from this work can explain this. Consider the stress fields from Eqns. (4.36), which have the asymptotic order as $r \to 0$:

$$\sigma_{11} = \mathcal{O}\left(r^{\bar{n}-1/2}\right), \quad \sigma_{12} = \mathcal{O}(1), \quad \text{and} \quad \sigma_{22} = \mathcal{O}\left(r^{1/2-\bar{n}}\right),$$

where $\bar{n}$ is defined by Eqn. (4.27) as a function of the normalized interfacial slip threshold ξ so that

$$\bar{n}(\xi) = 1 + \frac{1}{\pi}\tan^{-1}\xi.$$

This implies that when $\xi > 0$ (a consequence of a loading angle α, depicted in each example of Figure 1.2), the normal stress σ_{22} increases in asymptotic order from the no slip case. So, as $\xi \to 0^+$, more slippage is allowed and we should see a reduction in the magnitude of the induced value of σ_{22}. This matches qualitatively with the idea that energy from slippage is traded from tearing to dissipate along the surface through slippage and resulting in blunting [15]. However, as discussed in Section 7.2 when the loading direction has a lower angle than the transition angle ($\alpha < \tilde{\alpha}$), then $\xi < 0$ and we find that σ_{22} shows a lower asymptotic order as $r \to 0$ than the no-slip case. In this realm, with increased slippage (and higher adhesion energy [7]), then as $\xi \to 0^-$, we see an increase in the magnitude of σ_{22}. Hence, it is a logical hypothesis that the reason Newby et al found stronger bonding with higher interfacial friction is a result of the peeling direction and the stress state at low loading angles ($\alpha < \tilde{\alpha}$).

To further demonstrate this hypothesis, consider two more examples. First, Figure 9.1 shows several runs together all in the range where $\xi \to 0^+$. Figure 9.1a shows this transition effect on the imposed shear σ_{12} on the bonded surface from the no-slip to frictionless cases. In each case we see the expected result and a growing slip zone length δ as the stress threshold $|\xi|$ is reduced. The corresponding deflected shapes of the free edge for each case are shown in Figure 9.1b and as the slip threshold ξ is lowered, the crack tip moves from the origin progressively to the right. In each case with finite friction, we see a vertical wedge angle ϕ, however a transition from the no-slip case to finite friction is not apparent; recall the discussion in Section 5.2 where this difficulty is explained by the analytical limit of our solution from Eqn. (4.12). We can further see this disconnect from no-slip to finite friction in Figure 9.1c where the corresponding normal stresses σ_{22} are shown. In this plot, we see that from the no-slip condition the normal stress σ_{22} on the bonded interface abruptly jumps with finite friction and is then progressively lowered when the slip threshold magnitude decreases (i.e. as $\xi \to 0^+$).

In the second example, shown in Figure 9.2a, we see that when loaded in the opposite

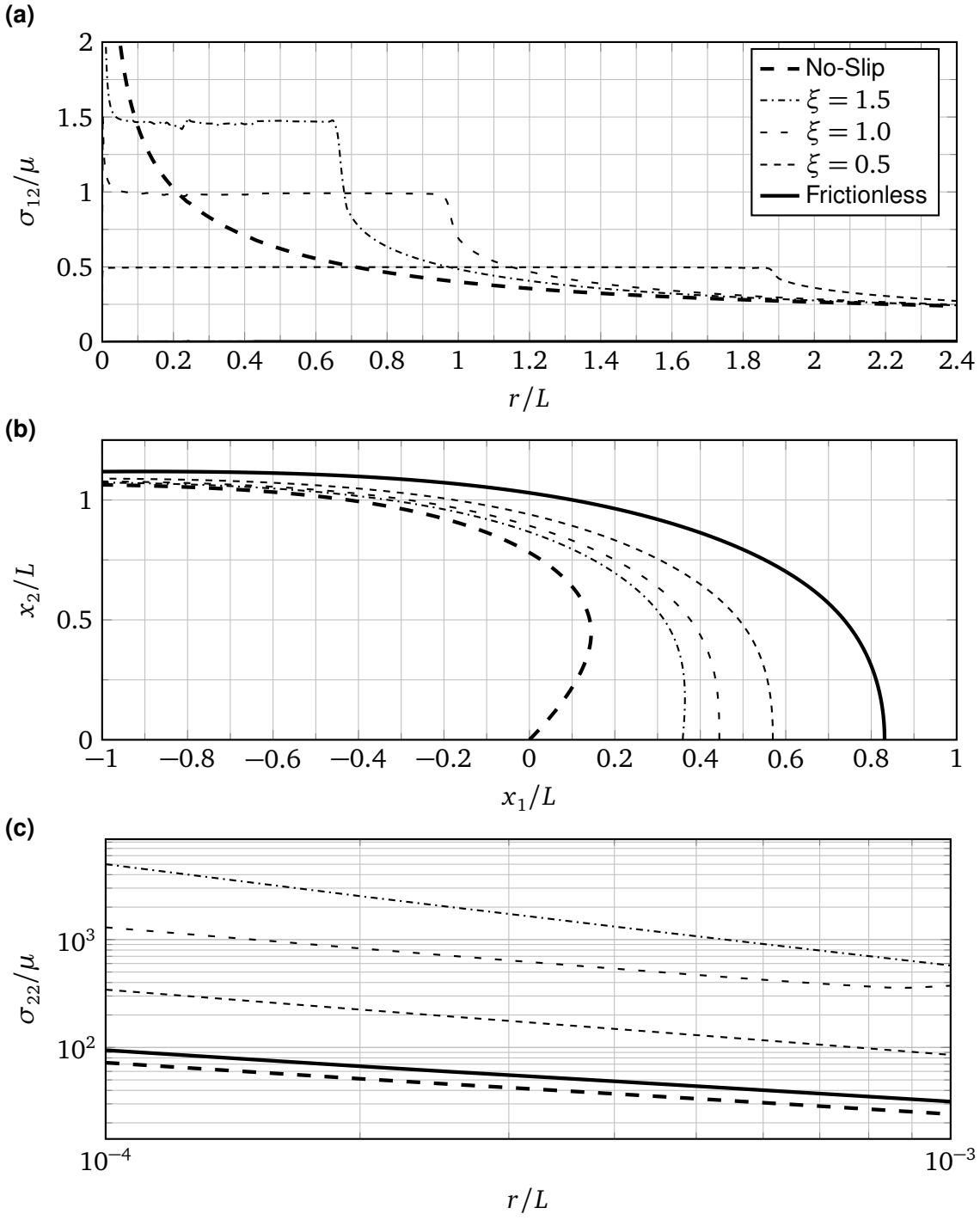

Figure 9.1: Loading example with $\Delta_Y = 1.0$, $\Delta_X = 0.5$, $\beta = 16.00$ and various ξ. (a) σ_{12}, (b) Crack opening shape, (c) σ_{22}.

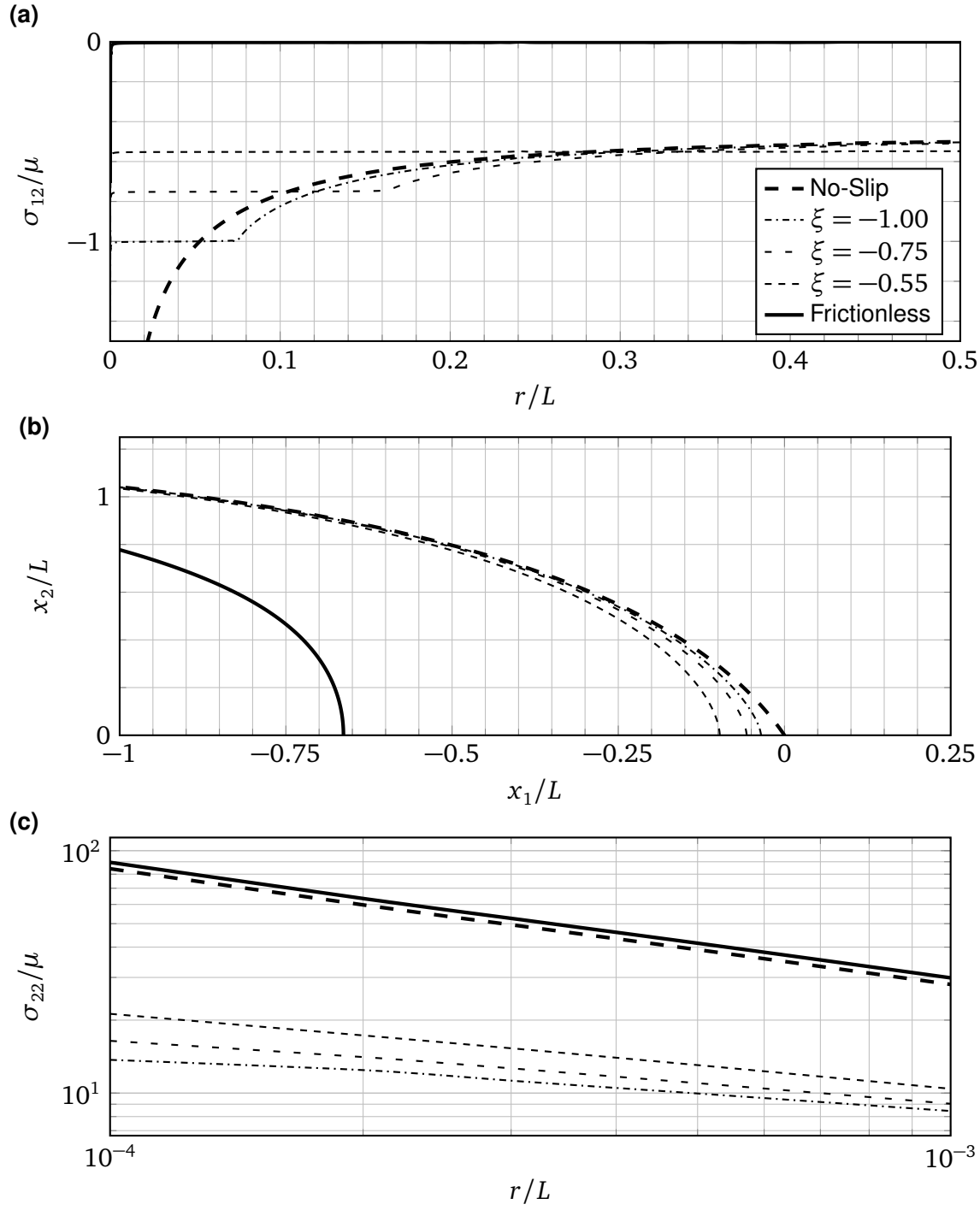

Figure 9.2: Effect of reducing shear threshold ξ with $\Delta_X = 1.0$, $\Delta_Y = -1.0$ and $\beta = 7.83$. (a) σ_{12} vs. r, (b) Deformed Shape, (c) σ_{22} vs r.

direction ($\alpha < \tilde{\alpha}$), as the slip threshold is reduced ($\xi \to 0^-$) the slip zone length δ again increases. In Figure 9.2b, the no-slip case shows a sharpened wedge angle on the free edge ($\phi > \pi/2$) and while the transition to the vertical wedge angle is still not apparent, the transition moves smoothly to the left as ξ is reduced. In this direction there is a large shift in surface slippage below $\xi < 0.55$ which can be attributed to the fact that the slip zone length increases much faster due to the negative overall stress across the surface (recall the discussion of Figure 8.12 from Section 8.3). When $\xi < 0$, the normal stresses σ_{22} on the bonded edge abruptly decreases when transitioning from no-slip to finite friction, and as the surface slip threshold is further lowered (or as slippage is allowed), the normal stress σ_{22} imposed on the bonded interface increases.

Another recent experimental work was done by Bhuyan et al [3]. In this study, a type of normal loading experiment called the 'sticky wedge test' was used, where a long strip of incompressible adhesive material with thickness of approximately $100 \pm 15\mu m$ was slowly lifted from a rigid substrate. In one of the figures presented, a scaled binary plot was provided to highlight the shape of the free edge near the crack tip with a vertical displacement of approximately $60\mu m$. Using Matlab data processing tools, data was extracted from this binary plot (see Figure 9.3a) and scaled using the a characteristic length of $H = 100\mu m$ as specified by Bhuyan et al. With the assumption that this experiment can be modeled similarly to either of the two bonded joints in Figures 1.2b and 1.2c, and further assuming the bonded elastomer tested by Bhuyan et al can be modeled as a 'nearly incompressible' Neo-Hookean material, then the near field solutions from Table 4.3 should apply, and with this data a least squares fit can be done for the parameters $\hat{b}$ and $\bar{n}$ in Eqn. (6.5). Starting with the points closest to the tip of the crack and by maximizing the points used such that $R^2 > 0.99$ (see the log plot in Figure 9.3b), it was found that $\hat{b} \simeq 1.5357 L^{-1.32}$ and $\bar{n} \simeq 1.161$, hence $\xi \simeq 0.552$. For comparison, Figure 9.3c shows the extracted data plotted with the curve fit and given that $\bar{n} > 1$ we see the opening geometry in this example is strikingly similar to a blunted parabola

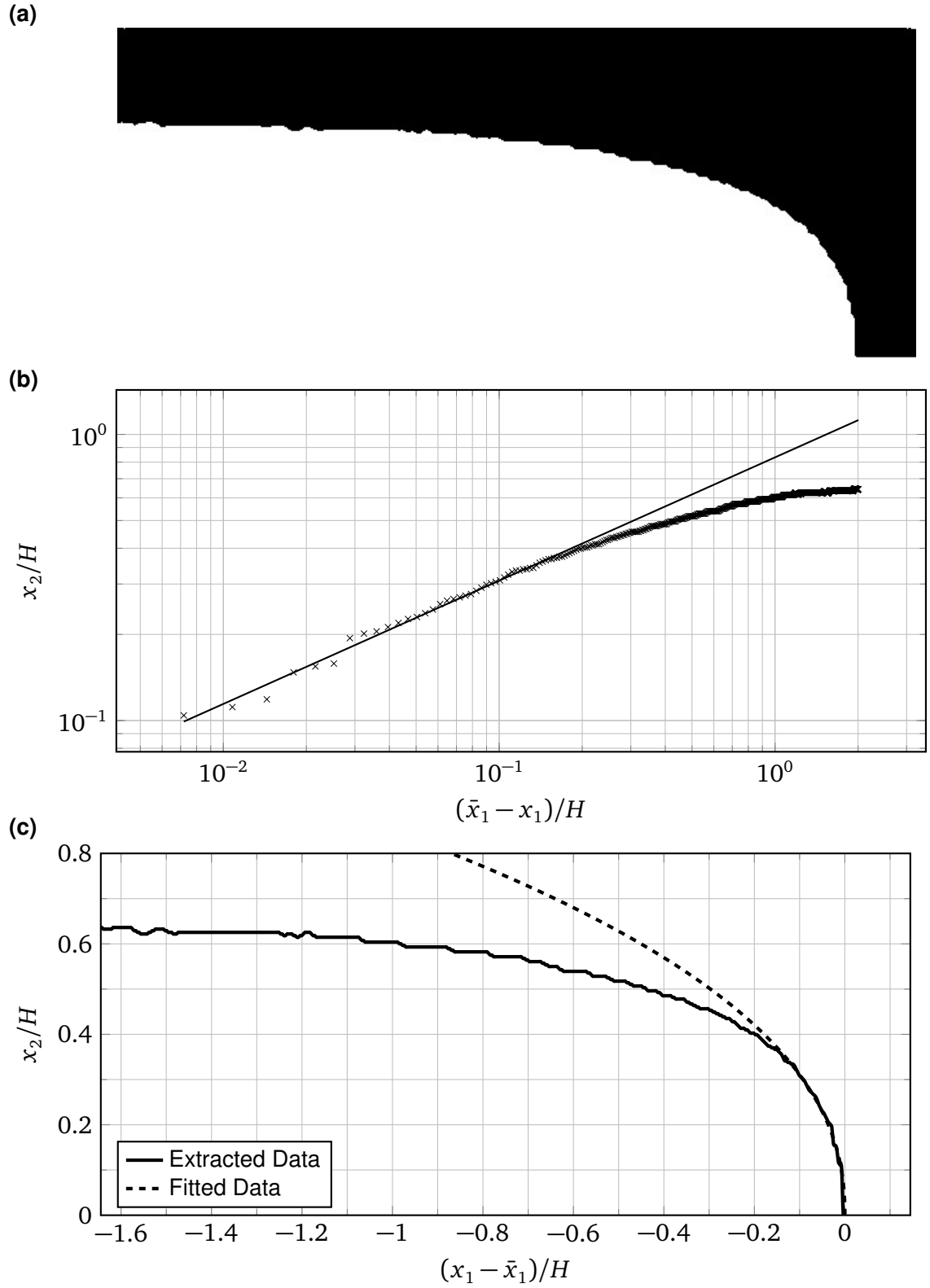

Figure 9.3: Curve fit of data compiled by Bhuyan et al. [3] to estimate ξ (a) Extracted data from Bhuyan et al [3] (b) Curve fit of extracted data, (c) Free edge shape plotted with fitted solution.

and more resembles the shape in Figure 5.2b than either of the two extents in Figures 5.2a or 5.2c, which were both determined to have a parabolic near-field shape [1] near $r \to 0$.

Note that the measurement process used here with Bhuyan et al's data to determine the slip threshold ξ (and $\bar{n}$) is provided as an example. In order to use this technique experimentally, it is also recommended to provide a measurement for the crack tip displacement $\bar{x}_1$ and slip zone length δ along with measurements of displacement along the the slip zone. With this additional data, direct comparisons could be made with the normal loading study from Section 8.2 such that the friction threshold ξ could be read directly (or interpolated) from any one of Figures 8.8a, 8.8b, 8.9a, 8.9b, 8.10a, or 8.10b.

9.2 The Transition from No-Slip to Finite Friction

In every case, when applying the sticky-wedge test, Bhuyan et al observed a near vertical wedge angle ($\phi \simeq \pi/2$) [3]. However, they also noted that the wedge angle may depend on material parameters such as viscoelasticity, and in these cases softer materials with less cross-linking deviated more from a vertical wedge angle (like what Newby saw) while the stiffer materials (larger μ) remain more like the perpendicular wedge angle and suggest that the wedge angle may be more finite at smaller than measured scales. We find insight into the phenomena of a finite wedge angle ϕ with interfacial slippage (unfortunately, not something shown in the model derived in this manuscript) by considering experiments in debonding of soft elastomers by Liechti et al [66], where a wedge angle $\phi \simeq \pi/2$ was found at slow strain rates, and a correlation was observed where the wedge angle ϕ decreased from $\pi/2$ as the strain rate increased.

Given these experimental findings at slow tearing, it is proposed that the elastostatic model from this study is viable in these cases. However, due to the viscoelastic nature of the soft elastomers tested (a characteristic not incorporated in the model presented here), the finger tip indent due to a finite wedge angle is also a velocity dependent result. So, as load

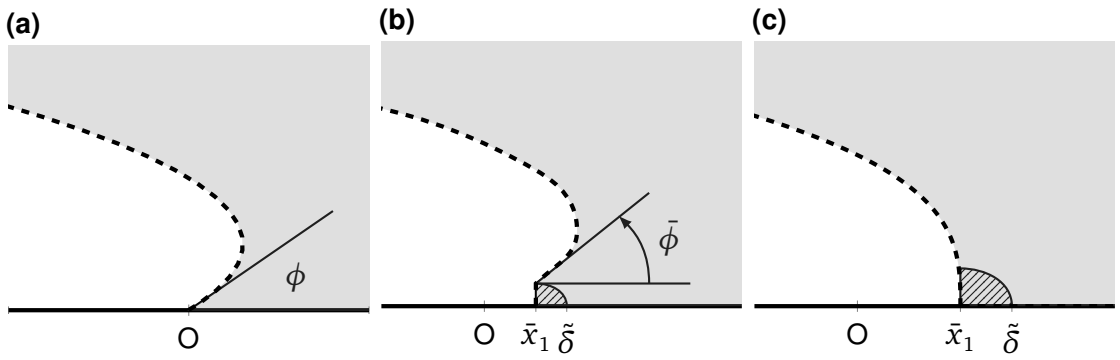

Figure 9.4: Visualization of the transition from no-slip to finite friction. (a) No-slip (b) Partial transition (c) finite friction.

speed increases, there will be a deviation from the results shown here which result in stiffer material and potentially larger ξ. In short, the results here are from a static case and therefore represent an equilibrium result only. A proposed idea is that the slip zone can grow radially resulting in a transition between the no-slip case in Figure 9.4a and the finite friction case from Figure 9.4c. A visualization of this is shown by Figure 9.4b, where $\bar{\phi}$ is an adjusted wedge angle at the edge of the slip zone. In these figures, the hatched pattern represents a growing slip zone in the deformed configuration (denoted $\tilde{\delta}$) that may have velocity dependence, or something similar to viscoelastic effects on the interfacial layer itself. This is a reasonable conclusion because the imposed stress threshold τ (and ξ) always acts in an opposing way to displacement. This is similar to coulomb friction which has analogies to a linear dash-pot in dynamic systems [103, 104, 105], then the finite friction boundary condition should be function of loading speed with a dissipative effect like viscoelasticity.

Given the range found for validity of the solution (Eqn. (4.12)), it is implied that our findings can not work for large values of slip threshold ξ. However, Newby et al proposed a model for interfacial slip in the form [7]

$$\tan\bar{\phi} = \frac{2\xi}{\xi^2 - 1}. \tag{9.1}$$

Using Newby's proposed model shown in Eqn. (9.1) with small values of ξ we find

$$\tan\bar{\phi} \simeq \lim_{\xi\to 0} \frac{2\xi}{\xi^2 - 1} = 0, \qquad \Longrightarrow \quad \therefore \bar{\phi} \simeq 0,$$

which does not agree at all with the vertical slope found in the finite friction result in Eqn. (5.22). However, for very large values of interfacial slip threshold our results are only viable inside a small slip zone (such as the small shaded region in Figure 9.4b) and it is expected that the solution should not deviate much from the no-slip solution, summarized by Table 4.2. Using Newby's result and recalling Eqn. (5.3), the wedge angle $\bar{\phi}$ can be approximated at $r = \delta$ by

$$\tan\bar{\phi} = \lim_{\substack{r\to\delta \\ \theta\to\pi}} \frac{dx_2}{dx_1} \simeq \frac{a_2}{a_1 - 2\delta^{1/2}} = \frac{a_2}{a_1}\left[\frac{1}{1 - \left(\frac{1}{2}a_1\delta^{-1/2}\right)^{-1}}\right].$$

Using the shear stress result from the no-slip case on the bonded edge ($\theta = 0$) from Eqn. (4.24b) and with a very small slip zone, then

$$\sigma_{12}(\delta, 0) \simeq \tfrac{1}{2}\mu a_1 \delta^{-1/2}.$$

Hence, we have an approximation for δ versus ξ by rearranging to get

$$\xi = \tau/\mu \simeq \tfrac{1}{2}a_1\delta^{-1/2}. \tag{9.2}$$

Also recall the no-slip wedge angle is defined as ϕ where

$$\tan\phi \equiv \frac{a_1}{a_2},$$

then using Eqn. (9.2), the adjusted wedge angle becomes

$$\tan\bar{\phi} \simeq \left[\frac{1}{1-\xi^{-1}}\right]\tan\phi. \tag{9.3}$$

For large values of $\xi >> 1$, then $\xi^{-1} << 1$ and the first term in Eqn. (9.3) has a Maclaurin series [90] expansion

$$\frac{1}{1-\xi^{-1}} = \sum_{N=0}^{\infty}\left(\frac{1}{\xi}\right)^{N} \simeq 1+\frac{1}{\xi}, \tag{9.4}$$

and finally we arrive at

$$\tan\bar{\phi} \simeq \left[1+\frac{1}{\xi}\right]\tan\phi. \tag{9.5}$$

Recall that the expression $\tan\phi$ (the slope of the no-slip wedge angle) was determined by the far field loading conditions and is the ratio of the no-slip stresses from Eqn. (5.4). The expression in Eqn. (9.5) shows how the wedge angle with minimal interfacial slippage $\bar{\phi}$ may transition from the no-slip case (with $\xi \to \infty$) to the finite friction case for large ξ. In this case, we assume a range beyond that shown by Eqn. (4.30) for compressible materials where

$$\tan\left[\frac{\pi}{2}\left(\frac{\beta}{\beta+1}\right)\right] > \xi > \infty.$$

A final note with this transition. If the material is incompressible, then $\beta \to \infty$ and this range of ξ shrinks to zero and the analytical result in Eqn. (4.28) is viable, implying that the model from Eqn. (9.5) does not apply, or represents another possible branch of solution.

9.3 Other Design Considerations From This Study

While the results here show how interfacial friction can dramatically affect the stress state and the delamination mechanism of bonded elastomers, there are multiple other aspects worth considering when designing a bonded interface. How to use the results depend on what is

desired from the bonded joint. This section is a highlight of some considerations for design, and focus mainly on the desired type of failure mode in the bonded joint.

The direction of loading α in conjunction with the transition angle $\tilde{\alpha}$ (which is a function of total stretch Δ) can significantly change the stress state near the crack tip. Assuming a high slip threshold τ, the bonded joint will be significantly stronger if the loading is more tangential to the bond. To visualize this, compare the magnitudes of normal stress σ_{22} from Figures 9.1c and 9.2c. Given this, a lap joint shown in Figure 1.2c where the two adherands are pulled apart in the $\pm\hat{\mathbf{E}}_1$ directions would be recommended. However, if failure at a particular lower strength is desired then a lower slip threshold τ can be achieved by adding various lubricants on the bonded surface before bonding [7].

The transition angle $\tilde{\alpha}$ findings in Figure 7.6b show that more flexible materials (for example rubbery elastomers with less polymer cross-linking), the transition angle α is somewhere close to pure normal loading ($\alpha \simeq \pi/2$). Conversely, for more brittle elastomers that can not undergo a large amount of stretch before delamination, the transition angle $\tilde{\alpha}$ is much smaller. Depending on how ductile the adhesive is and the desired result, it is recommended to either keep the loading angle well below ($\alpha < \tilde{\alpha}$) or above ($\alpha > \tilde{\alpha}$) the transition angle $\tilde{\alpha}$.

Also, consider the scaling model from Eqn. (9.5) for large interfacial slip thresholds (adjusted slightly from the no-slip case) was linked to the effects found in the FEA study shown in Figures 7.3 and 7.4. Note that the wedge angle ϕ increases from zero with small stretch to $\phi \simeq \pi/2$ with large stretch. It was shown analytically by Eqns. (5.7) and (5.17) (on the bonded and free edges respectively) that this wedge angle is also found to be related to the stresses. From this, we see that as the material stretches, the dominance of the stresses transitions from $\sigma_{11} > \sigma_{12} > \sigma_{22}$ to the opposite state $\sigma_{22} > \sigma_{12} > \sigma_{11}$.

10 - Conclusions and Future Work

10.1 Conclusions

In this work, several bond types were generalized as a near field interface crack problem (shown in Figure 3.1). Near field solutions were found for all three friction cases and are summarized in Tables 4.1, 4.2 and 4.3. From these closed form solutions, it was confirmed that the frictionless case is related to the finite friction case when slip threshold τ is set to zero.

The near-field solutions for the no-slip case produced a tidy expression between the ratio of various plane strain Cauchy stress $\boldsymbol{\sigma}$ components. However, a small boundary layer adjustment (discussed in Chapter 5) was required for evaluation of stresses on the free edge. Assuming a finite (non vertical slope) wedge angle ϕ, then the stress ratios for the no-slip case are

$$\begin{aligned}
&\text{Bonded Edge} \quad (\theta = 0): && \frac{\sigma_{22}}{\sigma_{11}} \simeq \tan^2\phi \quad \text{and} \quad \frac{\sigma_{12}}{\sigma_{11}} \simeq \tan\phi, \\
&\text{Free Edge} \quad (\theta = \pi): && \frac{\sigma_{22}}{\sigma_{11}} \simeq \sec^2\phi \quad \text{and} \quad \frac{\sigma_{12}}{\sigma_{11}} \simeq \tan\phi.
\end{aligned}$$

The no-slip and finite friction near-field solutions, which have remaining arbitrary constants,

were validated to show the same solutions near the points of interest as the extensive numerical study from Part III. The stress fields in both no-slip and finite friction cases also showed agreement with the numerical results. From the numerical studies, the relationship between normal deflection loading Δ_Y and the wedge angle ϕ was compared and it was concluded that for fixed loading values of Δ_Y and large values of β (the material compressibility parameter), the no-slip wedge angle saturates to a constant value. While normal loading Δ_Y was increased, the no-slip wedge angle increased toward the vertical angle $\phi \to \pi/2$. It is then concluded that the dominant stress depends on the amount of far field loading (material stretch) and is related to the wedge angle ϕ.

When lateral loading was introduced, it was found at particular loading directions (when $\alpha = \tilde{\alpha}$) that the no-slip shear stress imposed on the bonded surface was zero. When deviating from this transition angle $\tilde{\alpha}$, the sign of the shear stress σ_{12} also changed.

With a validated numerical method for iteratively quantifying the slip zone length δ, the finite friction case showed a vertical wedge angle for every simulation described in this manuscript and it was found that the product of the normal stresses has a constant value, being

$$\sigma_{11}\sigma_{22} = \tau^2 + \mu^2, \qquad \text{in the range} \quad 0 \leq \theta < \pi.$$

The finite friction solutions also revealed that the asymptotic order of the deflection and stress fields were functions of the bonded stress threshold τ. Even more interesting was that two different stress states exist depending on whether $\sigma_{12} < 0$ or $\sigma_{12} > 0$ on the bonded edge - which is linked to the load angle α with respect to the transition loading angle $\tilde{\alpha}$. Notably, the normal stress $\sigma_{22} = \mathcal{O}\left(r^{1/2-\bar{n}}\right)$ where

$$\bar{n} = 1 + \frac{1}{\pi}\tan^{-1}\left(\frac{\tau}{\mu}\right),$$

from which we can conclude that bonded interfaces loaded at shallow angles ($\alpha < \tilde{\alpha}$) with more interfacial slip (i.e. a lower slip threshold τ) will indeed show a higher imposed normal stress leading to detachment which partially may explain Newby et al's previously experimental result [7].

Unfortunately, Newby et al also showed experimentally that there tended to be a wedge angle $\phi < \pi/2$ with interfacial slippage to the right ($\bar{x}_1 > 0$) at shallow loading angles ($\alpha < \tilde{\alpha}$). While the stress state mentioned above may explain the delamination as an increase the normal stress σ_{22}, the results for material deflection presented in this manuscript showed a vertical wedge angle $\phi = \pi/2$ with material deflected to the left. Also of note is that the formulations examined here were elastostatic in nature and did not take into account viscoelasticity, which may also explain why a finite wedge angle ($\phi \neq \pi/2$) was not shown in any finite friction solutions or FEA simulations. It is concluded that the near-field solutions are merely the equilibrium case after any dissipation in the bulk elastomer or on the bonded surface has occurred.

Given that the finite slip solution had a range of validity where

$$-\infty < \frac{\tau}{\mu} < \tan\left[\frac{\pi}{2}\left(\frac{\beta}{\beta+1}\right)\right],$$

then solutions for values of β and ξ outside this range are not shown with this model and other forms of solution may exist. Considering the case when τ is very large, utilizing the scaling model by Newby et al [7] with the no-slip result from Eqns. (4.21) a proposed transition between no-slip and finite friction was presented in Section 9.2 with in the form

$$\tan\bar{\phi} \simeq \left(1 + \frac{\mu}{\tau}\right)\tan\phi, \quad \text{for} \quad \tau >> \mu,$$

where $\bar{\phi}$ is an adjusted wedge angle at the edge of a small slip zone length $r = \delta$.

10.2 Proposed Future Work

Future problems of interest are listed here. All of the problems shown in the following sections are appropriate extensions from the findings in this dissertation.

10.2.1 Finite Friction with Incompressible Elastomers

For the special case of material incompressibility, then the volumes in the reference and spatial configurations (V_0 and V respectively) are equivalent, hence $J = 1$ from Eqn. (2.3) and the strain energy density function collapses to a function with only one invariant in plane strain:

$$\psi(I_1, I_2, I_3) = \hat{\mathcal{W}}(I). \tag{10.1}$$

However in this case, a Lagrange multiplier [40] is required so that

$$\psi(I_1, I_2, I_3) = \hat{\mathcal{W}}(I) - (J-1)\,\tilde{\mathrm{p}}(\mathbf{X}),$$

where $\tilde{\mathrm{p}} = \tilde{\mathrm{p}}(r, \theta)$ is an arbitrary (and unknown) function that in incompressible elasticity problems is typically interpreted to be a pressure field [39, 40, 34]. Given that the function $\tilde{\mathrm{p}}(\mathbf{X})$ is an arbitrary result of incompressibility, then $J = 1$ from Eqn. (3.6b) which yields the constraint

$$\frac{1}{r}\left[\frac{\partial x_1}{\partial r}\frac{\partial x_2}{\partial \theta} - \frac{\partial x_1}{\partial \theta}\frac{\partial x_2}{\partial r}\right] = 1. \tag{10.2}$$

The first Piola-Kirchhoff stress tensor becomes:

$$\boldsymbol{\mathcal{P}} = 2\hat{\mathcal{W}}'(I)\boldsymbol{\mathcal{F}} - \tilde{\mathrm{p}}(\mathbf{X})\boldsymbol{\mathcal{F}}^{-T}. \tag{10.3}$$

Using Eqn. (2.25), the governing equations in the bulk material are

$$2\hat{\mathcal{W}}'(I)\nabla_{\mathrm{x}}^2 x_1 + 2\hat{\mathcal{W}}''(I)(\nabla_{\mathrm{x}} x_1 \cdot \nabla_{\mathrm{x}} I) - |\nabla_{\mathrm{x}}\tilde{\mathrm{p}}\times\nabla_{\mathrm{x}} x_2| = 0, \tag{10.4a}$$

$$\text{and} \quad 2\hat{\mathcal{W}}'(I)\nabla_{\mathrm{x}}^2 x_2 + 2\hat{\mathcal{W}}''(I)(\nabla_{\mathrm{x}} x_2 \cdot \nabla_{\mathrm{x}} I) + |\nabla_{\mathrm{x}}\tilde{\mathrm{p}}\times\nabla_{\mathrm{x}} x_1| = 0, \tag{10.4b}$$

where $(i = 1, 2)$

$$\nabla_{\mathrm{x}}^2 x_i \equiv \frac{\partial^2 x_i}{\partial r^2} + \frac{1}{r}\frac{\partial x_i}{\partial r} + \frac{1}{r^2}\frac{\partial^2 x_i}{\partial \theta^2}, \tag{10.5a}$$

$$\nabla_{\mathrm{x}} x_i \cdot \nabla_{\mathrm{x}} I \equiv \frac{\partial x_i}{\partial r}\frac{\partial I}{\partial r} + \frac{1}{r^2}\frac{\partial x_i}{\partial \theta}\frac{\partial I}{\partial \theta}, \tag{10.5b}$$

$$\text{and} \quad |\nabla_{\mathrm{x}}\tilde{\mathrm{p}}\times\nabla_{\mathrm{x}} x_i| \equiv \frac{1}{r}\left[\frac{\partial \tilde{\mathrm{p}}}{\partial r}\frac{\partial x_i}{\partial \theta} - \frac{\partial \tilde{\mathrm{p}}}{\partial \theta}\frac{\partial x_i}{\partial r}\right]. \tag{10.5c}$$

Recall the boundary condition on the traction free edge ($\theta = \pi$) requires $\mathcal{P}_{12}(r, \pi) = \mathcal{P}_{22}(r, \pi) = 0$. Then

$$2\hat{\mathcal{W}}'(I)\frac{1}{r}\frac{\partial x_1}{\partial \theta} + \tilde{\mathrm{p}}(\mathbf{X})\frac{\partial x_2}{\partial r} = 0, \tag{10.6a}$$

$$\text{and} \quad 2\hat{\mathcal{W}}'(I)\frac{1}{r}\frac{\partial x_2}{\partial \theta} - \tilde{\mathrm{p}}(\mathbf{X})\frac{\partial x_1}{\partial r} = 0. \tag{10.6b}$$

To determine the generalized form of the finite friction boundary condition on the bonded surface (at $\theta = 0$), Eqn. (2.18) applies, which re-arranged we find

$$\boldsymbol{\sigma} = \boldsymbol{\mathcal{P}}\boldsymbol{\mathcal{F}}^T = 2\hat{\mathcal{W}}'(I)\boldsymbol{\mathcal{F}}\boldsymbol{\mathcal{F}}^T - \tilde{\mathrm{p}}(\mathbf{X})\tilde{\mathbf{I}}, \tag{10.7}$$

where $\tilde{\mathbf{I}}$ is the identity tensor in the deformed basis. Using Eqn. (3.5) with $\theta = 0$ and assuming a constant shear $\sigma_{12}(r, 0) = \tau$, then

$$2\hat{\mathcal{W}}'(I)\left[\frac{1}{r}\frac{\partial x_1}{\partial \theta}\right]\left[\frac{1}{r}\frac{\partial x_2}{\partial \theta}\right] = \tau, \qquad \text{on} \quad \theta = 0. \tag{10.8}$$

Like the cases previously presented, no vertical opening is assumed, hence $x_2(r,0) = 0$. Therefore the constraint $J = 1$ requires

$$\frac{1}{r}\frac{\partial x_1}{\partial r}\frac{\partial x_2}{\partial \theta} = 1, \quad \text{on} \quad \theta = 0. \tag{10.9}$$

Combining this with Eqn. (10.8) and re-arranging we get a boundary condition for x_1 only,

$$2\hat{\mathcal{W}}'(I)\left[\frac{1}{r}\frac{\partial x_1}{\partial \theta}\right] - \tau\frac{\partial x_1}{\partial r} = 0, \qquad \text{on} \quad \theta = 0. \tag{10.10}$$

The general incompressible BVP is then made up of the governing Eqns. (10.4), the free end conditions (on $\theta = \pi$) by Eqns. (10.6), and the bonded boundary conditions (on $\theta = 0$) from Eqns. (3.10) and (10.10). Anecdotally, in the Neo-Hookean material case, then $\hat{\mathcal{W}}'(I) = \mu/2$ (recall Eqn. (3.16)) and the boundary condition from Eqn. (10.10) has the same form as the finite friction bonded condition using the compressible Blatz-Ko material (Eqn. (3.14)), being

$$\frac{1}{r}\frac{\partial x_1}{\partial \theta} - \left(\frac{\tau}{\mu}\right)\frac{\partial x_1}{\partial r} = 0, \quad \text{on} \quad \theta = 0. \tag{10.11}$$

While the incompressible no-slip case did not allow for a viable solution with separable functions of r and θ, the case with finite friction should be solvable using the same techniques from Chapter 4 and using some clever hints from Stephenson [80]. The value in pursuing this effort would be to confirm (or not) that the solution is the same as outlined in Table 4.3, i.e. that compressibility does not affect the geometry of the solution away from the free edge. Also, recall that the compressibility parameter β was found in the asymptotic order of the stress fields on the traction free edge ($\theta = \pi$) shown in Eqns. (5.24), which imply that as $\beta \to \infty$, then

$$\sigma_{11}(r,\pi) = \mathcal{O}\left(r^{2\bar{n}-2}\right), \quad \sigma_{12}(r,\pi) = \mathcal{O}\left(r^{\bar{n}-3/2}\right), \quad \text{and} \quad \sigma_{22}(r,\pi) = \mathcal{O}\left(r^{-1}\right).$$

Finally, consider some of the previously mentioned incompressible models utilizing a strain stiffening factor η. The generalized Neo-Hookean (GNH) model from Eqn. (3.15) has merit and would be a good starting point to understand how strain stiffening affects interfacial slippage. As another possible avenue to study strain stiffening effects, recall Stephenson's model [80] from Eqn. (3.19). Solving either of these problems with finite interfacial friction can yield direct comparisons using the general crack problem as the frictionless case.

10.2.2 Opening in Two Directions

To pursue crack opening in two directions there are many failure criteria which can be useful as boundary conditions, notably: Distortion Energy (von Mises), Maximum Shear Stress Theory ($\tau \geq \frac{1}{2}\sigma_Y$), and Maximum Principal Stress for Ductile Materials ($\sigma_{max} \geq \sigma_U$) [20]. To use these, the constraint boundary condition $x_2(r,0) = 0$ from Eqn. (3.10) would be replaced with a force balance. Consider the surface traction $\mathbf{t}$ on the bonded edge ($\theta = 0$) from Eqn. (2.14), then the surface traction is

$$\mathbf{t}(r,0) = \left[\sigma_{ij}(r,0)\hat{\mathbf{e}}_i \otimes \hat{\mathbf{e}}_j\right][-\hat{\mathbf{e}}_2] = -[\sigma_{11}(r,0)\hat{\mathbf{e}}_1 + \sigma_{12}(r,0)\hat{\mathbf{e}}_2],$$

and $\hat{\mathbf{e}}_1$ and $\hat{\mathbf{e}}_2$ terms refer to the directions in the spatial configuration. The total stress t on the surface is

$$t \equiv |\mathbf{t}| = \sqrt{\sigma_{11}^2(r,0) + \sigma_{12}^2(r,0)}, \tag{10.12}$$

from which any of the stress failure criteria mentioned above can be utilized.

Another method is to impose a traction separation relation for both normal and lateral directions as done with the finite friction case explained in Section 3.2. Consider the surface traction $\mathbf{t}$ on the bonded edge ($\theta = 0$) from Eqn. (2.14), then the surface traction normal to the bottom edge is σ_{22}, hence the finite friction boundary condition for the bonded surface

with opening in normal and lateral directions is

$$|\sigma_{12}(r,0)| \leq |\tau|, \quad \text{and} \quad |\sigma_{22}(r,0)| \leq |\sigma|, \tag{10.13}$$

where τ and σ are stress thresholds in the x_1 and x_2 directions respectively. Again, a caution doing this because Park and Paulino explained that traction separation relationships may not be independent directionally, and the model presented above does not account for this if τ and σ are constants.

Given that it is shown throughout this manuscript that interfacial slippage, a traction separation model in the lateral direction, has a significant effect on bonding strength; and also considering that the most common analysis in fracture is done using normal traction separation models, then it must be concluded that both directions account for fracture. It would then be of interest to utilize a traction-separation model that takes into account of both separation directions which can be modeled and tested.

10.2.3 Utilize Other Cohesive Zone Models as Boundary Conditions

Many cohesive zone models can be sought from Park and Paulino's review [74], or from any general fracture mechanics resources [20, 97, 21]. Many cohesive zone models have the form of a simple linear expression where the opening traction σ is proportional to the opening displacement [20, 97, 21] and each can be modeled across the entire cohesive zone using an approximated cubic function [74], or alternatively an exponential function. A schematic of the most common models used [20, 74] is shown in Figure 10.1, where Figure 10.1a shows the Dugdale-Barrenblatt model of constant stress in the cohesive zone. Figure 10.1b is an example of the exponential representation of traction separation adapted for lateral opening. However, the linear cohesive zone model (Figure 10.1c) is worth solving first because it is the next progression from the constant friction case (Figure 10.1a), and is less complicated than the exponential or polynomial function (Figure 10.1b). The model presented in Figure 10.1c

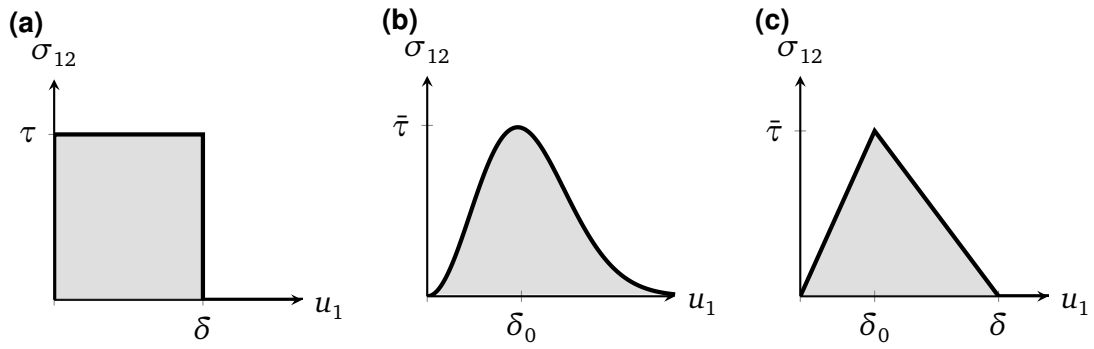

Figure 10.1: Visualization of various cohesive zone models reformulated for shear traction with lateral opening. (a) Dugdale-Barrenblatt model (b) Exponential cohesive zone model (c) Linear cohesive zone model.

in the range $u_1 < \delta_0$ represents a simple analogy where interfacial slippage is impeded by linear, horizontal springs on the bonded surface ($\theta = 0$). Then, the boundary condition is valid in the range $u_1 < \delta_0$, and has the form

$$\sigma_{12}(r,0) \equiv \hat{k} u_1(r,0), \tag{10.14}$$

where u_1 is the displacement in the x_1 direction and $\hat{k}$ is a positive constant which represents the slope of the curve, hence $\hat{k} \equiv \bar{\tau}/\delta_0$. Recall that:

$$u_1(r,\theta) \equiv x_1(r,\theta) - X_1(r,\theta) = x_1(r,\theta) - r\cos\theta. \tag{10.15}$$

This boundary condition has the form $\sigma_{12}(r,0) = \hat{k} u_1(r,0)$, or

$$\mu J^{-1}\left[\frac{\partial x_1}{\partial r}\frac{\partial x_2}{\partial r} + \frac{1}{r^2}\frac{\partial x_1}{\partial \theta}\frac{\partial x_2}{\partial \theta}\right]_{\theta=0} = \hat{k}\,[x_1(r,0) - r]. \tag{10.16}$$

Assuming the material remains attached, then $x_2(r,0) = 0$, hence

$$\left.\frac{\partial x_2}{\partial r}\right|_{\theta=0} = 0, \qquad \therefore \quad J(r,0) = \left.\frac{1}{r}\frac{\partial x_1}{\partial r}\frac{\partial x_2}{\partial \theta}\right|_{\theta=0}.$$

Re-arranging gives

$$\frac{1}{r^2}\frac{\partial x_1}{\partial \theta}\frac{\partial x_2}{\partial \theta} = k\frac{1}{r}\frac{\partial x_1}{\partial r}\frac{\partial x_2}{\partial \theta}(x_1 - r), \quad \text{on} \quad \theta = 0, \tag{10.17}$$

where $k \equiv \hat{k}/\mu$ and has a range of $0 < k < \infty$. Rearranging yields multiple cases, being

$$\left[\frac{\partial x_2}{\partial \theta}\right]_{\theta=0} = 0, \qquad \left[\frac{1}{r}\frac{\partial x_1}{\partial \theta} - k\frac{\partial x_1}{\partial r}(x_1 - r)\right]_{\theta=0} = 0, \qquad \text{or both.}$$

Using the second condition for x_1 (recall the logic from Section 3.2), then

$$\frac{1}{r}\frac{\partial x_1}{\partial \theta} - k\frac{\partial x_1}{\partial r}(x_1 - r) = 0, \quad \text{on} \quad \theta = 0, \tag{10.18}$$

The rest of the bonded conditions and equations for any compressible material are the same as the third column in Table 3.2.

This analysis has value because the linear and exponential cohesive zone models are utilized extensively in literature [22, 20, 21] and may also lead to a solution which bridges the no-slip and finite friction cases. In the above formulation, it is assumed that taking $k \to 0$ should collapse to finite friction condition and $k \to \infty$ should resemble the no-slip condition. Using other more complicated models may also provide other insights.

10.2.4 Solutions at Other Locations Along the Bonded Interface

Recall that Figures 8.12a and 8.12b showed different failure modes inside the bonded interface depending on positive or negative shear in the slip zone on the surface near $r \to 0$. However, the opposite end also shows a stress concentration which can be dealt with by solving a slightly different problem where the bulk material takes up a quarter of the plane, shown in Figure 10.2. The same method can again be used here to determine a second slip zone on the opposite end. Note that this problem is different than the interface crack problems because the (infinitely) long traction free end in the negative horizontal is now

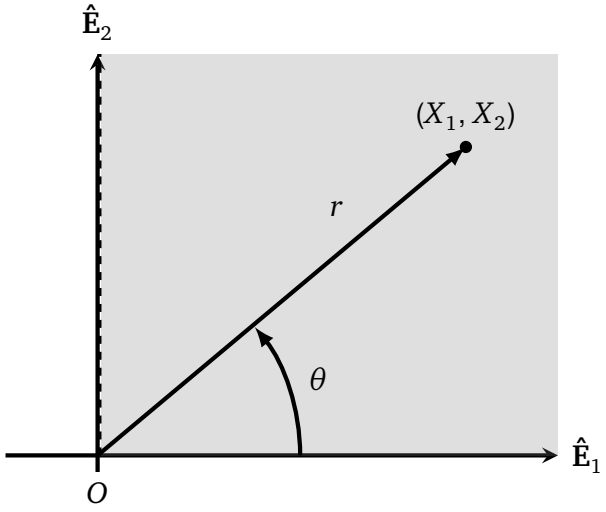

Figure 10.2: Visualization of the finite friction problem with origin at some location $r \to \tilde{L}$.

traded with a traction free end up the positive $\hat{\mathbf{E}}_2$ axis, and the coordinate extents are $r \geq 0$ and $0 \leq \theta \leq \pi/2$. The bonded boundary condition at $\theta = 0$ again requires $x_2(r, 0) = 0$ and Eqn. (3.30) (or, eqn (10.10) for incompressible materials). However, the traction free edge resides on the $\theta = \pi/2$ face (the vertical dashed line in Figure 10.2). Now, using $\mathfrak{N} = -\hat{\mathbf{E}}_1$, then $\mathcal{P}_{11}(r, \pi/2) = \mathcal{P}_{21}(r, \pi/2) = 0$, and using Eqns. (3.24) and (3.5) the new boundary condition on $\theta = \pi/2$ has the same form as Eqns. (3.29). The rest of the BVP for the quarter-plane problem requires Eqns. (3.27) and the bonded edge Eqns. (3.10) and (3.30) previously derived.

Also of interest, are the stress fields on each side of where the slip zone length ends (i.e. at $r \to \delta$). In this case, a re-formulation of the problem and coordinates must be done where the new polar coordinates have the constraints

$$X_1 \equiv r\cos\theta = \delta + R\cos\Theta, \tag{10.19a}$$

$$\text{and} \quad X_2 \equiv r\sin\theta = R\sin\Theta. \tag{10.19b}$$

Figure 10.3 shows the new geometry which looks similar to the original problem geometry

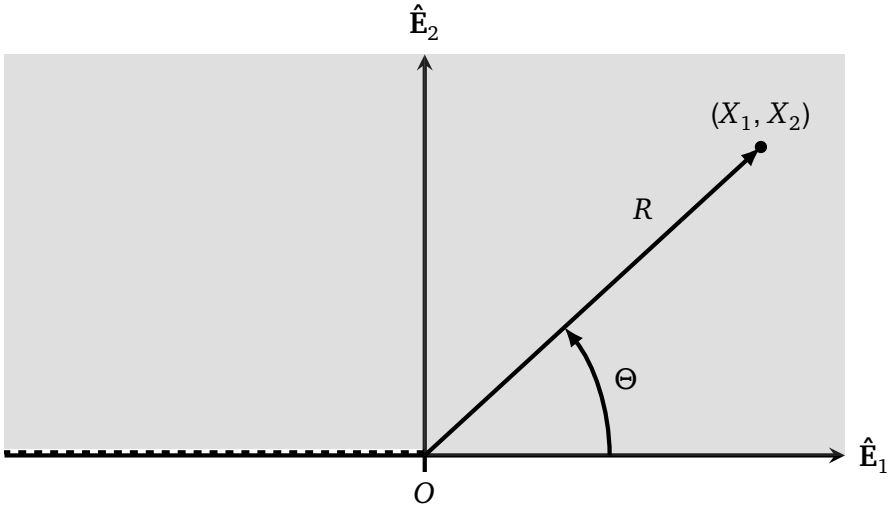

Figure 10.3: Visualization of the finite friction problem with origin at the slip zone.

from Figure 3.1, however the dashed line (on $\Theta = \pi$) remains attached ($\therefore x_2(R, \pi) = 0$) with a constant shear $\sigma_{12}(R, \pi) = \tau$. The bonded edge to the right would follow the conditions for no-slip where $u_1 = u_2 = 0$, such that $x_2(R, 0) = 0$ and $x_1(R, 0) = R + \delta$. These boundary conditions together with the governing body Eqns. (3.27) (which must be re-furnished using the coordinates R and Θ, details omitted here) make up the problem for finite friction near $r \rightarrow \delta$. While still not a global result, an asymptotic solution at more points on the bonded surface should provide insight on the entire surface so that global solution can be approximated. Then, problems like the tree frog detachment or other bonded joints can be directly compared using the analytical findings.

10.2.5 Other FEA Studies

Legrain et. al [106] outlined a finite element analysis method using the near field result close to the crack as 'enrichment functions' in order to aid convergence of the numerical simulations. The numerical simulations in this manuscript represented a monumental effort and convergence required a great deal of manual attention. It would be of interest to see if the near-field solutions for the no-slip and finite friction cases can be used in this way. If this

idea has merit, more extensive numerical analysis can be done in a much shorter time. For example, an FEA study which is of interest but time did not allow was to determine the full effects of β and ξ on a well discretized range of mixed loading conditions Δ_X and Δ_Y. Longer samples and geometry (the ratio was $10L \times 2L$ for simulations in this manuscript) would be of interest because in some simulations it was found that the opposing end interacted with the effects along the bonded surface and even near the crack tip.

Part V

References

Bibliography

[1] Lengyel TH, Long R, Schiavone P. Effect of interfacial slippage on the near-tip fields of an interface crack between a soft elastomer and a rigid substrate. Proceedings of the Royal Society of London A: Mathematical, Physical and Engineering Sciences. 2014;470(2170).

[2] Lengyel TH, Schiavone P, Long R. Interface Crack Between a Compressible Elastomer and a Rigid Substrate with Finite Slippage. Journal of the Mechanics and Physics of Solids (SUBMITTED). 2015;.

[3] Bhuyan S, Tanguy F, Martina D, Lindner A, Ciccotti M, Creton C. Crack propagation at the interface between soft adhesives and model surfaces studied with a sticky wedge test. Soft Matter. 2013;9(28):6515–6524.

[4] Grand View Research. Adhesives and Sealants Market Analysis And Segment Forecasts To 2020; 2015. [Online; accessed 01-May-2015]. Available from: http://www.grandviewresearch.com/industry-analysis/adhesives-and-sealants-market.

[5] Koncept Analytics. Global Adhesives & Sealants Market Report: 2014 Edition; 2014. [Online; accessed 01-May-2015]. Available from: http://www.researchandmarkets.com/research/v8hhpz/global_adhesives.

[6] Baldan A. Adhesion phenomena in bonded joints. International Journal of Adhesion and Adhesives. 2012;38(0):95 – 116.

[7] Zhang Newby BmZ, Chaudhury MK, Brown HR. Macroscopic Evidence of the Effect of Interfacial Slippage on Adhesion. Science. 1995 Sep;269(5229):1407–1409.

[8] Zhang Newby BmZ, Chaudhury MK. Effect of interfacial slippage on viscoelastic adhesion. Langmuir. 1997;13(6):1805–1809.

[9] Zhang Newby BmZ, Chaudhury MK. Friction in adhesion. Langmuir. 1998;14:4865–4872.

[10] Amouroux N, Petit J, Léger L. Role of interfacial resistance to shear stress on adhesive peel strength. Langmuir. 2001;17(21):6510–6517.

[11] Lu Z, Yu S, Wang X, Feng X. Effect of interfacial slippage in peel test: theoretical model. The European Physical Journal E. 2007;23(1):67–76.

[12] Collino RR, Philips NR, Rossol MN, McMeeking RM, Begley MR. Detachment of compliant films adhered to stiff substrates via van der Waals interactions: role of frictional sliding during peeling. Journal of The Royal Society Interface. 2014;11(97):20140453.

[13] Lefranc M, Bouchaud E. Mode I fracture of a biopolymer gel: rate-dependent dissipation and large deformations disentangled. Extreme Mechanics Letters. 2014;.

[14] Livne A, Bouchbinder E, Svetlizky I, Fineberg J. The near-tip fields of fast cracks. Science. 2010;327(5971):1359–1363.

[15] Hui CY, Jagota A, Bennison S, Londono J. Crack blunting and the strength of soft elastic solids. Proceedings of the Royal Society of London Series A: Mathematical, Physical and Engineering Sciences. 2003;459(2034):1489–1516.

[16] Wu KC, Huang SM. Dugdale model for an expanding crack under shear stress. Engineering Fracture Mechanics. 2013;104(0):198 – 207.

[17] Comninou M. The interface crack. Journal of Applied Mechanics. 1977;44(4):631–636.

[18] Comninou M. An overview of interface cracks. Engineering Fracture Mechanics. 1990;37(1):197 – 208.

[19] Williams M. The stresses around a fault or crack in dissimilar media. Bulletin of the seismological society of America. 1959;49(2):199–204.

[20] Anderson TL. Fracture Mechanics: Fundamentals and Applications. CRC press; 2005.

[21] Hutchinson JW. Nonlinear fracture mechanics. Department of Solid Mechanics, DtH. 1979;.

[22] Rice J. Elastic fracture mechanics concepts for interfacial cracks. Journal of applied mechanics. 1988;55(1):98–103.

[23] Zehnder AT. Lecture notes on fracture mechanics. Cornell University. 2007;.

[24] Tarantino AM. Thin hyperelastic sheets of compressible material: field equations, Airy stress function and an application in fracture mechanics. Journal of elasticity. 1996;44(1):37–59.

[25] Elices M, Guinea GV, Gomez J, Planas J. The cohesive zone model: advantages, limitations and challenges. Engineering Fracture Mechanics. 2002;69(2):137 – 163.

[26] Shi X, Zhao YP. Comparison of various adhesion contact theories and the influence of dimensionless load parameter. Journal of Adhesion Science and Technology. 2004;18(1):55–68.

[27] Herrmann JM. An asymptotic analysis of finite deformations near the tip of an interface-crack. Journal of Elasticity. 1989;21(3):227.

[28] Herrmann JM. An asymptotic analysis of finite deformations near the tip of an interface-crack: Part II. Journal of Elasticity. 1992;29(3):203.

[29] da Silva LFM, das Neves PJC, Adams RD, Spelt JK. Analytical models of adhesively bonded joints-Part I: Literature survey. International Journal of Adhesion and Adhesives. 2009;29(3):319 – 330.

[30] da Silva LFM, das Neves PJC, Adams RD, Wang A, Spelt JK. Analytical models of adhesively bonded joints-Part II: Comparative study. International Journal of Adhesion and Adhesives. 2009;29(3):331 – 341.

[31] Kinloch AJ. The science of adhesion. Journal of Materials Science. 1980;15(9):2141–2166.

[32] Kinloch AJ. The science of adhesion. Journal of Materials Science. 1982;17(3):617–651.

[33] Kendall K. Crack propagation in lap shear joints. Journal of Physics D: Applied Physics. 1975;8(5):512.

[34] Holzapfel GA. Nonlinear Solid Mechanics: A Continuum Approach for Engineering. John Wiley & Sons; 2000.

[35] Gravish N, Wilkinson M, Autumn K. Frictional and elastic energy in gecko adhesive detachment. Journal of The Royal Society Interface. 2008;5(20):339–348.

[36] Endlein T, Ji A, Samuel D, Yao N, Wang Z, Barnes WJP, et al. Sticking like sticky tape: tree frogs use friction forces to enhance attachment on overhanging surfaces. Journal of The Royal Society Interface. 2013;10(80).

[37] Kendall K. Thin-film peeling-the elastic term. Journal of Physics D: Applied Physics. 1975;8(13):1449. Available from: http://stacks.iop.org/0022-3727/8/i=13/a=005.

[38] Yoshizawa H, You-Lung C, Israelachvili J. Recent advances in molecular level understanding of adhesion, friction and lubrication. Wear. 1993;168(1 - 2):161 – 166.

[39] Chadwick P. Continuum Mechanics: Concise Theory and Problems. Dover books on physics. DOVER PUBN Incorporated; 1999.

[40] Gurtin ME. An Introduction to Continuum Mechanics. Mathematics in Science and Engineering. Elsevier Science; 1982.

[41] Gurtin ME, Fried E, Anand L. The Mechanics and Thermodynamics of Continua. The Mechanics and Thermodynamics of Continua. Cambridge University Press; 2010.

[42] Ali A, Hosseini M, Sahari B. A review and comparison on some rubber elasticity models. Journal of Scientific and Industrial Research. 2010;69(7):495–500.

[43] Ali A, Hosseini M, Sahari B. A review of constitutive models for rubber-like materials. American Journal of Engineering and Applied Sciences. 2010;3(1):232.

[44] Horgan CO, Saccomandi G. Constitutive Models for Compressible Nonlinearly Elastic Materials with Limiting Chain Extensibility. Journal of Elasticity. 2004;77(2):123–138.

[45] Arruda EM, Boyce MC. A three-dimensional constitutive model for the large stretch behavior of rubber elastic materials. Journal of the Mechanics and Physics of Solids. 1993;41(2):389–412.

[46] Boyce MC, Arruda EM. Constitutive Models of Rubber Elasticity: A Review. Rubber Chemistry and Technology. 2000;73(3):504–523.

[47] Blatz PJ, Ko WL. Application of Finite Elastic Theory to the Deformation of Rubbery Materials. Transactions of The Society of Rheology (1957-1977). 1962;6(1):223–252.

[48] Knowles JK, Sternberg E. An asymptotic finite-deformation analysis of the elastostatic field near the tip of a crack. Journal of Elasticity. 1973;3(2):67–107.

[49] Rajagopal K, Tao L. On an inhomogeneous deformation of a generalized neo-Hookean material. Journal of elasticity. 1992;28(2):165–184.

[50] Geubelle PH, Knauss WG. Finite strains at the tip of a crack in a sheet of hyperelastic material: I. Homogeneous case. Journal of Elasticity. 1994;35(1-3):61–98.

[51] Geubelle PH, Knauss WG. Finite strains at the tip of a crack in a sheet of hyperelastic material: II. Special bimaterial cases. Journal of Elasticity. 1994;35(1-3):99–137.

[52] Geubelle PH, Knauss WG. Finite strains at the tip of a crack in a sheet of hyperelastic material: III. General bimaterial case. Journal of Elasticity. 1994;35(1-3):139–174.

[53] Brostow W. Mechanical properties. In: Physical properties of polymers handbook. Springer; 2007. p. 423–445.

[54] Pocius AV. Adhesives. In: Physical Properties of Polymers Handbook. Springer; 2007. p. 479–486.

[55] Gibert FX, Allal A, Marin G, Derail C. Effect of the rheological properties of industrial hot-melt and pressure-sensitive adhesives on the peel behavior. Journal of Adhesion Science and Technology. 1999;13(9):1029–1044.

[56] Tsai K, Kim K. Stick-slip in the thin film peel test-I. the 90° peel test. International Journal of Solids and Structures. 1993;30(13):1789 – 1806.

[57] Schallamach A. How does rubber slide? Wear. 1971;17(4):301 – 312.

[58] Gent A. Adhesion and strength of viscoelastic solids. Is there a relationship between adhesion and bulk properties? Langmuir. 1996;12(19):4492–4496.

[59] Nase J, Creton C, Ramos O, Sonnenberg L, Yamaguchi T, Lindner A. Measurement of the receding contact angle at the interface between a viscoelastic material and a rigid surface. Soft Matter. 2010;6:2685–2691.

[60] Nase J, Ramos O, Creton C, Lindner A. Debonding energy of PDMS. The European Physical Journal E. 2013;36(9):1–10.

[61] Ghatak A, Vorvolakos K, She H, Malotky DL, Chaudhury MK. Interfacial rate processes in adhesion and friction. The Journal of Physical Chemistry B. 2000;104(17):4018–4030.

[62] Allegra G, Raos G. Sliding friction between polymer surfaces: a molecular interpretation. The Journal of chemical physics. 2006 April;124(14):144713. Available from: http://dx.doi.org/10.1063/1.2193509.

[63] Gent A, Kinloch A. Adhesion of viscoelastic materials to rigid substrates. III. Energy criterion for failure. Journal of Polymer Science Part A-2: Polymer Physics. 1971;9(4):659–668.

[64] Momozono S, Nakamura K, Kyogoku K. Theoretical model for adhesive friction between elastomers and rough solid surfaces. The Journal of Chemical Physics. 2010;132(11):–. Available from: http://scitation.aip.org/content/aip/journal/jcp/132/11/10.1063/1.3356220.

[65] Tanguy F, Nicoli M, Lindner A, Creton C. Quantitative analysis of the debonding structure of soft adhesives. The European Physical Journal E. 2014;37(1). Available from: http://dx.doi.org/10.1140/epje/i2014-14003-8.

[66] Liechti KM, Wu JD. Mixed-mode, time-dependent rubber/metal debonding. Journal of the Mechanics and Physics of Solids. 2001;49(5):1039–1072.

[67] Ondaruhu T. Tack of a polymer melt: adhesion measurements and fracture profile observations. Journal de Physique II. 1997;7(12):1893–1916.

[68] Sun S, Li M, Liu A. A review on mechanical properties of pressure sensitive adhesives. International Journal of Adhesion and Adhesives. 2013;41(0):98 – 106.

[69] Chiche A, Pareige P, Creton C. Role of surface roughness in controlling the adhesion of a soft adhesive on a hard surface. Comptes Rendus de l'Académie des Sciences-Series IV-Physics. 2000;1(9):1197–1204.

[70] Fuller K, Tabor D. The effect of surface roughness on the adhesion of elastic solids. Proceedings of the Royal Society of London A Mathematical and Physical Sciences. 1975;345(1642):327–342.

[71] Persson B, Tosatti E. The effect of surface roughness on the adhesion of elastic solids. The Journal of Chemical Physics. 2001;115:5597.

[72] Begley MR, Collino RR, Israelachvili JN, McMeeking RM. Peeling of a tape with large deformations and frictional sliding. Journal of the Mechanics and Physics of Solids. 2013;61(5):1265 – 1279.

[73] Bender CM, Orszag SA. Advanced mathematical methods for scientists and engineers I: Asymptotic methods and perturbation theory. vol. 1. Springer; 1999.

[74] Park K, Paulino GH. Cohesive zone models: a critical review of traction-separation relationships across fracture surfaces. Applied Mechanics Reviews. 2011;64(6):060802.

[75] Erdogan F. Stress distribution in bonded dissimilar materials with cracks. Journal of Applied Mechanics. 1965;32(2):403–410.

[76] England A. A crack between dissimilar media. Journal of Applied Mechanics. 1965;32(2):400–402.

[77] Knowles JK, Sternberg E. Finite-deformation analysis of the elastostatic field near the tip of a crack: Reconsideration and higher-order results. Journal of Elasticity. 1974;4(3):201–233.

[78] Knowles JK, Sternberg E. On the singularity induced by certain mixed boundary conditions in linearized and nonlinear elastostatics. International Journal of Solids and Structures. 1975;11(11):1173 – 1201.

[79] Knowles J, Sternberg E. Large deformations near a tip of an interface-crack between two Neo-Hookean sheets. Journal of Elasticity. 1983;13(3):257–293.

[80] Stephenson RA. The equilibrium field near the tip of a crack for finite plane strain of incompressible elastic materials. Journal of Elasticity. 1982;12(1):65.

[81] Long R, Krishnan VR, Hui CY. Finite strain analysis of crack tip fields in incompressible hyperelastic solids loaded in plane stress. Journal of the Mechanics and Physics of Solids. 2011;59(3):672–695.

[82] Krishnan VR, Hui CY. Large deformation of soft elastic materials in adhesive contact with a rigid cylindrical flat punch. Soft Matter. 2008;4(9):1909–1915.

[83] Knowles JK. The finite anti-plane shear field near the tip of a crack for a class of incompressible elastic solids. International Journal of Fracture. 1977;13(5):611–639.

[84] Krishnan VR, Hui CY, Long R. Finite Strain Crack Tip Fields in Soft Incompressible Elastic Solids. Langmuir. 2008;24(24):14245–14253.

[85] Knowles JK, Sternberg E. On a class of conservation laws in linearized and finite elastostatics. Archive for Rational Mechanics and Analysis. 1972;44(3):187–211.

[86] Reddy J. An Introduction to the Finite Element Method. Engineering Series. McGraw-Hill Education; 2005.

[87] Adeeb S. Introduction to Solid Mechanics and Finite Element Analysis Using Mathematica. Kendall Hunt Publishing Company; 2013.

[88] Hughes TJR. The Finite Element Method: Linear Static and Dynamic Finite Element Analysis. Dover Civil and Mechanical Engineering. Dover Publications; 2012.

[89] Oden JT. Finite Elements of Nonlinear Continua. Dover Civil and Mechanical Engineering. Dover Publications; 2013.

[90] Stewart J. Calculus. Cengage Learning; 2011.

[91] Dugdale D. Yielding of steel sheets containing slits. Journal of the Mechanics and Physics of Solids. 1960;8(2):100–104.

[92] Harrop LP. Application of a modified Dugdale model to the K vs {COD} relation. Engineering Fracture Mechanics. 1978;10(4):807 – 816.

[93] Barenblatt GI. The mathematical theory of equilibrium cracks in brittle fracture. Advances in applied mechanics. 1962;7(1):55–129.

[94] Sancaktar E. Constitutive Adhesive and Sealant Models. In: da Silva LM, Öchsner A, Adams R, editors. Handbook of Adhesion Technology. Springer Berlin Heidelberg; 2011. p. 551–595.

[95] Ogden RW. Non-Linear Elastic Deformations. Dover Civil and Mechanical Engineering. Dover Publications; 2013.

[96] Blatz P. On the Thermostatic Behavior of Elastomers. In: Chompff AJ, Newman S, editors. Polymer Networks. Springer US; 1971. p. 23–45.

[97] Rice J, Sih GC. Plane problems of cracks in dissimilar media. Journal of Applied Mechanics. 1965;32(2):418–423.

[98] Hutchinson JW, Suo Z. Mixed mode cracking in layered materials. Advances in applied mechanics. 1992;29(63):191.

[99] Rice JR. A path independent integral and the approximate analysis of strain concentration by notches and cracks. Journal of applied mechanics. 1968;35(2):379–386.

[100] Version A. 6.13. Analysis User's Guide, Dassault Systems. 2013;.

[101] Montgomery DC, Runger GC. Applied statistics and probability for engineers. John Wiley & Sons; 2010.

[102] Mark JE. Physical properties of polymers handbook. Springer; 1996.

[103] Thomson W. Theory of vibration with applications. CRC Press; 1996.

[104] Kulakowski BT, Gardner JF, Shearer JL. Dynamic modeling and control of engineering systems. Cambridge University Press; 2007.

[105] Crandall SH. Engineering analysis: A survey of numerical procedures. Krieger Publishing Co., Inc.; 1983.

[106] Legrain G, Moës N, Verron E. Stress analysis around crack tips in finite strain problems using the eXtended finite element method. International Journal for Numerical Methods in Engineering. 2005;63(2):290–314.